Université catholique de Louvain
École polytechnique de Louvain
Institut de mécanique, matériaux et génie civil (iMMC)
Avenue G. Lemaître 4, 1348 Louvain-la-Neuve, Belgique

Cenaero
Rue des Frères Wright 29, 6041 Gosselies, Belgique
Email : ariane.frere@cenaero.be
http://www.cenaero.be

Wind turbine and aircraft industries rely on global numerical optimization to reach high performances in ever shorter times to market. Computational Fluid Dynamics (CFD) boost the industrial competitiveness and this can be pushed further by developing more reliable methods. The two main methods are Large-Eddy Simulation (LES) and Reynolds-Averaged Navier-Stokes (RANS). LES resolves accurately a significant part of the unsteady flow, while RANS provides the averaged flow; it is thus dramatically cheaper than LES, and has been the established method in design for decades. Recent needs from the industry motivate the switch to the higher fidelity LES method. However, the computational requirements of wall-resolved LES (wrLES) remain unaffordable for flows at high Reynolds numbers, as in most of the relevant applications.

This work is dedicated to the implementation and validation of wall-modeled LES (wmLES) to drastically reduce the cost. WmLES alleviates the near-wall grid requirement by employing a model to reconstruct the wall shear stress. The developments are made in a Discontinuous Galerkin (DG) framework, chosen for its high accuracy and scalability. The DG wrLES approach is first validated on low Reynolds number airfoils. The DG wmLES approach is then developed and validated on a turbulent channel flow, also providing rules of good practice. It is then applied to the flow over a NACA 4412 airfoil at a high Reynolds number, where it is seen to successfully capture the global flow behavior; thereby inspiring confidence in its potential. Finally, a wrLES computation of the same airfoil allows to evaluate several wall models, and to identify paths for future wmLES developments.

Ariane Frère received her degree in electromechanical engineering from the Université Libre de Bruxelles in 2008. She joined Cenaero after working on wind turbine design at GE Wind. She then pursued her PhD between 2013 and 2017 at Cenaero and UCL, in collaboration with DTUWind.

656 | 2018

Ariane Frère

Towards wall-modeled LES of high Reynolds number airfoils using a DG method

UCL
Université catholique de Louvain

Towards wall-modeled Large-Eddy Simulations of high Reynolds number airfoils using a discontinuous Galerkin method

Ariane Frère

Juin 2018

Thèse présentée en vue de l'obtention du grade de docteur en sciences de l'ingénieur

École polytechnique de Louvain

Université catholique de Louvain

UCL Université catholique de Louvain

UNIVERSITÉ CATHOLIQUE DE LOUVAIN
ÉCOLE POLYTECHNIQUE DE LOUVAIN
INSTITUT DE MÉCANIQUE, MATÉRIAUX ET GÉNIE CIVIL

TOWARDS WALL-MODELED LARGE-EDDY SIMULATIONS OF HIGH REYNOLDS NUMBER AIRFOILS USING A DISCONTINUOUS GALERKIN METHOD

DOCTORAL DISSERTATION PRESENTED BY

ARIANE FRÈRE

IN PARTIAL FULFILLMENT OF THE REQUIREMENTS
FOR THE DEGREE OF DOCTOR IN ENGINEERING SCIENCES

THESIS COMMITTEE:

Prof. Philippe Chatelain, Université catholique de Louvain (Advisor)
Prof. Grégoire Winckelmans, Université catholique de Louvain (Advisor)
Prof. Jean-François Remacle, Université catholique de Louvain
Dr. Koen Hillewaert, Cenaero
Prof. Philipp Schlatter, KTH Royal Institute of Technology
Prof. Martin O. L. Hansen, DTU Wind Technical University of Denmark
Prof. Thomas Pardoen, Université catholique de Louvain (President)

Louvain-la-Neuve, June 2018

MERCI

First of all, I would like to thank you, dear reader. The research is not meaningful to me if it is not shared and discussed. So, thank you for opening this book and for your interest in my work. I take this opportunity to also thank all the readers, reviewers, listeners, editors and conference organizers who allowed me to share my findings and to receive feedback. Your advise contributed to push my reflexion further and to produce the work presented here.

I would like to thank especially the members of my jury, Prof. P. Schlatter from KTH, Prof. M. O. L. Hansen from DTU Wind, Prof. J.-F. Remacle and Prof. T. Pardoen from UCL. Thank you for the time you spent to read, verify and comment my work. I have modified my text to reflect the precious discussions we had during my private defense. I hope that this improved version will meet all your expectations.

I definitely would like thank the different financial supports that I have received during this PhD. This research has been financed by the Walloon Region through the FirstDoCA framework, as well as by Cenaero research center. I also received an IRP Wind Mobility grant to work during three months at DTUWind. I would like to thank EERA Wind for this grant, as well as Dr. Torben Larsen, Prof. Niels Sørensen, Dr. Hamid Sarlak and Dr. Robert Mikkelsen for their continuous support and collaboration. The study benefited from computational resources made available on the Tier-1 supercomputer of the Fédération Wallonie-Bruxelles (n° 1117545), as well as on the Tier-0 Jülich Supercomputing Center (PRACE project R2Wall).

Je voudrais évidemment remercier plus particulièrement mes promoteurs : Dr. Koen Hillewaert, Prof. Philippe Chatelain et Prof. Grégoire Winckelmans. Merci Koen d'avoir été tout de suite motivé par mon envie d'utiliser Argo pour des applications en Éolien. Merci pour ta curiosité sans limite. Merci de m'avoir accueillie dans ton équipe et d'avoir voulu relever le défi de faire de moi une Argonaute. Merci Philippe pour ton dynamisme sans faille et ta positive attitude. Merci pour tes conseils avisés et tes fameuses phrases choc qui ont boosté mes introductions et conclusions. Merci, surtout, de m'avoir convaincue que j'y arriverais. Last but no least, Merci Grégoire pour tes commentaires de fond et tes remises en question. Merci de ton intérêt pour ma recherche. Merci de m'avoir aidée à clôturer ce travail. Merci à vous trois de

m'avoir guidée pour chercher et trouver des solutions. Merci d'avoir toujours trouvé du temps pour moi, alors que vous n'en aviez pas. Merci pour vos lectures, relectures et rerelectures. Je pense que là, c'est la bonne. Et j'espère que, sur ce point, vous serez tous d'accord .

Je voudrais aussi remercier mes collègues, dont nombreux sont devenus des amis. Tout d'abord, Merci Jean-Sébastien. Merci pour tes remarques pertinentes, tes explications claires et ta patience. Merci Corentin, Pierre et Michel pour votre précieuse aide, du debug de code à la visu des résultats. Côté UCL, Merci Maud, Sophia, Olivier T., Philippe P. et Yves pour vos regards extérieurs sur mon travail et, surtout, pour votre amitié. Merci Sophia et Maud d'avoir partagé avec moi ces nombreux weekends de rédaction. Merci à mes teamleaders Cécile et Eric, d'avoir soutenu mon désir de faire cette thèse et de m'avoir donné la liberté nécessaire pour y arriver. Merci à la fine équipe du covoiturage (Sophia, Corentin, JS, Arnaud, Ludwig, Pierre et Rebecca) pour toutes ces heures de debriefing et de rigolade. Merci aussi Séverine et Merci Isabelle d'avoir géré tout le côté administratif de mon travail. Merci à tous mes collègues de Cenaero, de l'UCL et de DTUWind qui ont fait de mon temps de travail un temps riche en échanges et en bonne humeur.

Ce travail n'aurait pas été possible si je n'avais pas, en plus de tous ces supers collègues, une équipe de choc côté privé. Je remercie donc grandement ma famille (l'originelle et la belle) et mes amis. Merci pour votre soutien, vos petits-plats et vos si nombreux baby-sittings. Je remercie particulièrement mes amies menthes poivrées qui, par leurs rires, coaching et soirées, m'ont permis de me changer les idées et de repartir du bon pied. Merci Elise, par ta présence et tes pauses forcées à la plaine de jeux, tu m'as donné le recul et la maturité nécessaires pour mener à bien ce travail. Enfin et surtout, Merci Thomas! Merci Liebe de m'avoir encouragée et soutenue durant tout ce périple. Merci d'avoir su, avant moi, que je voulais faire cette thèse. Et Merci de m'avoir permis d'y arriver. Ce doctorat, je vous le dois!

The answer, my friend, is blowin' in the wind.
Bob Dylan

CONTENTS

Contents **i**

1 Introduction **1**
1.1 Wall-modeled LES 7
1.2 Objectives and structure of the thesis 10

2 Wall models and discontinuous Galerkin method **13**
2.1 Modeling the boundary layer 13
2.1.1 Boundary layer characterization 14
2.1.2 Universal velocity profile 17
2.1.3 Quasi analytical wall models 22
2.1.4 Velocity profile for boundary layers subjected to a pressure gradient 24
2.1.5 Wall models for boundary layers subjected to a pressure gradient 28
2.2 Numerical approach 31
2.2.1 Navier-Stokes equations 31
2.2.2 Spatial discretization: discontinuous Galerkin method . 32
2.2.3 Implicit Large-Eddy Simulation 34
2.2.4 Time discretization 35
2.3 wmLES strategy 37
2.3.1 Wall boundary conditions 37
2.3.2 Implemented wall models 38
2.3.3 Specific design criteria 41

3 Low Reynolds number airfoils **43**
3.1 Low Reynolds number flow phenomena 43
3.2 S826 airfoil: wrLES-experimental cross-validation 48
3.2.1 Numerical setup 48
3.2.2 wrLES at $Re = 4 \times 10^4$ for $AOA = 0°$ and $12°$ 50
3.2.3 wrLES at $Re = 1 \times 10^5$ for $AOA = 0°$ and $12°$ 55
3.2.4 Sensitivity analysis with respect to the span extent 59
3.2.5 Oil flow visualization 62
3.3 E387 airfoil: comparison to state-of-the-art tools 66
3.3.1 Numerical setup 66
3.3.2 wrLES at $Re = 6 \times 10^4$ for $AOA = 4°$ and $8°$ 67

3.3.3 Capture of the hysteresis at $Re = 6 \times 10^4$ and $AOA = 6°$ 73
3.4 Achievements 76

4 Turbulent channel flow **79**
4.1 Motivation 79
4.2 Sensitivity analysis at $\mathbf{Re}_\tau = \mathbf{5200}$ 82
4.2.1 Computational setup 82
4.2.2 Baseline cases using polynomials of degree 3 and 4 . . . 84
4.2.3 Impact of the input location 88
4.2.4 Impact of the interpolation order 90
4.2.5 Grid refinement and aspect ratio study 94
4.2.6 Space and time averaging 96
4.3 Additional evaluation: unstructured meshes and $\mathbf{Re}_\tau = \mathbf{50000}$ 99
4.4 Conclusions and best practice guidelines 102

5 High Reynolds number airfoils **105**
5.1 Motivation 105
5.2 NACA4412 airfoil: wall-modeled LES 106
5.2.1 Numerical setup 106
5.2.2 Comparison to state-of-the-art tools 108
5.2.3 Challenges for wmLES development 113
5.3 NACA4412 airfoil: wall-resolved LES 114
5.3.1 Numerical setup 114
5.3.2 Comparison to previous studies 119
5.3.3 Characterization of the boundary layer subject to an APG 126
5.3.4 Comparison with different wall model estimates 131
5.4 Comparison between wmLES and wrLES 137
5.5 Preliminary results: wrLES with a span ten times larger 140
5.5.1 Numerical setup 140
5.5.2 Initialization: use of the wrLES with a small span 142
5.6 Achievements 147

6 Conclusions and perspectives **149**
6.1 Conclusions 150
6.2 Perspectives 153

Bibliography **157**

A Turbulent channel flow: additional test cases **167**
A.1 Grid refinement and aspect ratio study for variable order cases . 167
A.2 Mean velocity fluctuations 169

B Two-Layer Model: impact of the ν_t **171**

C Robustness problems on IGV **173**

CHAPTER 1

INTRODUCTION

As for the first flying vehicles, the first wind turbines were designed through full scale prototype tests, sometimes successful, sometimes not. This trial and error approach permitted an incremental development of the technologies. Nowadays, these machines are gigantic. The V164 wind turbine, for example, has a rotor diameter of 164 meters. Its blades weigh 35 tons each and its nacelle weighs 400 tons. The nacelle is mounted at the top of a 140 meter high tower. Obviously, given these dimensions, the costs related to the breaking of a turbine are so high that a full scale "trial and error" development is no longer feasible. Furthermore, the currently targeted performance and time-to-market are such that the incremental design evolution is no longer fast enough. The innovation relies on global optimization where a large number of different configurations need to be evaluated. This explains the quest for ever more fast and reliable simulation frameworks. The "ideal design tool" should be

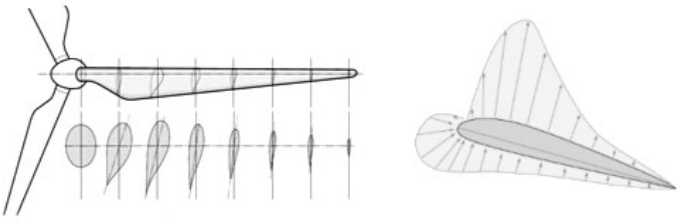


Figure 1.1: Schematic of a typical wind turbine blade division into several 2D airfoil sections. Images taken from [28, 63].

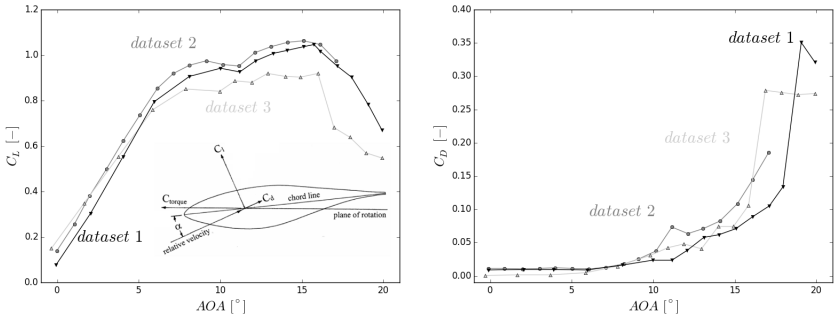


Figure 1.2: Lift (left) and drag (right) force coefficients measured on the S809 airfoil for different angles of attack in three different wind tunnels. The forces are represented on a schematic with the angle of attack α, the lift C_l and the drag C_d coefficients. The results are reproduced based on data and schematic from [94].

capable of reproducing faithfully the flow around the blade, the deformation induced on every single element of the structure and the heat generated in the electrical system. However, if such simulations could be performed, they would probably be as long and expensive as full scale testing. Therefore, the global problem is separated in smaller independent problems and simplifying assumptions are required.

A central working hypothesis in the wind sector aerodynamics is the division of the 3D-blade into several sections, as presented on Figure 1.1. Each section can then be considered as 2D and evaluated as such. This approach is called blade element method and due to its simplicity and large applicability, it remains the main design tool in the wind industry [88]. Note that this method is also common for the preliminary design cycles of aircraft wings and helicopter blades. The performance of a blade section is then characterized by the lift and drag force coefficients obtained for a range of angles of attack. These 2D performance curves are often referred to as "airfoil polars". For example, Figure 1.2 presents the lift and drag force coefficients measured for different angles of attack in three different wind tunnels for a typical wind turbine airfoil.

Wind turbine aeroelastic and wake models rely on this aerodynamic simplification to predict loads and energy production. Wind load and farm production predictions depend hence largely on the quality of the airfoil polar. For example, the study called "The Nebulous Art of Using Wind Tunnel Airfoil Data for Predicting Rotor Performance" [94] showed that the predicted power of a test wind turbine was dramatically dependent on the airfoil dataset. By using one or another dataset from Figure 1.2, very different power predictions are obtained, as presented on Figure 1.3.

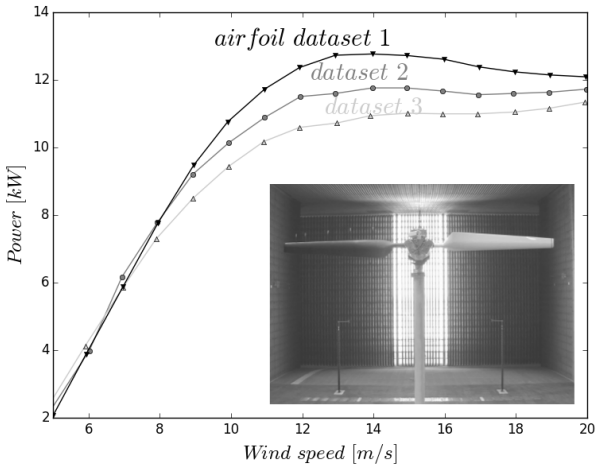


Figure 1.3: Predictions of the power produced by the NREL 10m diameter test turbine described in [38] in function of the wind speed. The predictions are made using three different airfoil datasets. The results are reproduced based on data from [94], the picture comes from [38].

Accurate airfoil polar data are difficult to obtain. In experiments, the measured characteristics can vary due to slight differences in the wind tunnel turbulence level or the geometry of walls and test section. These differences are extremely difficult to avoid. Moreover, for high incidence flows, blockage effects and interactions with the tunnel walls are often observed. Therefore, the use of a "virtual wind tunnel" where the geometry and the flow conditions are well controlled is a very attractive perspective. Such "virtual wind tunnel" is in theory possible using numerical simulation and, in particular, Computational Fluid Dynamics (CFD) that solves numerically the fluid governing equations. Therefore, CFD is largely used in the industry and, in the aircraft and the wind industries, it is part of the daily design process. The CFD methods have permitted already to boost the industry competitivity. This can be pushed further by the development of faster and more reliable CFD approaches.

The main challenge in CFD consists in the representation of the turbulence. A flow is considered turbulent when its motion is highly three-dimensional, chaotic and characterized by vortical structures (vortices) present at various scales of the flow. The turbulent regime is defined as opposite to the laminar regime, where the flow is smooth and where there is no mixing between neighboring fluid layers. The two flow regimes can be observed in the smoke of a candle, as presented in Figure 1.4. Close to the flame, the flow is laminar. It then becomes turbulent and comprises large and small eddies. The transition from a laminar to a turbulent flow is characterized by a dimensionless number called the Reynolds number. The Reynolds number is defined as the

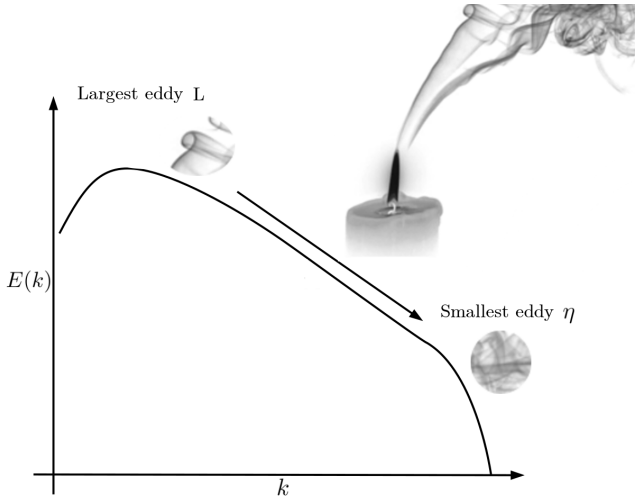


Figure 1.4: Typical energy spectrum of homogeneous isotropic turbulence with the eddy energy E in function of the eddy wave number k. The image is composed based on the energy spectrum taken from [15] and a picture of candle taken from [73].

ratio between the inertial and the viscous forces and is given by

$$Re = \frac{U\,L}{\nu}, \tag{1.1}$$

where U is a characteristic velocity of the flow, L is a characteristic length and ν is the kinematic viscosity of the fluid. For moderate Reynolds numbers, the regime is laminar. However, in most of the applications that are relevant to engineering, the flows are turbulent.

The complexity of turbulent flows can be traced to the fact that they involve flow structures of drastically different length scales. In 1920 already, Richardson found that the largest vortices or eddies, which have the highest energy content, break down into smaller eddies of lower energy, until the eddies are so small that they are dissipated into heat by viscosity. This energy transfer from large to small eddies is called "energy cascade" and is illustrated in Figure 1.4. Note that the energy is represented as a function of the wave number k; so the eddies of large scale L have a small wave number and the eddies of small scale η have a high wave number.

From dimensional arguments, Kolmogorov found that the characteristic scale of the smallest eddies η in a homogeneous isotropic turbulent flow, depends only on the viscosity and the energy dissipation rate ϵ as

$$\eta = \left(\frac{\nu^3}{\epsilon}\right)^{\frac{1}{4}}. \tag{1.2}$$



Figure 1.5: Simulation of a turbulent jet flow with three different CFD approaches: DNS (left), LES (center) and RANS (right) [52].

As the dissipation rate is determined by the large scales of the flow according to

$$\epsilon \propto \frac{U^3}{L}, \tag{1.3}$$

we find that the ratio between the largest and the smallest eddies is directly linked to the Reynolds number as

$$\frac{L}{\eta} \propto \left(\frac{UL}{\nu}\right)^{3/4} = Re^{3/4}. \tag{1.4}$$

In order to perfectly resolve the flow, performing a so-called Direct Numerical Simulation (DNS), the discretization should capture the largest and the smallest eddies. Therefore, the grid cost would be proportional to L/η along one dimension. In 3D, furthermore considering that the time resolution depends on the size of the smallest element, we obtain that the total computational cost of a DNS is proportional the cube of the Reynolds number

$$\left(\frac{L}{\eta}\right)^4 \propto Re^3. \tag{1.5}$$

At the time of writing this work, the most advanced DNS performed on an airfoil considered a Reynolds number $Re = 4 \times 10^5$. This computation required a resource corresponding to several tens of thousands of cores during a hundred days [98], which is a computation power only exceptionally available on large computational facilities. Considering that this computation characterized the flow at a single angle of attack, and that the Reynolds numbers of interest for the industry are about ten times higher, DNS is obviously not affordable for daily industrial design tasks. Therefore, to make the problems of interest tractable, solutions are proposed to model the turbulence.

Several turbulence modeling approaches exist and the choice of one or another depends on the compromise between the targeted accuracy and the computational cost, on the flow conditions and on the information needed (average or unsteady fields). The two main approaches are Large-Eddy Simulation (LES) and Reynolds-Averaged Navier-Stokes (RANS). Figure 1.5 compares them to a DNS by showing the instantaneous flow field obtained for the simulation of

a turbulent jet flow. As it can be observed on this figure, the LES approach is the closest to the DNS as it resolves properly a significant fraction of the eddies of the flow and, as first proposed by Smagorinsky[87], it models the effect of the unresolved (*i.e.* subgrid) eddies on the resolved ones. By looking at the energy cascade in Figure 1.4, this method corresponds to the resolution of the most energetic eddies and of a significant part of those lying in the inertial range (*i.e.* in the cascade). Beyond a certain wave number, the eddies are filtered. Most of the LES approaches use then a "subgrid-scale" (SGS) model to represent the effect of the unresolved scales on the resolved scales.

In the absence of walls, this truncation filtering makes LES much more affordable than DNS as the size of the smallest eddies that are solved no longer depends on the Reynolds number. As illustrated on this figure, the RANS approach provides a global averaged flow behavior but does not resolve correctly the eddies. This large modeling simplification makes RANS dramatically cheaper than LES and therefore, RANS is established as the main design tool in the industry for decades. However, in spite of its affordability, RANS has limitations for some applications, as for example for highly separated or unsteady flows. The use of a LES approach is then necessary to provide complementary results and deeper physical insights.

The independence of the LES cost with respect to the Reynolds number is very promising. However, it is not valid for wall-bounded flows, for which other solutions need to be developed. In the presence of walls, a region of high shear appears between the wall, where the flow is at rest, and the top of boundary layer, where the flow has attained large velocity. This shear changes the shape of the turbulent structures and cannot be filtered anymore, as for LES of homogeneous isotropic turbulence. As the size of the near-wall smallest eddies decreases drastically with the Reynolds number, the cost of LES of wall-bounded flows - although orders of magnitude smaller - scales as fast as that of DNS. For this reason, Spalart *et al.* [90] use the name Quasi-DNS (QDNS) to describe LES where wall turbulence is resolved. As a consequence, new approaches have been developed over the last few years to reduce the cost of wall-resolved LES. These techniques are based on the addition of models to represent the wall turbulence and they are called wall-modeled LES (wmLES).

In this context, the present work aims at providing a more accurate, and, at the same time, still affordable, CFD approach to the wind and aircraft industries by working on the two following aspects:

1. simulation and analysis of wind turbine airfoils with highly accurate wall-resolved LES to serve the validation of lower fidelity methods and to deepen physical understanding,
2. implementation and validation of wall-modeled LES techniques to provide an affordable LES approach for high Reynolds numbers flows.

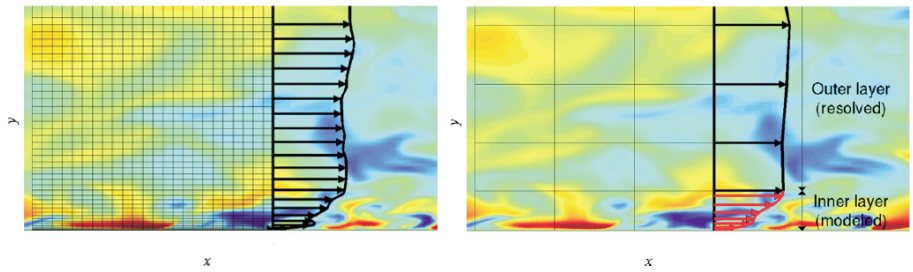


Figure 1.6: Schematic illustrating the inner layer modeling concept with the typical wall-resolved (left) and wall-modeled LES (right) meshes. Image taken from [69].

1.1 Wall-modeled LES

The large cost increase observed for LES of wall-bounded flows comes mainly from the inner part of the boundary layer, called the inner layer and that spans, by convention, from the wall to roughly 10% of the boundary layer thickness. At $Re = 1 \times 10^6$ for example, 99% of the total grid points will be placed in the inner layer although it represents only 10% of the boundary layer thickness [70]. The resolution of the inner layer scales as $Re^{1.8}$ according to a first estimate made by Chapman in 1979 [21] or as $Re^{1.9}$ according to a more recent evaluation made by Choi and Moin [23]. The resolution of the rest of the boundary layer, which is called the outer layer, also depends on the Reynolds number as the size of the largest eddies depends on the boundary layer thickness δ that decreases with the Reynolds number. Chapman estimated that the outer layer cost increases is as $Re^{0.4}$ [21]. This confirms that it is the resolution of the inner layer that confines the use of wall-resolved LES to low Reynolds number applications. Based on these findings, scientists already suggested in the late 70's to reduce the near-wall grid requirement by modeling the inner layer. Figure 1.6 shows the typical mesh coarsening allowed by switching from wall-resolved LES (wrLES) to wall-modeled LES (wmLES).

Two main methods are used to model the inner layer: the wall-stress method and the hybrid RANS/LES method. The wall-stress method, first employed in 1970 by Deardoff [29] and in 1975 by Schumann [83], is the simplest as it solves the LES equations in the entire domain and entirely avoids the resolution of the inner layer by imposing the wall shear stress τ_w based on data (*e.g.* velocity, pressure) taken at a certain distance from the wall.

The hybrid method, first introduced in 1997 by Spalart *et al.* [90] as Detached-Eddy Simulation (DES), solves RANS equations close to the wall and LES equations in the rest of the domain. This approach is more spread in the industry than the wall-stress approach. In an attempt to quantify the interest over the time for these two methods, Figure 1.7 compares the number of publications recorded per year that concern each of the two methods. Al-

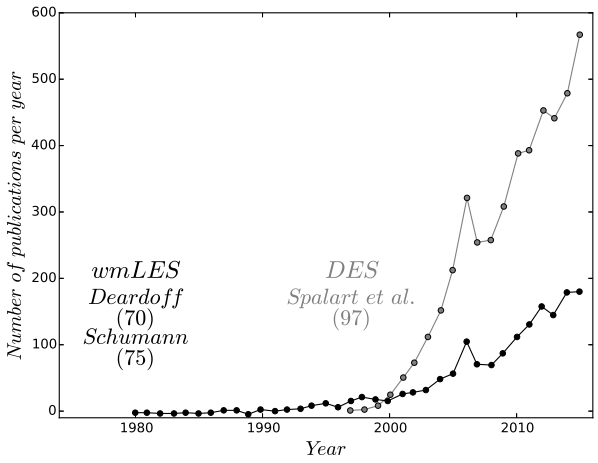


Figure 1.7: Yearly publications about wmLES and DES according to a search in Google Scholar for the words "large eddy"+"wall model"-"DES" for wmLES and "DES"+"Spalart"+"detached eddy" for DES. Data extracted from a figure in G. Park presentation in CTR [66].

though this approach is debatable to quantify precisely the importance of one topic, the observed trend is interesting. Figure 1.7 shows that, for the two methods, the number of publications has grown significantly since the year 2000. The DES approach can be seen to generate more interest than the wall-stress one. Still, the DES approach has some drawbacks when compared to the wall-stress method. The main challenge for the DES method lies in the computational connection between two regions that are described by different sets of equations; this often leads to unphysical mismatches at the connection. Furthermore, as the DES method relies on RANS close to the wall, it suffers from RANS drawbacks. DES is thus essentially interesting for largely separated flows, as its name implies. Therefore, this brings a resurgence of interest for the wall-stress approach. In this work, a wall-stress approach is implemented in a discontinuous finite element method, which is called discontinuous Galerkin method (DGM) and has generated increasing interest and adoption recently.

The enthusiasm for DGM comes from the fact this method provides high accuracy, low dissipation and low dispersion irrespective of the mesh type. Furthermore, it is highly scalable and thus better adapted for LES of large-scale industrial applications than the more widespread finite volume methods. To evaluate this interest, Figure 1.8 presents the number of publications published yearly along the last 15 years that were treating both CFD and DGM. It appears that this number has increased to a value of about 600 publications in 2015, which is of the same order of magnitude as for DES, as presented on Figure 1.7. To evaluate the relative importance of this value, Figure 1.8 presents as well the equivalent evolution for RANS and LES. Furthermore, in addition

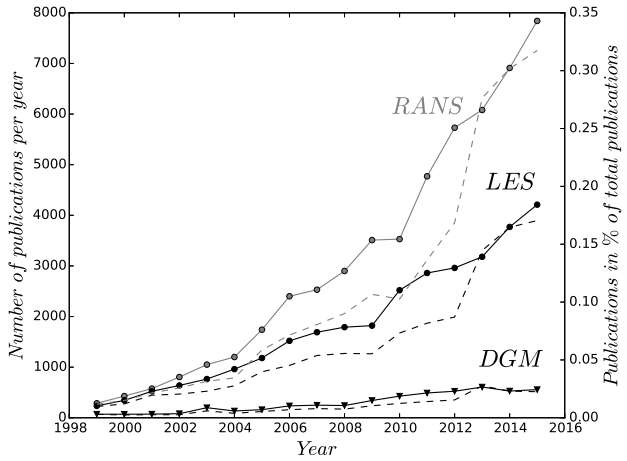


Figure 1.8: Yearly publications about RANS, LES and DGM according to a search in Google Scholar with the words "CFD"+"RANS" for RANS, "CFD"+"LES"+"large eddy" for LES and "Computational fluid dynamics"+"discontinuous Galerkin" for DGM. The number of publications are given in absolute values (solid lines, left y-axis) and also relatively to the global amount of publications recorded in Google Scholar database (dashed lines, right y-axis).

to the absolute values, the numbers of publications are also given relatively to the global amount of publications recorded in Google Scholar database. This representation allows to show that the number of publications about RANS, LES and DGM has drastically increased in the last years relatively to the total number of publications in all the research sectors. In 2015 for example, the importance of LES in the global research domain reached 0.20%.

The wall-stress approach is usually described by the type of wall model that it uses. The most basic models provide a direct link between the velocity at a certain distance from the wall and the wall shear stress, this is the case for models based on the law-of-the-wall as illustrated in Figure 1.9. However, as these models are based on assumptions that limit their use to simple flow configurations, more advanced models, such as the Two-Layer Model [6], are often preferred, even if they require to solve a system of equations. Although the errors due to the use of a basic or a more advanced model obviously have an impact on the accuracy of the global computation, the behavior of the numerical method on the coarse near-wall grid is at least as important. The main challenges in the use of this approach are thus identified as

- finding a wall model capable of predicting the correct wall shear stress
- mastering the interplay between the numerical method and the coarse near-wall mesh.

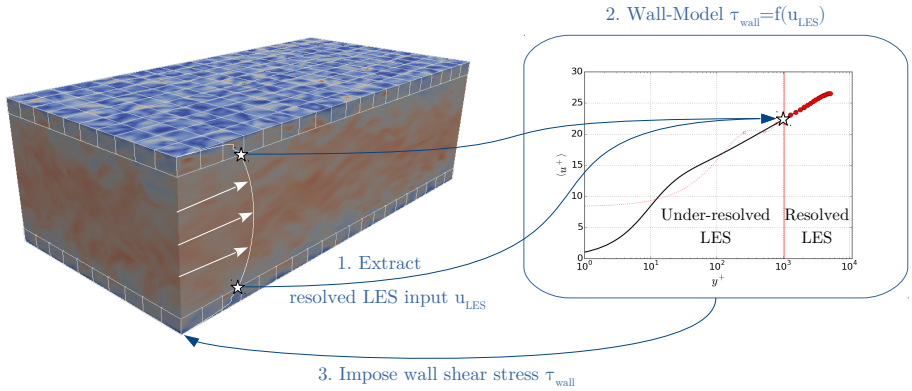


Figure 1.9: Sketch of the Wall-stress approach on the turbulent channel flow test case. The outer LES flow information (e.g. the velocity u_{LES}) at a fixed distance from the wall and a wall model (e.g. the Reichardt law-of-the-wall) are used to determine the wall shear stress τ_{wall}. The shear stress is then imposed as a wall boundary condition.

1.2 Objectives and structure of the thesis

The main goal of this thesis is to evaluate the relevance of the DG method for LES of industrial applications. This work is performed using a code named Argo [40]. During the thesis of C. Carton de Wiart [15], the code was validated on academic benchmarks such as the DNS of the Taylor-Green vortex [19] and the LES of homogeneous isotropic turbulence and channel flow [17]. The accuracy was demonstrated to be similar to that of dedicated academic codes. The code has also been applied to DNS and LES of industrial benchmarks featuring transitional flow [16, 41]. The present work thus positions itself in the continuity of the PhD thesis from C. Carton de Wiart, which demonstrated promising results for the turbomachinery sector. The present thesis goes a step further in the application of the method to industrial problems through a twofold effort consisting in

- entering in a new industrial sector, namely the wind sector, and
- reaching high Reynolds numbers by leveraging the wall models and their implementation in DGM.

Therefore, the first step in this thesis consisted in defining applications in the wind sector where DGM could bring an added value. As the strengths of DGM appear for LES and unstructured complex geometries, this task was a challenge. On the one hand, CFD is much less established in the wind sector than it is in the aircraft or the turbomachinery industry. Therefore, the RANS approach is already considered as expensive and the LES applications are scarce. On the other hand, these rare LES applications concern wind farm wake analyses [92] for which other high-order CFD approaches have already proven their interest and found their niche. As these approaches have high ac-

curacy and low computational cost on structured grids, DGM can not compete in cases over flat terrains. However, DGM could stand out for cases where an unstructured mesh is needed, as for wake analyses over complex terrains.

Before the implementation and the test of the wmLES techniques, it is important to evaluate DGM for wall-resolved LES of wind applications. To this end, wrLES of low Reynolds number airfoils are performed. In the previous work of C. Carton de Wiart, two airfoils had been studied already with Argo, one with DNS and one with wrLES. As these calculations were compared to other simulations performed with similar CFD approaches, the LES strategy was verified but not validated. In this study, these verification and validation efforts are pushed further by comparing the results to experimental as well as to drastically different numerical approaches that are largely used in the wind sector.

As explained before, in the author's view, there are two main challenges in the use of the wall-stress approach. These challenges are addressed separately. The approach is first tested on a canonical flow to focus on the characterization of the DGM numerical response on the coarse near-wall mesh and to define best practice guidelines. Different wall models are then compared on a high Reynolds number airfoil case. The thesis is organized as follows.

Chapter 2: Wall models and discontinuous Galerkin method
Chapter 2 presents a review of the most largely used wall models within the wmLES community. Based on a discussion about their expected accuracy and computational cost, some models are chosen to be implemented in Argo DG. In order to understand how exactly the models are implemented, the discontinuous Galerkin method is reviewed. In addition to highlighting the implementation carried out in this work, this allows to compile a list of constraints and objectives on the usage of wmLES that are specific to the present implementation.

Chapter 3: Low Reynolds number airfoils
Chapter 3 presents wall-resolved LES of two low Reynolds number airfoils: the S826 and the Eppler 387. Three complex flow phenomena are studied, namely the laminar separation bubble, the lift hysteresis and the stall cells. For the two airfoils, the wrLES results are compared to both experimental and numerical databases. These comparisons permit to highlight the complexity to provide "test-parameter-free" airfoil polars and the consequent difficulty in validating CFD approach based on experimental database. The chapter concludes by suggesting tracks to overcome these complexities by experimental and numerical collaborations. The work on the S826 has been published in "AIAA Conference Series"[33] and the work on the E387 in "Journal of Physics: Conference Series"[34].

Chapter 4: Turbulent channel flow
Chapter 4 evaluates the wall-modeled LES method on the turbulent channel flow. In addition to the validation of the wmLES approach, this chapter aims at defining guidelines on the use of wmLES in DGM through a rigorous sensitivity analysis. Various parameters are studied such as the wall model input location and the polynomial degree. This work has been published in the journal "Physics of Fluids" [31].

Chapter 5: High Reynolds number airfoils
Chapter 5 presents first a wall-modeled LES of an airfoil at high Reynolds number and at near-stall condition. The airfoil that is considered is the NACA 4412 airfoil, a widely used test case for turbulence modeling validation. To evaluate the quality of the simulation, a wall-resolved LES of the exact same test case is performed. In addition to providing a deep analysis of the airfoil aerodynamics, this chapter uses the data to compare different wall models and to conclude on their respective ability to represent a turbulent boundary layer subject to an adverse pressure gradient. This work, presented at DLES11 conference, has been selected for a special edition in the journal "Flow, Turbulence and Combustion" and is currently under review. This work also permitted to obtain a grant from PRACE for reproducing the computation on a larger span extent. As these simulations are currently ongoing on the BlueGene/Q machine *JuQueen* at the Jülich Supercomputing Centre, only a few preliminary results are presented in this work.

CHAPTER 2

WALL MODELS AND DISCONTINUOUS GALERKIN METHOD

This chapter presents a review of the most widely used wall models within the wmLES community. Based on a discussion about their expected accuracy and computational cost, some models are chosen to be implemented in Argo DG. In order to understand how exactly the models are implemented, the discontinuous Galerkin method is reviewed. In addition to highlight the implementation carried out in this work, this allows to compile a list of constraints and objectives on the usage of wmLES that are specific to the present implementation.

2.1 Modeling the boundary layer

As presented in Chapter 1, the wall-resolved LES of wall-bounded flows at Reynolds numbers that are relevant for wind turbine, turbomachinery or aircraft design ($Re \geq 10^6$) currently requires too much resources to be used in practice. The near-wall grid requirements of LES are indeed prohibitive; this work thus aims at alleviating those by the use of wall-modeled LES (wmLES).

To find a wall model that is able to reconstruct the wall shear stress based on data taken some distance above the wall, it is important to assimilate a few concepts about boundary layer flows. Therefore, the concepts of turbulence, boundary layer and wall modeling, which have been introduced in Chapter 1, are described here in a more detailed manner.

2.1.1 Boundary layer characterization

Away from a wall boundary, the flow can be considered as potential and it exhibits velocity magnitudes that are of the same order as the freestream velocity u_∞. In such a scenario, the viscous effects are confined to a thin layer above the boundary. The viscous effects allow the flow to stick to the surface, in what is called a **no-slip condition**; the velocity then reaches the velocity of the wall, $u(x, y = 0) = 0$ for stationary objects. The development of this region is shown in Figure 2.1 in the canonical case of a uniform inflow above a flat plate. In 1904, Prandtl called this region the **boundary layer** [72]. The maximum velocity that is reached at the upper edge of the boundary layer is called the **edge velocity** and is denoted $\boldsymbol{u_e(x)}$. Note that, in the case of the flat plate presented on Figure 2.1, this velocity is constant and $u_e(x) = u_\infty \ \forall x$. This will however not be the case for the flow over an airfoil, as it will be discussed later on. In engineering, and in this work, the **boundary layer thickness $\boldsymbol{\delta}$** is defined as the distance from the wall where the velocity reaches $u(x, \delta) = 0.99\, u_e(x)$. The **displacement thickness $\boldsymbol{\delta^*}$** and the **momentum thickness $\boldsymbol{\theta}$** are obtained by the following integrals over the wall normal direction y

$$\delta^*(x) = \int_0^{\xi(x)} \left(1 - \frac{u(x,y)}{u_e(x)}\right) dy \tag{2.1}$$

$$\theta(x) = \int_0^{\xi(x)} \frac{u(x,y)}{u_e(x)} \left(1 - \frac{u(x,y)}{u_e(x)}\right) dy \tag{2.2}$$

where $\xi(x)$ is taken larger than $\delta(x)$. These definitions are solely valid for cases where the velocity above the boundary layer is uniform in y. For boundary layers with accelerating or decelerating $u_e(x)$ (*e.g.* on airfoils), the potential flow outside the boundary layer is not uniform in the wall normal direction; one then uses, as $\xi(x)$, the location of maximum velocity and, as $u_e(x)$, the value of the velocity there.

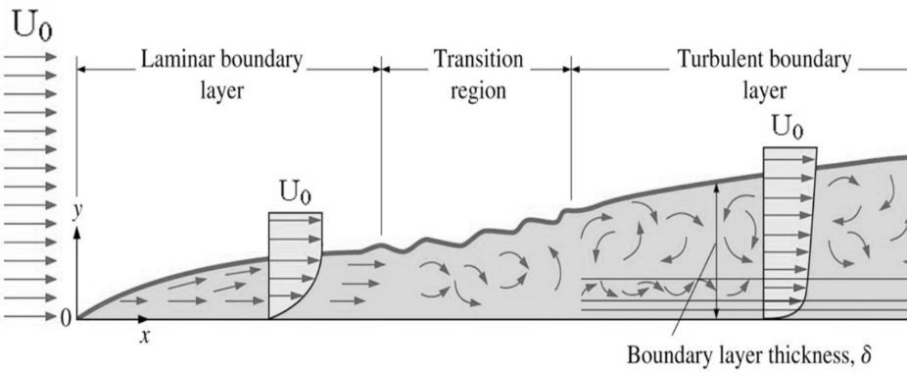


Figure 2.1: Schematic of the boundary layer development over a smooth flat plate. Image taken from [1]. The freestream velocity u_∞ is here denoted U_0.

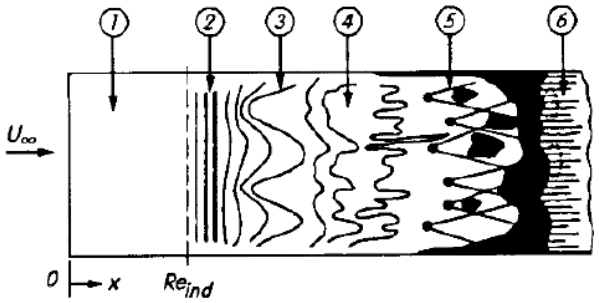


Figure 2.2: Schematic of laminar–turbulent transition in the attached boundary layer over a smooth flat plate: 1-stable laminar flow, 2-unstable Tollmien–Schlichting waves, 3-three–dimensional waves and vortex formation, 4-vortex decay, 5-formation of turbulent spots, 6-fully turbulent flow. Image and legend taken from Schlichting [79] after White [105]. The freestream velocity u_∞ is here denoted U_∞.

Therefore, the value and the position of $u_e(x)$ on an airfoil are difficult to define exactly in practice. This also comes from the fact that the set of data is discrete. Several methods are thus used in the literature, as clearly presented in [97], and it is important to state precisely which method is considered. In this work, $u_e(x)$ is taken as the velocity at the position where the velocity gradient normal to the surface is minimum.

As shown in Figure 2.1, the boundary layer thickness increases on the flat plate from the extreme left, the leading edge, to the right. Within the boundary layer, the two types of flow described in Chapter 1 are observed with a laminar flow close to the leading edge that becomes unstable and transitions to a turbulent flow. The two regions follow quite different physics and are differentiated by using the terms laminar and turbulent boundary layers.

The mechanism of transition is complex, to the point that some consider it as the "most important unsolved problems of fluid mechanics"[78]. Its thorough analysis is therefore far beyond the scope of this work, but it is worth summarizing the main concepts. The process of transition over a flat plate is presented in Figure 2.2. It is initiated by the development of two-dimensional Tollmien-Schlichting instabilities. Three-dimensional instabilities then rapidly develop and lead to characteristic Λ-structures. The Λ-vortices break-down into smaller structures and turbulent spots appear at the wall. These turbulent spots rapidly grow and lead to the fully turbulent flow. This complete transitional process is called **natural transition**.

The transition strongly depends on the flow parameters, the main one being the Reynolds number. For the low Reynolds number airfoils studied in Chapter 3 for example, the laminar region can span over 60% of the total airfoil chord length, while it will be of a few % for the high Reynolds number air-

foils studied in Chapter 5. The freestream turbulence intensity and the wall roughness can also strongly affect the transition process, and can even lead to a by-pass of the steps 2 to 4 presented in Figure 2.2. One then speaks of **by-pass transition**. In this work, a third type of transition process will be observed where the flow separates before the transition and the transition then occurs in the separated shear layer. It is called the **separated flow transition**, and it can include aspects of both natural and by-pass transition, as well as perturbations similar to the Kelvin-Helmholtz instabilities observed in free shear layers.

As this work aims at finding a model to represent the boundary layer observed on high Reynolds number airfoils, it focuses on the characterization of turbulent boundary layers. However, it is interesting to observe a few more characteristics of laminar and turbulent boundary layers.

In the laminar boundary layer, the difference of velocity between the adjacent flow layers produces a shear stress that is proportional to the fluid viscosity and to the velocity gradient as

$$\frac{\tau(y)}{\rho} = \nu \frac{du}{dy}. \tag{2.3}$$

In the case of the turbulent boundary layer, the flow unsteadiness increases the exchange of momentum between the flow layers. This additional shear stress is called the Reynolds stress and it depends on the fluctuation of the velocity. Considering a 2D case with the velocity in the streamwise direction u given as the sum of a mean velocity $\overline{u}$ and a fluctuating velocity u', and the velocity in the normal direction v given in a similar way $v = \overline{v} + v'$, the total stress is then given by

$$\frac{\tau(y)}{\rho} = \nu \frac{d\overline{u}}{dy} - \overline{u'v'}. \tag{2.4}$$

As this turbulent mixing decreases close to the wall, considering hydraulically smooth wall cases, the turbulent boundary layer presents a near-wall region that is similar to a laminar region and the wall shear stress τ_w is given by

$$\frac{\tau_w}{\rho} = \frac{\tau(0)}{\rho} = \nu \frac{d\overline{u}}{dy}. \tag{2.5}$$

The relative importance of the viscous and the Reynolds stresses within the turbulent boundary layer is detailed in the next section.

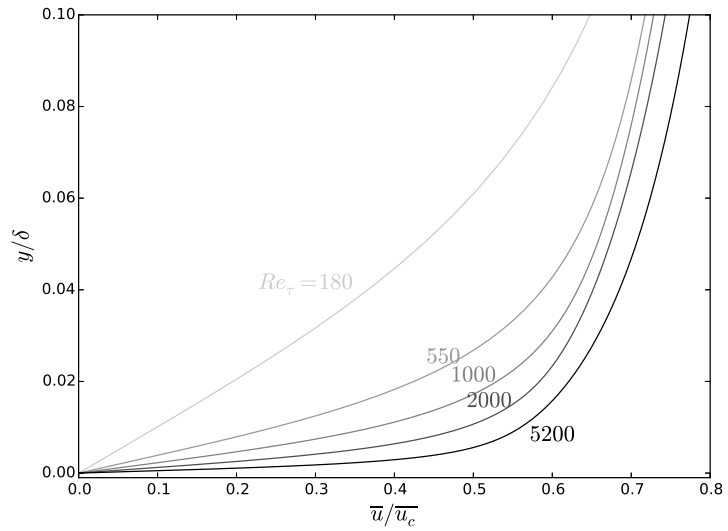


Figure 2.3: Profiles of the velocity in the turbulent channel flow for different Reynolds numbers: $Re_\tau = 180, 550, 1000, 2000$ and 5200. The data come from several DNS performed by Lee and Moser [51].

2.1.2 Universal velocity profile

This section describes the turbulent boundary layers that have a constant edge velocity u_e. The accelerated or decelerated boundary layers, where $u_e(x)$ respectively increases or decreases are described in Section 2.1.4.

For the description of the turbulent boundary layer, it is interesting to examine the flow in a channel. The turbulent channel flow is a well-known test case in which a fully developed turbulent flow evolves between two walls that are parallel and separated by a distance of 2δ. Figure 2.3 shows the velocity profiles obtained by DNS in such a channel for different Reynolds numbers. In that figure, the normal wall distance y and the mean velocity $\overline{u}$ are both non-dimensionalized. The boundary layer thickness δ is used for y and the velocity at the center of the channel $\overline{u_c}$ is used for $\overline{u}$. Figure 2.3 introduces a Reynolds number based on the shear stress at the wall $\boldsymbol{Re_\tau}$. For this Reynolds number, δ is chosen as the characteristic distance and the wall shear stress τ_w is manipulated to obtain the dimensions of a velocity. The obtained velocity is called the **friction velocity** $\boldsymbol{u_\tau}$. The friction velocity and the resulting Reynolds number are given by the following two relations

$$u_\tau = \sqrt{\frac{|\tau_w|}{\rho}} \tag{2.6}$$

$$Re_\tau = \frac{\delta\, u_\tau}{\nu}. \tag{2.7}$$

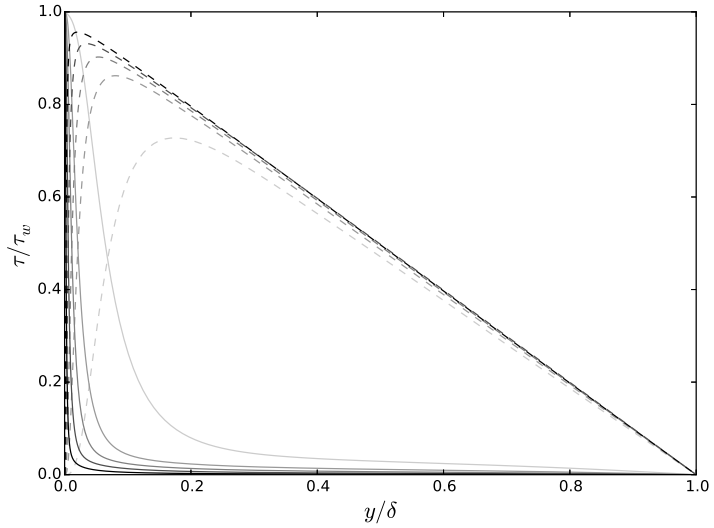


Figure 2.4: Profiles of the viscous (solid line) and Reynolds (dashed line) shear stresses in the turbulent channel flow for different Reynolds numbers: $Re_\tau = 180$, 550, 1000, 2000 and 5200. The lines are colored from light gray to black for increasing Reynolds numbers. The data come from several DNS performed by Lee and Moser [51].

Figure 2.3 shows only the first 10% of the boundary layer, which corresponds to the region called **inner layer**. For a given δ, the velocity evolution from the wall is steeper for the large Reynolds numbers. Therefore, the velocity gradient $d\overline{u}/dy$ increases as the Reynolds number increases and the size of the smallest grid element necessary to capture this gradient reduces drastically. As introduced in Chapter 1, the inner layer is therefore the region that needs to be modeled to reduce the large grid resolution dependance to the Reynolds number.

Using the data from the five DNS of the turbulent channel flow, Figure 2.4 presents the evolution of the viscous and the Reynolds shear stresses from the wall to the center of the channel, *i.e.* $0 \leq y \leq \delta$. The shear stress is non-dimensionalized using the wall shear stress. On this figure, the viscous shear stress is maximum at the wall, then reduces quickly and becomes almost negligible. This reduction of the viscous stress is even faster as the Reynolds number increases. The Reynolds stress, for its part, is zero at the wall and then increases to become dominant. Therefore, it appears that in the close vicinity of the wall, three distinct regions can be defined. The first region is dominated by the viscous stresses. The second region is influenced by both viscous and Reynolds stresses. The third region is dominated by the Reynolds or turbulent stresses.

Figure 2.5 and Figure 2.6 present the same profiles as in Figure 2.3 and Figure 2.4 but in different units. Note that the curves collapse. The velocity profiles are presented in wall units, *i.e.* using the friction velocity to non-dimensionalize the tangential velocity $\overline{u}$ and the normal wall distance y as

$$u^+ = \frac{\overline{u}}{u_\tau} \tag{2.8}$$

$$y^+ = \frac{y\, u_\tau}{\nu}. \tag{2.9}$$

For the viscous and Reynolds stresses, rather than normalizing them by τ_w as in Figure 2.4, they are here normalized by using the total local shear $\tau(y)$ to highlight their respective importance. They are also presented as function of the dimensionless wall distance y^+, to help the definition of the different regions.

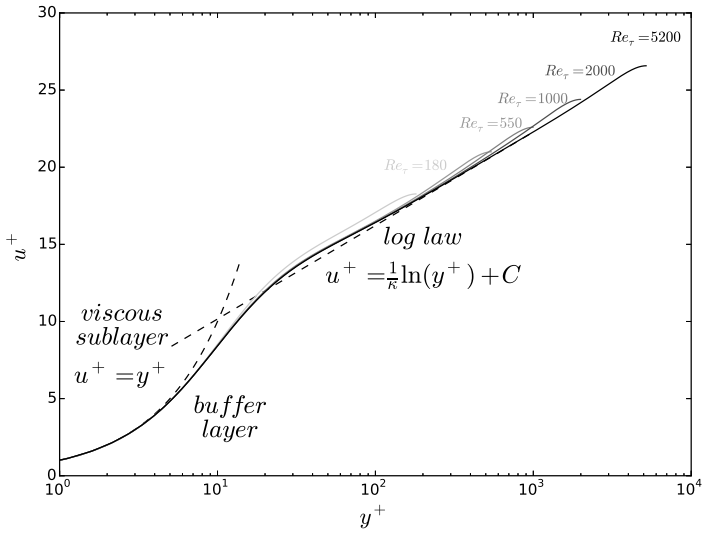


Figure 2.5: Same data as in Figure 2.3 non-dimensionalized using the wall units to highlight the universal velocity profile and the different constitutive layers. The dashed lines denote the expected theoretical profiles for the viscous and log regions.

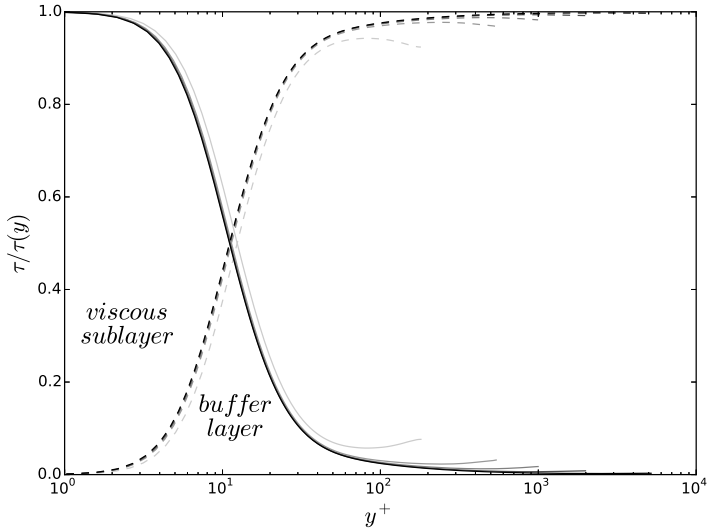


Figure 2.6: Same data as in Figure 2.4 non-dimensionalized using the local total shear $\tau(y)$ to highlight the relative importance of the viscous (solid line) and Reynolds (dashed line) stresses. The wall distance is given in wall units to facilitate the definition of the different constitutive layers.

Based on these two figures, the turbulent boundary layer can be divided in three regions. Close to the wall ($y^+ < 5$), the viscous stresses are dominant and the dimensionless mean streamwise velocity varies linearly with the normal wall distance as given by

$$u^+ = y^+. \tag{2.10}$$

After this first zone called the **viscous sublayer**, the second zone is a **buffer layer** ($5 < y^+ \lesssim 100$) where viscous and turbulent stresses are of the same order of magnitude. Further from the wall ($y^+ \gtrsim 100$), a third zone starts where the viscous stresses become negligible compared to the turbulent stresses. In this third zone, two sub-regions are defined.

In the first sub-region, called the **log region**, the velocity can be shown to follow the logarithm of the wall distance

$$u^+ = \frac{1}{\kappa} \ln\left(y^+\right) + C. \tag{2.11}$$

where κ and C are two constants. The value of these constants is the subject of many works in the literature, as discussed further in Section 2.1.3. The extent of the log region varies with the Reynolds number. Marusic *et al.* [57] mention that the log law applies to a section of the boundary layer given by

$$3\sqrt{\frac{\delta\, u_\tau}{\nu}} \leq y^+ \leq 0.15\frac{\delta\, u_\tau}{\nu}. \tag{2.12}$$

Table 2.1 uses this relation to present the limits of the log region for three of the DNS used in Figure 2.3 to Figure 2.6. Note that, for $Re_\tau \leq 1000$, the log region practically vanishes.

Re_τ	y^+_{min}	y^+_{max}
1000	95	150
2000	134	300
5200	216	780

Table 2.1: Log region min. and max. y^+ values according to the relation Eq. (2.12) for the three higher Reynolds numbers considered in the previous figures.

The velocity profile in the viscous, buffer and log regions can be expressed as a function of the dimensionless wall distance of the form

$$u^+ = f\left(y^+\right), \tag{2.13}$$

which is called the **law-of-the-wall**.

The second sub-region of the turbulence dominated region spans from the end of the purely log region to the end of the boundary layer. This region

differs from the law-of-the-wall because, as it can be observed in Figure 2.5, there is an added velocity profile $G\left(\frac{y}{\delta}\right)$ that presents a "S-shape". That is thus a function of the global/geometrical variable $\left(\frac{y}{\delta}\right)$, and not of y^+. In 1956, Coles [26] proposed the following composite velocity profile

$$u^+ = f\left(y^+\right) + G\left(\frac{y}{\delta}\right). \tag{2.14}$$

In that region, the velocity profile depends on both the inner variable y^+ and the outer variable y/δ. As $f(y^+) = \frac{1}{\kappa}\ln y^+ + C$, one also obtains the **defect law**, valid for the entire third (*i.e.* turbulence dominated) region

$$\frac{\overline{u_e} - \overline{u}}{u_\tau} = -\frac{1}{\kappa}\ln\left(\frac{y}{\delta}\right) + G\left(1\right) - G\left(\frac{y}{\delta}\right) = F\left(\frac{y}{\delta}\right). \tag{2.15}$$

Note that the inner layer is defined in this work as spanning from the wall to 0.1δ, regardless of the Reynolds number. This arbitrary choice is made to be in the line of most of the textbooks [71, 79]. And the wmLES approach is defined as a modeling of the inner layer. However, as we will see later, in some cases where the flow follows the law-of-the-wall further than 0.1δ, the wall model can be applied for $y \geq 0.1\delta$.

2.1.3 Quasi analytical wall models

The simplest wall model uses the logarithmic law-of-the-wall Eq. (2.11) in the near-wall turbulent region. As this law joins the dimensionless mean streamwise velocity u^+ and the normal wall distance y^+, it can be used to predict directly the wall shear stress τ_w for given velocity u and wall distance y. However, as this law is only valid for a portion of δ given by Eq. (2.12), the location where the input velocity can be taken is constrained. To alleviate this constraint, different laws-of-the-wall tend to also model the area closer to the wall by providing a smoothing between the linear and the log regions. Such well-known relations are Reichardt's law-of-the-wall [79]

$$\begin{aligned} u^+ = \frac{1}{\kappa}\ln\left(1+\kappa y^+\right) + \left(C - \frac{1}{\kappa}ln\left(\kappa\right)\right) \\ \left(1 - \exp\left(\frac{-y^+}{11}\right) - \frac{y^+}{11}\exp\left(\frac{-y^+}{3}\right)\right), \end{aligned} \tag{2.16}$$

and Spalding's law-of-the-wall [91]

$$y^+ = u^+ + \exp\left(-\kappa C\right)\left(\exp\left(\kappa u^+\right) - \sum_{n=0}^{4}\frac{\left(\kappa u^+\right)^n}{n!}\right). \tag{2.17}$$

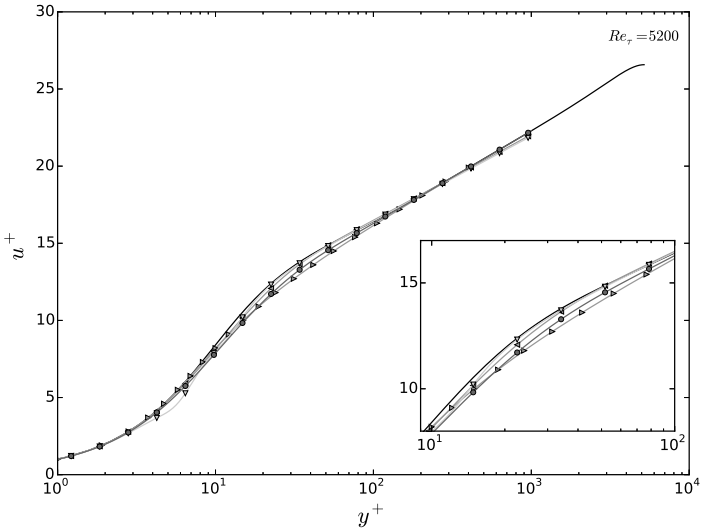


Figure 2.7: Comparison of different laws-of-the-wall with the velocity profile obtained by DNS for the turbulent channel case at $Re_\tau = 5200$ [51] (solid line). Eq. (2.16) is plotted for two different sets of constants: $\kappa = 0.38$ - $C = 4.1$ (dark gray line with circles) and $\kappa = 0.41$ - $C = 5.2$ (gray line with left triangles). Eq. (2.17) is plotted for $\kappa = 0.38$ - $C = 4.1$ (gray line with right triangles) and Eq. (2.18) is plotted for $\kappa = 0.42$ (light gray line with down triangles) as suggested in [2]. The small inset presents a zoom on the blending region.

Another wall model, which is used by commercial codes (see *e.g.* [2]), provides a blending as

$$u^+ = \exp(\alpha)\left(y^+\right) + \exp\left(\frac{1}{\alpha}\right)\left(\frac{1}{\kappa}\ln Ey^+\right) \tag{2.18}$$

$$\alpha = \frac{-a\left(y^+\right)^4}{1+by^+} \tag{2.19}$$

where E, a and b are constants chosen as $E = 9.79, a = 0.01, b = 5$.

Figure 2.7 compares these three relations to the DNS run at the highest available Reynolds number $Re_\tau = 5200$. For Reichardt's law, two widely used sets of constants are compared, namely $\kappa = 0.41$ and $C = 5.2$, as usually given in textbooks, and $\kappa = 0.38$ and $C = 4.1$, as suggested by more recent works (see *e.g.* [65]). The zoom on the blending region shows that Spalding's blending is not as good as Reichardt's one. For $y^+ \simeq 700$, Reichardt's law with the most recent constants appears to provide the best match.

Finally, note that another widely used model is based on Werner and Wengle's formula [104]. In comparison to the previous models, this model has the ad-

vantage of providing the wall shear stress directly, without the intermediate step of looking up the velocity profile. The model is given as

$$|\tau_w| = \begin{cases} \frac{2\ \mu\ |u_m|}{y} & u_m \leq \beta \\ \rho \left[\frac{1-B}{2} A^{\frac{1+B}{1-B}} \left(\frac{\mu}{\rho y} \right)^{1+B} + \frac{1+B}{A} \left(\frac{\mu}{\rho y} \right)^{B} |u_m| \right]^{\frac{2}{1+B}} & u_m > \beta \end{cases} \tag{2.20}$$

where $\beta = \frac{\mu}{2\rho y} A^{\frac{2}{1-B}}$, μ is the dynamic viscosity and u_m is the averaged velocity between the wall and the wall distance y. A and B are two constants taken as $A = 8.3$ and $B = 1/7$ [2].

All the presented analytical laws are easy to implement and require low computational time. However, they are based on the law-of-the-wall, which was so far presented for a boundary layer subjected to a constant edge velocity as observed on a flat plate. The next section seeks the validity of these models for accelerated and decelerated boundary layers as observed on airfoils.

2.1.4 Velocity profile for boundary layers subjected to a pressure gradient

As presented in Figure 2.8, the boundary layer over an airfoil presents, as for the flat plate, a laminar region followed by a transition to turbulence. However, the velocity $u_e(x)$ is no longer constant and the boundary layer is accelerated or decelerated. These velocity and pressure gradients are imposed by the outer flow and depend on the airfoil geometry, the Reynolds number and the angle of attack. Figure 2.8 can be used to define some important governing parameters.

When approaching the airfoil, the flow splits between the lower and the upper side at what is called the stagnation point. For an angle of attack of zero, the stagnation point is located near the leading edge of the airfoil. For higher angles of attack, the stagnation point moves towards the airfoil lower side, as presented in Figure 2.8. At this point, the velocity is zero and the static pressure is called the stagnation pressure p_0.

Based on this stagnation pressure, the pressure evolution over the airfoil is commonly expressed as a dimensionless **pressure coefficient C_p** given by

$$C_p = \frac{p - p_\infty}{p_0 - p_\infty} = \frac{p - p_\infty}{\frac{1}{2}\rho u_\infty^2} \simeq 1 - \frac{u_e^2}{u_\infty^2}, \tag{2.21}$$

where p is the static pressure on the airfoil and p_∞ and u_∞ are the freestream static pressure and velocity.

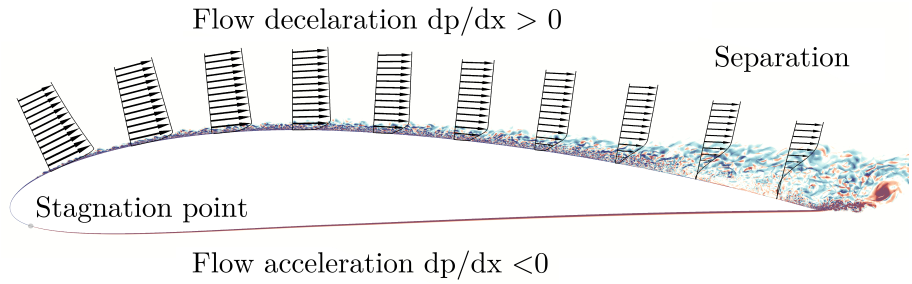


Figure 2.8: Illustration of the boundary layer evolution over an airfoil. The image is taken from a simulation of the NACA4412 at an angle of attack of 12° that will be presented in details in Chapter 5.

From the stagnation point where $C_p = 1$ and towards the upper side of the airfoil, there is a rapid increase of the velocity $du_e/dx \gg 0$ associated with a large pressure drop $dp/dx \ll 0$. The velocity then slowly decreases $du_e/dx < 0$ and the pressure increases $dp/dx > 0$ towards the trailing edge. The upper surface is therefore referred to as the suction side. The deceleration $du_e/dx < 0$ can be eventually such that a backflow is encountered. That is then a case of separation, as observed in Figure 2.8. On the lower surface, which is called the pressure side, the velocity increases slowly $du_e/dx > 0$ and the pressure decreases $dp/dx < 0$. The increase in velocity stabilizes the flow and the negative pressure gradient (PG) is therefore called **favorable PG**. As the positive PG on the suction side can lead to flow separation, which is associated to a large performance drop, it is called an **adverse PG (APG)**. The capture of APG effects is, as of today, one of the biggest challenges in wall modeling.

One complexity in APG modeling is that its influence on the boundary layer is different for low and high Reynolds numbers. Figure 2.9 shows the impact of an APG on the boundary layer development over the same bump geometry for two Reynolds numbers. The bump, which is drawn in light gray in the small figures, was designed by Dassault Aviation to reproduce a typical APG observed on an airfoil at high angle of attack [9]. The test case was studied first experimentally at $Re_\tau = 6500$ [9] and then simulated by DNS at the (then) highest numerically accessible Reynolds number, namely $Re_\tau = 395$ [56]. Figure 2.9 provides the pressure coefficient evolutions over the bump for the two Reynolds numbers. In both cases, the bump induces first a favorable pressure gradient until the top of the bump where $C_p \simeq -1.5$ but the APG is slightly different with, at low Reynolds number, a plateau that reveals a separated region. The boundary layer velocity profiles are shown for both Reynolds numbers at different positions in the APG region. The profiles are given in wall units.

At the higher Reynolds number, a common log region is observed in all of the profiles, effectively decoupling the outer layer, which is highly impacted by the APG, from the inner layer. The latter appears to behave in the universal way presented previously, *i.e.* the law-of-the-wall with $u^+ = f(y^+)$. Already in 1949, Ludwieg and Tillman [54] observed that the law-of-the-wall is still valid for accelerated and decelerated boundary layers at high Reynolds number. In 1954, Clauser [25] showed that the defect law can be described by a relation equivalent to Eq. (2.15) where the flow velocity depends on $\frac{y}{\delta}$ but also on a parameter $\boldsymbol{\beta = \delta^* \frac{dp/dx}{\tau_w}}$, called the **Clauser parameter**. Based on this parameter, Clauser introduced the concept of the **near-equilibrium boundary layer**, for which β is constant in x and that follows a universal velocity profile when expressed in defect law Eq. (2.15) for the turbulence dominated region.

At the lower Reynolds number, there is no logarithmic layer as discussed in Section 2.1.2, and the impact of the APG goes up to the wall. A wall model developed and/or validated on the basis of low Reynolds number data is therefore not applicable to high Reynolds number cases; and conversely.

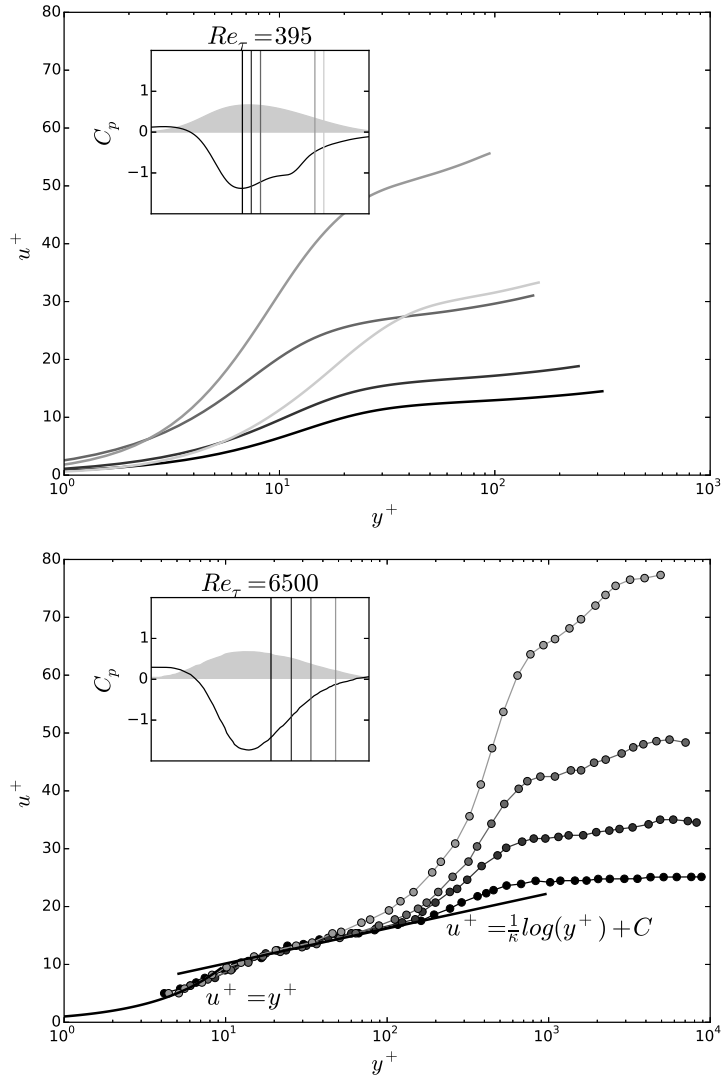


Figure 2.9: Impact of an adverse pressure gradient at low and high Reynolds numbers. The small inlay presents the geometry (gray area), the pressure coefficient (black curve) and the locations corresponding to the velocity profiles plotted in the main figure (vertical lines colored from black to gray). The low Reynolds number results are on the top (the data come from the DNS database [49] and have been analyzed by the author). The experimental high Reynolds number results are on the bottom (the data have been extracted from Bernard *et al.* [9]).

2.1.5 Wall models for boundary layers subjected to a pressure gradient

Although the laws presented in Section 2.1.3 have been developed for boundary layers subjected to a constant edge velocity, they should also be applicable to boundary layers subjected to a PG, as long as the velocity profile features a log region (high Re) and as the wall model input falls within the inner layer. However, many authors have developed more elaborate expressions that explicitly take the PG into account. Brionnaud *et al.* obtained promising results on a detached flow over an aircraft wing [12] using the **Generalized law-of-the-wall** of Shih [86]

$$\overline{u} = \frac{\tau_w}{|\tau_w|} u_\tau f_1(y^+) + \frac{p^+}{|p^+|} u_\tau p^{+\frac{1}{3}} f_2(y^+ p^{+\frac{1}{3}}), \tag{2.22}$$

$$p^+ = \frac{\nu}{\rho u_\tau^3} \frac{dp}{dx} \tag{2.23}$$

where p^+ is the pressure gradient in wall units and f_1 and f_2 are calibrated fifth-order polynomials. For the sake of clarity, these functions and their coefficients are not given here but note that improved coefficients have been proposed by Thiry [95] to remove the discontinuities observed in the original function.

Shih's approach is interesting as it has basically the same cost as the analytical models described in Section 2.1.3. However, the most widely used approach is the **Two-Layer Model (TLM)**, proposed by Balaras *et al.* [6]. The TLM couples LES in the free field to the incompressible turbulent boundary layer equations near the wall. These equations correspond in the Navier-Stokes equations where a Reynolds average has been performed and where the boundary layer height is assumed small compared to the flow characteristic length. This allows to neglect a few terms and to obtain a pressure that is constant through the boundary layer height. Thus, the pressure gradient in the directions parallel to the wall can be provided as input to the problem. The full TLM equations (split according to common wmLES simplifications) are recalled here

$$\frac{\partial}{\partial x_2}\left((\nu + \nu_t)\frac{\partial \bar{u}_i}{\partial x_2}\right) = F_i \qquad i = 1,3 \tag{2.24}$$

$$F_i = \frac{1}{\rho}\frac{\partial \bar{p}}{\partial x_i} + \frac{\partial \bar{u}_i}{\partial t} + \frac{\partial}{\partial x_j}(\bar{u}_i \bar{u}_j) \qquad j = 1,2,3 \tag{2.25}$$

where $(x_1, x_2, x_3) = (x, y, z)$ are the streamwise, wall-normal, and spanwise directions, $(u_1, u_2, u_3) = (u, v, w)$ are the corresponding velocity components, p is the pressure, and t is the time.

The eddy viscosity ν_t is found by using a RANS-type model. This model differs slightly from one author to another. Table 2.2 gathers the most current relations. Note that the only relations in this table that have the correct behavior close to the wall are the ones used by [14] and [102], as ν_t has a y^{+^3}

Balaras *et al.* [6]	$\nu_t = (\kappa y)^2(1-\exp(-(y^+/25)^3))\lvert\frac{\partial u}{\partial y}\rvert$
Choi and Moin [14] Kawai and Asada [46]	$\nu_t = \kappa y u_\tau(1-\exp(-y^+/17))^2$
Wang and Moin [102] Chen *et al.* [22]	$\nu_t = \kappa y u_\tau(1-\exp(-y^+/19))^2$
Duprat *et al.* [30]	$\nu_t = \kappa y u_{tp}\left(\alpha + y_{tp}(1-\alpha)^{3/2}\right)^\beta \left(1-\exp(\frac{-y_{tp}}{1+A*\alpha^3})\right)^2$ $u_{tp} = \sqrt{(u_\tau)^2+(u_p)^2}$ $u_p = (\lvert\mu/\rho^2 dp/dx\rvert)^{1/3}$, $y_{tp} = \frac{y^+ u_{tp}}{u_\tau}$ $\alpha = u_\tau/u_{tp}$, $A = 17$, $\beta = 0.78$
Bocquet *et al.* [10]	$\nu_t = (\kappa y)^2(1-\exp(-y^+/26))^2\lvert\frac{\partial u}{\partial y}\rvert$

Table 2.2: Turbulent closure equations used in the wmLES community.

behavior when $y^+ \to 0$. Furthermore, when connecting the TLM to LES, as the LES is already capturing much of the turbulent shear stress, the ν_t given in Table 2.2 needs to be reduced, as suggested in Medic *et al.* [60].

To reduce the computational cost of the full TLM approach, these equations have often been simplified by removing the time dependence and the convective terms (*i.e.* $F_i = \frac{1}{\rho}\frac{\partial \bar{p}}{\partial x_i}$). Table 2.3 lists the most common simplifications done in the TLM equations as well as the tests cases on which the methods have been evaluated.

Although good results have been obtained on several cases, a recent review from Larsson *et al.* [48] points out that the TLM should not be used without the convective terms as they can be large and of the same order of magnitude as the pressure gradient. Both terms approximately balance each other in the inner layer above the viscous sublayer and the inner layer dynamics are much faster than the outer layer ones. This brings Larsson *et al.* to the conclusion

Authors	TLM neglected terms	Test cases
Balaras *et al.* [6]	n.a	TCF (+rotating), square duct
Choi and Moin[14]	n.a.	TCF, backward step
	time, convective, PG	TCF, backward step
Bocquet *et al.* [10]	time, convective	TCF
Choi *et al.* [22]	convective	TCF, periodic hill
Lodato *et al.* [53]	time, convective	TCF, periodic hill
Duprat *et al.* [30]	time, convective	TCF, periodic hill

Table 2.3: Simplifications made in the Two-Layer Model and the applications performed with the simplified model. TCF stands for turbulent channel flow.

that, for non equilibrium cases, it would be more accurate to use the TLM supposing equilibrium conditions (*i.e.* $F_i = 0$) rather than only neglecting the convective terms.

More extensive reviews of the different wall models are provided by Larsson *et al.* [48] and Piomelli *et al.* [69]. In his PhD thesis [95], O. Thiry also provides a comprehensive review of the existing wall models.

2.2 Numerical approach

In this work, every wall-resolved and wall-modeled LES are produced using Argo DG solver. The purpose of this section is to present the physical modeling and the numerical methods that are used for the simulation of airfoil aerodynamics at low Mach numbers. Furthermore, this section presents how the wall models are implemented in the DG discretization framework and emphasize the constraints and challenges specific to this implementation. For a more generic description of Argo DG, refer to the works of Hillewaert [40], Carton de Wiart [15] and Schrooyen [81].

2.2.1 Navier-Stokes equations

In their conservation form and using Einstein notation with $i, j = 1, 2, 3$, the continuity, momentum and energy equations are given by

$$\frac{\partial(\rho)}{\partial t} + \frac{\partial(\rho u_i)}{\partial x_i} = 0 \tag{2.26}$$

$$\frac{\partial(\rho u_j)}{\partial t} + \frac{\partial(\rho u_j u_i)}{\partial x_i} = -\frac{\partial p}{\partial x_j} + \frac{\partial \tau_{ij}}{\partial x_i} + \rho f_j \tag{2.27}$$

$$\frac{\partial(\rho E)}{\partial t} + \frac{\partial(\rho E u_i)}{\partial x_i} = -\frac{\partial p u_i}{\partial x_i} + \frac{\partial \tau_{ij} u_j}{\partial x_i} + \rho f_i u_i - \frac{\partial q_i}{\partial x_i} \tag{2.28}$$

where u_i, f_i and q_i are the velocity, the external force and the heat flux in the direction x_i, ρ is the density, E is the total energy. The Navier-Stokes equations can be expressed in a more compact and generic form by defining a solution vector $\mathbf{W}$, a source term vector $\mathbf{S}$ and by splitting the convective $\mathbf{C}$ and diffusive $\mathbf{D}$ fluxes according to the following relations

$$\frac{\partial \mathbf{W}}{\partial t} + \frac{\partial\, \mathbf{C}}{\partial x_i} + \frac{\partial\, \mathbf{D}}{\partial x_i} + \mathbf{S} = 0 \tag{2.29}$$

$$\mathbf{W} = \begin{pmatrix} \rho \\ \rho u_j \\ \rho E \end{pmatrix} \mathbf{C} = \begin{pmatrix} \rho u_i \\ \rho u_i u_j + p\delta_{ij} \\ \rho u_i E + p u_i \end{pmatrix} \mathbf{D} = \begin{pmatrix} 0 \\ -\tau_{ij} \\ q_i - \tau_{ij} u_j \end{pmatrix} \mathbf{S} = \begin{pmatrix} 0 \\ -\rho f_j \\ -\rho f_i u_i \end{pmatrix}. \tag{2.30}$$

In this work, this system of equations is closed by assuming a perfect gas. Furthermore, a Newtonian fluid is considered, the bulk viscosity is neglected, and the viscous stress tensor is thus given by

$$\tau_{ij} = \mu \left(\left[\frac{\partial u_j}{\partial x_i} + \frac{\partial u_i}{\partial x_j} \right] - \frac{2}{3} \delta_{ij} \frac{\partial u_i}{\partial x_i} \right) \tag{2.31}$$

2.2.2 Spatial discretization: discontinuous Galerkin method

In this work, the discontinuous Galerkin method is used to discretize the Navier-Stokes equations. This method is a particular class of Galerkin finite element method (FEM). As in classical FEM, each variable $\tilde{w}_m$ of the solution vector $\mathbf{W} = [\rho\ \rho u_0\ \rho u_1\ \rho u_2\ \rho E] = [\tilde{w}_0 \dots \tilde{w}_4]$ is approximated by w_m that is a linear combination of N shape functions ϕ_i and their corresponding coefficients $W_{i,m}$ as

$$\tilde{w}_m \approx w_m = \sum_{i=1}^{N} W_{i,m}\phi_i \ , \tag{2.32}$$

where the ϕ_i form a basis of the test space Φ and N is the number of degrees of freedom (dof). In Argo DG, the shape functions are defined using Lagrange polynomials of degree p.

Unlike conventional FEM, in the discontinuous Galerkin method, these functions are not required to be continuous across any of the interfaces between the elements, as illustrated in Figure 2.10 for three elements e_1, e_2 and e_3. The solution on the entire computational domain can therefore be evaluated as the sum over each element e independently as

$$w_m = \sum_{e} \sum_{i=1}^{N_e} W_{i,m,e}\phi_{i,e} \ . \tag{2.33}$$

This specificity allows to divide the problem in a system of small finite element problems defined on each element. However, this increases also drastically the number of degrees of freedom as the ones contained on the interfaces are doubled.

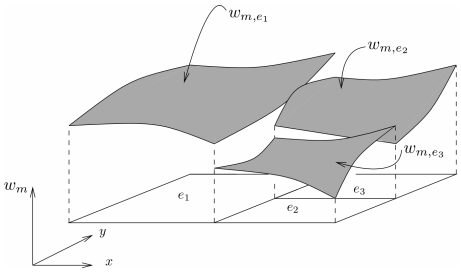


Figure 2.10: Sketch of the solution as interpolated in the discontinuous Galerkin method. Image taken from [40].

On each element, the Navier-Stokes equations Eq. (2.29) are solved using the Galerkin variational principle. The best approximated solution w to the solution state vector $\tilde{w}$ in the interpolation space Φ is found by requiring that the residual is orthogonal to all state vectors v of the same interpolation space Φ in a suitable inner product defined on the space Φ. The solution w is then found by demanding that the following expression is zero for all $v = [v_0 \dots v_4] \in \Phi$

$$\begin{aligned}\sum_e \int_e v_m \frac{\partial w_m}{\partial t} dV + \sum_e \int_e v_m \frac{\partial C_m^i}{\partial x^i} dV + \sum_e \int_e v_m \frac{\partial D_m^i}{\partial x^i} dV \\ + \sum_e \int_e v_m S_m dV = 0.\end{aligned} \tag{2.34}$$

The successive use of the integration by part and the divergence theorem on the convective and diffusive terms leads to the appearance of interface fluxes. Conversely to classic FEM, discontinuities are allowed between the elements and these fluxes do not cancel. To characterize them, an interface average operator $\{.\}$ and a jump operator $[[.]]$ are defined using $+$ and $-$ to indicate lower and upper values with respect to the face normal vector $\mathbf{n}$

$$\{a\} = \frac{(a^+ + a^-)}{2} \qquad \left[\left[a^i\right]\right] = a^- \mathbf{n}^{i-} + a^+ \mathbf{n}^{i+} \,. \tag{2.35}$$

Using also the Jacobian of the diffusive flux with respect to the solution gradients

$$D_m^i \approx D_{mn}^{il}(\tilde{w}) \frac{\partial \tilde{w}_n}{\partial x^l} \tag{2.36}$$

where D_{mn}^{il} is a fourth order tensor for variable m in direction i, the weak formulation in Eq. (2.34) becomes, $\forall v = [v_0 \dots v_4] \in \Phi$

$$\begin{aligned}&\underbrace{\sum_e \int_e v_m \frac{\partial w_m}{\partial t} dV}_{T} \underbrace{- \sum_e \int_e \frac{\partial v_m}{\partial x^i} C_m^i \, dV}_{C_{volume}} \underbrace{- \sum_e \int_e \frac{\partial v_m}{\partial x^i} D_m^i \, dV}_{D_{volume}} + \underbrace{\sum_e \int_e v_m S_m dV}_{S_{volume}} \\ &+ \underbrace{\sum_I \oint_I \left[[v_m]\right]^i n^i \, \mathcal{H}_m\left(w^-, w^+, \mathbf{n}\right) dS}_{C_{interface}} + \underbrace{\sum_I \oint_I \left[[v_m]\right]^i \left\{ D_{mn}^{il} \, \frac{\partial w_n}{\partial x^l} \right\} dS}_{D_{interface}} \\ &+ \underbrace{\sum_I \oint_I \left[[w_n]\right]^i \left\{ D_{nm}^{il} \frac{\partial v_m}{\partial x^l} \right\} dS}_{D_{transpose}} - \underbrace{\sum_I \sigma \oint_I \left[[v_m]\right]^i \left[[w_m]\right]^i dS}_{D_{penalty}} = 0 \,.\end{aligned} \tag{2.37}$$

The first four terms of this relation are common to the classic FE method. They represent, respectively, the temporal term T and the volume contributions to the convective C_{volume}, diffusive D_{volume} and source S_{volume} terms.

The four remaining terms are the interfaces fluxes that couple the elements. A partial integration performed per element results in interface contributions, $C_{interface}$ and $D_{interface}$, which essentially correspond to jumps in surface fluxes. Similarly to a finite volume method, the convective fluxes are evaluated using an approximate Riemann solver to stabilise the formulation. In this study, Roe's flux difference splitting is employed. $D_{penalty}$ and $D_{transpose}$ are used respectively to ensure the stability of the diffusive scheme and to provide a symmetric formulation according to the Symmetric Interior Penalty formulation [4]. This formulation generalizes a boundary penalty method to enforce weak Dirichlet boundary conditions at the interfaces. The penalty parameter σ must be chosen to be large enough to guarantee stability. Sharp bounds for the value of σ have been elaborated for all types of elements by Hillewaert [40]. These optimal values have been used in this study.

All integral terms of the variational formulation Eq. (2.37) are integrated with Gauss-Legendre quadrature rule and are solved in the reference elements using a mapping as presented in Figure 2.11.

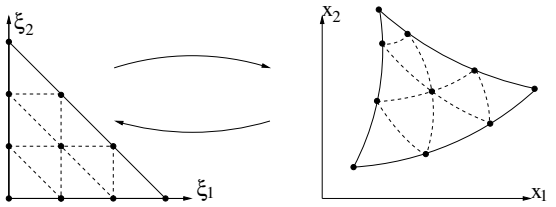


Figure 2.11: Mapping between the reference triangular element (left) and the element in the global frame (right). Image taken from [40].

The DG discretization provides $\mathcal{O}(h^{p+1})$ accuracy on unstructured meshes in the L_2 error norm and achieves low dispersion and dissipation errors. Despite the additional dof, the compact interpolation stencil provides computational density and locality, resulting in high serial and parallel efficiency.

2.2.3 Implicit Large-Eddy Simulation

In the classical LES approach, a low-pass spatial filter is applied to the Navier-Stokes equations. Considering k the wavenumber of the turbulent energy spectrum presented in Figure 2.12 and k_C the cut-off wavenumber, the solution is split into represented scales ($0 \leq k \leq k_C$) and subgrid scales ($k \geq k_C$). A subgrid-scale (SGS) model is then added to reproduce the effect of the subgrid scales on the larger scales.

As any practical discretization features considerable error near the highest wavenumbers, the represented scales are in fact split further in resolved ($0 \leq k \leq k_{RES}$) and under-resolved scales ($k_{RES} < k < k_C$) as presented in Figure 2.12.

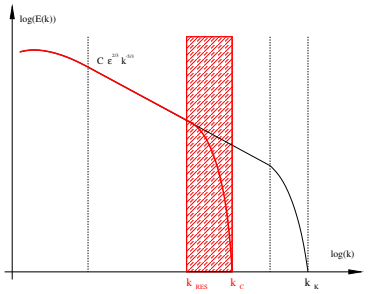


Figure 2.12: Energy spectrum of homogeneous isotropic turbulence at high Reynolds number. The thick black curve illustrates the implicit LES filtering with k_{RES} corresponding to the wavenumber value where the numerical error becomes important and k_C to the cut-off wavenumber where everything is filtered.

The spectral behavior of the DG methods concentrates the numerical dissipation more and more on the higher wavenumbers as the interpolation order increases [35], leaving larger parts of the spectrum intact. The numerical dissipation of high-order DG methods thus spectrally acts in a fashion similar to the explicit SGS approach. Therefore the implicit LES (ILES) approach seems a viable approach. As the shape of this implicit filter changes with the polynomial order, the range $k_{RES} - k_C$ shrinks as the order increases and a larger part of the spectrum is captured.

The ILES approach is often criticized, mainly due to its lack of physical background. As any numerical approximation generates numerical dissipation and dispersion errors, the interaction of numerical error with the modeling should however be taken into account for all LES models (*i.e.* implicit or explicit).

As one may expect that the performance of ILES will depend on the discretization and interpolation order, a considerable effort was spent in validating the approach used in this work on standard academic benchmarks such as the homogeneous isotropic turbulence and the channel flow cases [15, 17, 18], thereby demonstrating good accuracy for interpolation orders $p \geq 3$. The current work hence is a step forward in the validation of wall-resolved and wall-modeled ILES with a DG method.

2.2.4 Time discretization

Although multiple possibilities exist in Argo DG regarding the time discretization, in this work, all LES are performed using the second-order implicit time-stepping procedure based on the Backward Differentiation Formula (BDF2). For each time step, the global non-linear problem is solved using Newton-Raphson iterative algorithm. Each linear problem in the Newton-Raphson loop is then solved using an iterative approach; that is, in this work, unless

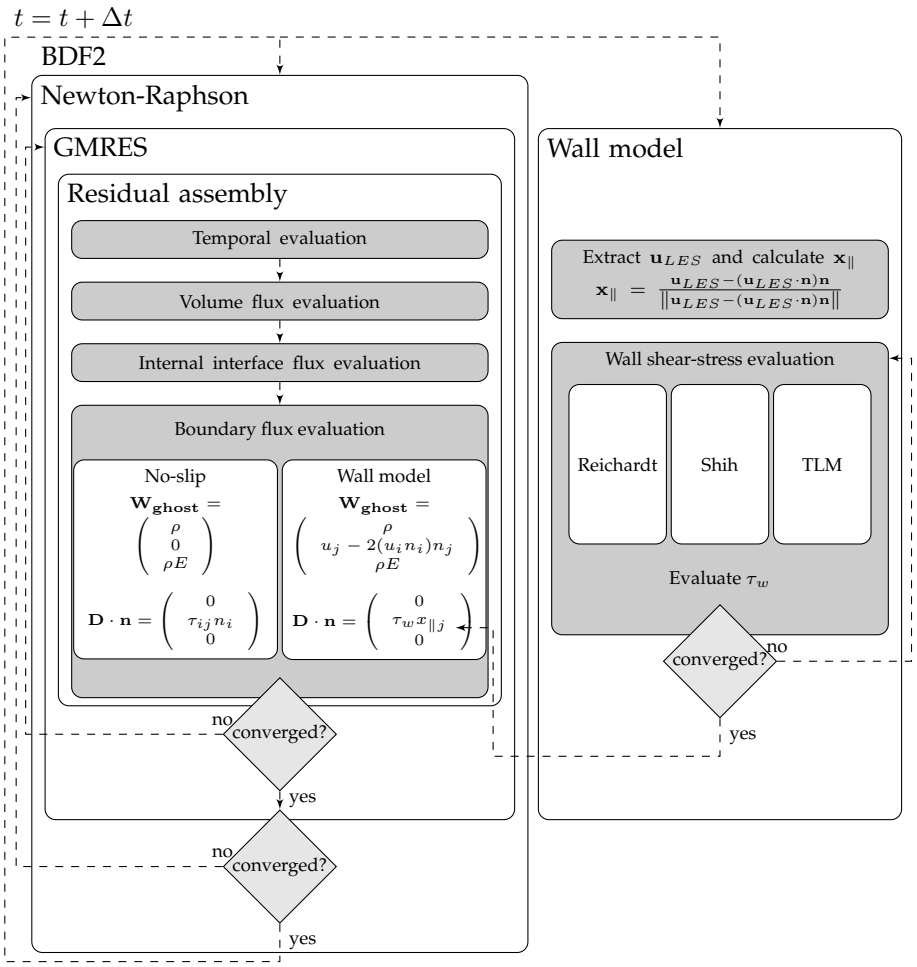


Figure 2.13: Global diagram of the different iteratives processes performed in this work for wall-resolved and wall-modeled LES.

explicitly specified, the matrix-free Generalized Minimum RESidual (GMRES) method, in combination with a block-Jacobi preconditioner. The global process is presented in Figure 2.13. The diagram further describes the imposition of the boundary conditions for classical no-slip walls as well as those equipped with a wall shear stress model approach. These steps are presented in details in the next section.

2.3 wmLES strategy

This section explains in details how the wall models have been implemented in Argo DG. It is divided in three steps: the specification of the boundary conditions, the implementation of the models, and the definition of a few chosen constraints in the usage of the wmLES within Argo DG.

2.3.1 Wall boundary conditions

In this work, all LES are performed considering fixed and adiabatic walls. For both convective and diffusive fluxes, the Dirichlet boundary conditions are applied weakly by imposing the conditions on virtual points referred to as ghost points. This provides a virtual exterior state to compute the interface fluxes of Eq. (2.37). To impose a Neumann boundary condition for the diffusive part, the required flux is imposed through $D_{interface}$ while ensuring no contribution from $D_{transpose}$ and $D_{penalty}$.

In wall-resolved LES, the boundary layer is sufficiently resolved to allow the imposition of the no-slip condition. As used in this work, the adiabatic wall boundary condition consists of the combination of Dirichlet conditions for velocity and Neumann conditions for density and energy. Specifically, for the Dirichlet BC, the density and energy components are left unchanged, providing a zero jump at the interface and the momentum components are set to zero. Likewise, for the Neumann BC, the energy component is set to zero, and the momentum components are left unchanged, as given by

$$\mathbf{W_{ghost}} = \begin{pmatrix} \rho \\ 0 \\ 0 \\ 0 \\ \rho E \end{pmatrix} \qquad \mathbf{D}\cdot\mathbf{n} = \begin{pmatrix} 0 \\ \tau_{i1}n_i \\ \tau_{i2}n_i \\ \tau_{i3}n_i \\ 0 \end{pmatrix}. \tag{2.38}$$

In wall-modeled LES, the boundary layer is too coarse for imposing the no-slip condition and a slip condition is used, thereby removing the Dirichlet conditions on the wall-tangent components of the velocity. The missing information is then provided by the Neumann conditions that impose the wall shear stress. Specifically, for the Dirichlet BC, the density and energy components are left unchanged, but the momentum components are manipulated in order to suppress the wall-normal component. Likewise, for the Neumann BC, the energy component is set to zero, and the tangential part of the momentum components is replaced by the wall model output as

$$\mathbf{W_{ghost}} = \begin{pmatrix} \rho \\ u_1 - 2(u_i n_i)n_1 \\ u_2 - 2(u_i n_i)n_2 \\ u_3 - 2(u_i n_i)n_3 \\ \rho E \end{pmatrix} \quad \mathbf{D}\cdot\mathbf{n} = \begin{pmatrix} 0 \\ \tau_w x_{\|1} + ((\tau_{ij}n_j)n_i)n_1 \\ \tau_w x_{\|2} + ((\tau_{ij}n_j)n_i)n_2 \\ \tau_w x_{\|3} + ((\tau_{ij}n_j)n_i)n_3 \\ 0 \end{pmatrix}. \tag{2.39}$$

where $\mathbf{n}$ is the normal to the wall surface and $\tau_{\mathbf{w}}$ is the imposed wall shear stress calculated by the wall model.

Although the fluxes are calculated at each GMRES iteration, the imposed wall shear stress is calculated only once per time step, as presented in Figure 2.13. The wall model procedure is divided in three main steps. At each time step and for each quadrature point, the velocity at the distance y_{wm} from the wall is extracted and its contributions parallel to the wall are calculated as

$$\mathbf{x}_{\parallel} = \frac{\mathbf{u}_{LES} - (\mathbf{u}_{LES} \cdot \mathbf{n})\mathbf{n}}{\|\mathbf{u}_{LES} - (\mathbf{u}_{LES} \cdot \mathbf{n})\mathbf{n}\|} \tag{2.40}$$

$$u_{\parallel} = \mathbf{u}_{LES} \cdot \mathbf{x}_{\parallel} \, , \tag{2.41}$$

where $\mathbf{x}_{\parallel}$ is the direction of the input velocity tangential component. Based on this velocity, the shear stress is calculated. This calculation depends on the chosen model, as it will be explained in Section 2.3.2. The provided wall shear stress τ_w is then projected in the global frame

$$\tau_{\mathbf{w}} = \tau_w . \mathbf{x}_{\parallel} \tag{2.42}$$

and imposed at the wall through the Neumann boundary condition.

Note that some terms in $(\mathbf{D} \cdot \mathbf{n})$ are grayed as they were not used to perform the wmLES presented in this work. These terms have been recently added as they avoid to over-constrain the problem by removing the condition on the wall normal stress, which is supposed to be zero in the original formulation. As the shear in the wall-normal direction is physically zero, the over-constrained version is still physically consistent and both formulations should converge to the same result. The two versions of the boundary condition have been tested on the channel flow and no difference was observed.

Note also that the contribution to the energy equation is neglected in this work as adiabatic and stationary walls are considered.

2.3.2 Implemented wall models

Different approaches can be used to compute the wall shear stress τ_w. In this work, six models have been implemented and tested that can be categorized in two groups. Firstly, four analytical approaches have been developed based upon the logarithmic law Eq. (2.11), the analytical boundary layer profiles of Reichardt Eq. (2.16) and Spalding Eq. (2.17) and the Generalized law-of-the-wall of Shih Eq. (2.22). Secondly, two simplified versions of the Two-Layer Model (Eq. (2.24) and Eq. (2.25)) have been evaluated (*i.e.* the one described in [10] and [30]). Following initial tests, only three have been retained. The integration of these models is presented in the following sections.

Analytical profiles : Reichardt and Shih laws-of-the-wall

Reichardt (Eq. (2.16)) and Shih (Eq. (2.22)) laws-of-the-wall can be expressed as $u^+ = f(y^+, p^+)$. A function

$$f(\tau) = u^+ - f(y^+, p^+) = 0 \tag{2.43}$$

is hence easily defined and solved using a Newton-Raphson algorithm as

$$\tau_{n+1} = \tau_n - \frac{f(\tau_n)}{f'(\tau_n)}. \tag{2.44}$$

The initial value τ_0 is taken as the shear calculated at the previous time step. This Newton-Raphson iterative procedure has been used for all wmLES performed in this work. Recently, another version of the Reichardt law has been implemented. That version uses a lookup table rather than the iterative process, as suggested in [55]. By multiplying the Reichardt law Eq. (2.16) by y^+ on both side, the following relation is found

$$\begin{aligned} \frac{uy}{\nu} &= u^+ y^+ \\ &= y^+ \left(\frac{1}{\kappa} \ln\left(1 + \kappa y^+\right) \right) \\ &+ y^+ \left(\left(C - \frac{1}{\kappa} ln\left(\kappa\right) \right) \left(1 - \exp\left(\frac{-y^+}{11} \right) - \frac{y^+}{11} \exp\left(\frac{-y^+}{3} \right) \right) \right). \end{aligned} \tag{2.45}$$

As shown in Figure 2.14, the expression u^+y^+ as a function of y^+ is practically linear. So only a few points need to be stored in a table to retrieve it accurately using a simple linear interpolation. Figure 2.14 also presents the derivative of

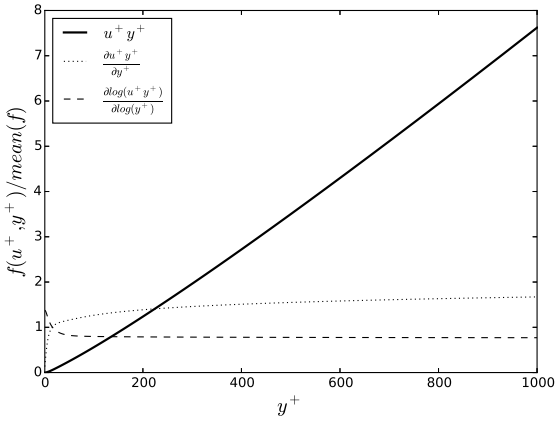


Figure 2.14: Reichardt's law profile when multiplied by y^+ in both sides and its derivatives, using or not the logarithmic form.

the expression u^+y^+ with respect to y^+ and the derivative of $(\ln(u^+y^+))$with respect to $(\ln y^+)$. As the second expression is closer to a constant value, it appears that the relation $(\ln(u^+y^+))$ as a function of $(\ln y^+)$ is even closer to a line. Therefore the data are stored as $\ln(u^+y^+)$ and, for a given set of inputs (u, y), the corresponding y^+ is found directly using the lookup table, providing the wall-shear stress as

$$\tau_w = \rho(y^+\nu/y)^2. \tag{2.46}$$

The Two-Layer Model

As described in Section 2.1.5, the Two-Layer Model from Balaras *et al.* [6] is often used in a simplified version. The most common simplification consists in neglecting the temporal and convective terms. Considering the problem in 2D, Eq. (2.24) and Eq. (2.25) become

$$\frac{\partial}{\partial y}\left((\nu + \nu_t(y))\frac{\partial u}{\partial y}(y)\right) = \frac{1}{\rho}\frac{\partial p}{\partial x}. \tag{2.47}$$

However, even with this simplification, the problem remains more complex to solve than the analytical laws as it requires the resolution of an ODE on an auxiliary grid. Two different implementation procedures have been evaluated. The first approach, inspired by the work of Bocquet *et al.* [10], integrates Eq. (2.47) and solves the obtained integrals by Gauss-Legendre quadrature. This method has been disregarded as it leads to quite complex sets of equations and to a high sensibility to the number of quadrature points. The second approach is based on finite difference and is presented in Figure 2.15. This approach is more adapted for the development of the wmLES methodology because it allows to modify rapidly the variant of the Two-Layer Model as well as the equations for ν_t.

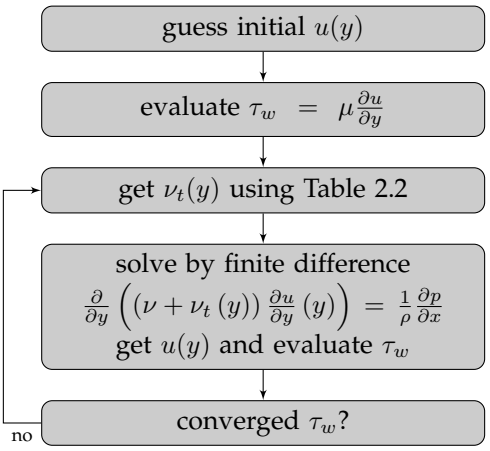


Figure 2.15: Iterative process for the resolution of the TLM using finite differences.

2.3.3 Specific design criteria

To preserve the large scalability and mesh flexibility of the DG method, the wmLES methodology should ideally satisfy a number of criteria. The first criterion consists in fixing an equivalent resolution in the streamwise and spanwise directions ($\Delta x = \Delta z$) as the code aims at being used in cases where there is no foreseen averaged flow direction.

The second criterion lies in keeping an order of accuracy in line with the wall-resolved LES experience that showed that fourth ($p = 3$) and fifth ($p = 4$) orders offered the best compromise between mesh flexibility, accuracy and computational cost for wall-resolved LES.

Although many wmLES strategies impose the equilibrium law in a space and a time averaged manner [83, 70, 83], the third criterion is to work locally and in an instantaneous manner. This comes from the aim to use the wmLES approach for practical flows, which may not have homogeneous directions, or may not be statistically steady. The averaging approach will hence not be used in general with the current methodology, but it is however evaluated in Section 4.2.6 in order to quantify its potential gains.

The fourth criterion is the most constraining one as it limits the position of the input location and links it directly to the mesh dimension. It aims at keeping parallel communication to a minimum in order to preserve scalability. The input location is therefore preferentially located in the wall-adjacent element or its direct neighbor, as the latter is already available as a ghost element. However, various studies show that the input location (y_{wm}) should be far enough from the wall to be resolved and recommend not to take the information in the wall-adjacent element. Park and Moin [67] also developed a wmLES approach for a highly scalable method dealing with unstructured meshes. To allow the input location to be far from the wall while keeping a minimum communication between the wall element and the input element, they choose to solve the wall model in a separated structured mesh. They however needed to add a preprocessing method to link each input location element to its corresponding wall-adjacent element. In order to avoid this complexity and as we can profit from the high-order scheme, this work tries to find a sufficiently accurate input data in the wall-adjacent element or its direct neighbors. The current implementation therefore allows, for each quadrature point, an input located everywhere between the wall and the first element top interface. The mesh needs a first extruded layer but the full flexibility can be kept in the rest of the domain.

CHAPTER 3

LOW REYNOLDS NUMBER AIRFOILS

This chapter presents wall-resolved Large-Eddy Simulations of two low Reynolds number airfoils: the S826 and the Eppler 387. Three complex flow phenomena are studied, namely the laminar separation bubble, the lift hysteresis and the stall cells. For the two airfoils, the wrLES results are compared to both experimental and numerical databases. These comparisons permit to highlight the complexity to provide "test-parameter-free" airfoil polars and the consequent difficulty in validating CFD approach based on experimental database. The chapter concludes by suggesting tracks to overcome these complexities by experimental and numerical collaborations. The work on the S826 has been published in "AIAA Conference Series"[33] and the work on the E387 in "Journal of Physics : Conference Series"[34].

3.1 Low Reynolds number flow phenomena

In the past few years, low Reynolds number airfoils ($Re = \frac{c\,u_\infty}{\nu} \leq 10^5$) have received a high interest from the booming unmanned and micro-aerial vehicle sector. In the wind sector, low Reynolds number aerodynamics is important for the small turbines, which have a diameter of a few meters and a production of a few kW. For the medium-size and the large wind turbines, which have a production of a hundred kW to several MW, the large extent of the blades results in high numbers at the blade tips. As the blade chord increases fast towards the center of rotation, the Reynolds number stays high through the blade, as presented in Figure 3.1. Low Reynolds number airfoil aerodynamics is therefore not directly relevant for the operation of medium-size and the large wind turbines. However, it is relevant for the development of the tools that are used for the design of the large wind turbines. These tools are indeed

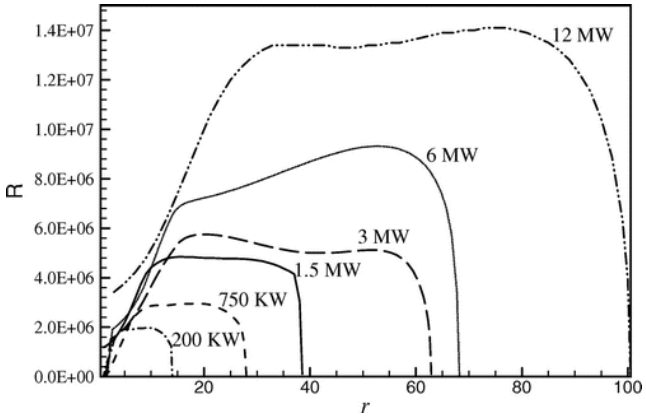


Figure 3.1: Reynolds number (R [-]) evolution along the wind-turbine blade radius (r [m]). Figure taken from Ge *et al.* [36].

developed and validated on small laboratory scaled wind turbines, which are subjected to low Reynolds number physics.

One representative example is the laboratory scaled wind turbine that was used in the recent series of blind tests, the Nowitech-Norcowe tests. These blind tests compared different wind turbine wake models to wind tunnel measurements and they demonstrated that some errors in the wake modeling could be attributed to the incorrect capture of the low Reynolds number airfoil polar [68]. Therefore, new experimental and numerical studies had to be launched to capture the low Reynolds number effects observed on the airfoil used in this experiment, namely the S826 airfoil [77, 75].

One critical flow phenomenon observed on low Reynolds number airfoils at some angles of attack is the laminar separation bubble (LSB), typically characterized by the successive laminar separation, transition and turbulent reattachment of the flow, as presented in Figure 3.2. The formation, the extent and the burst of this bubble are very sensitive to the environment and can lead to large changes in the airfoil performance. These types of performance changes are presented in Figure 3.3 that shows the electrical power measured in the field on a medium size 0.6 MW stall-regulated turbine. Bak *et al.* [5] attribute the sudden shifts in lift, observed around a wind speed of 17 m/s, to the bursting of large LSB.

This example is at a relatively high Reynolds number. The LSB are usually even more problematic for low Reynolds number because they are larger. Choudhry *et al.* [24] differentiate the long LSB, typical of low Reynolds number airfoils from the short LSB, which have a chord extent that is less than 1%. In both cases, the LSB is observable on the pressure coefficient (C_p) curve as a plateau of constant pressure, see Figure 3.4. However, the lengths of the plateau along the chord are different. Therefore, one can imagine that the

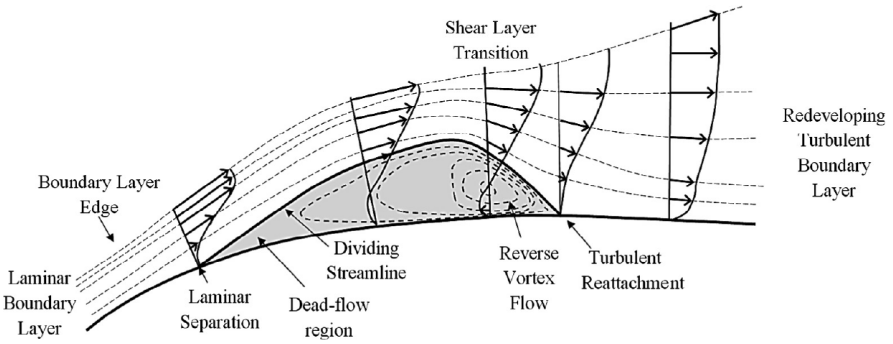


Figure 3.2: Schematic of the laminar separation bubble process. Figure from Horton [42] reproduced by Choudhry *et al.* [24].

burst of a long LSB would impact more drastically the performance of the airfoil.

As, at lower Reynolds number, the airfoil performance is more dependent on the flow environment, different wind tunnel measurements lead often to different polars. This problem is highlighted in Figure 3.5, which gives the lift coefficient measured on the E387 airfoil by four different wind tunnels. Globally, the four wind-tunnels capture the same trend. However, the measurements made in Delft [100] and in the NASA-Langley Low Turbulence Pressure Tunnel (LTPT) show a strong loss of performance around the angle of attack $AOA = 6°$, although the measurements made in Princeton [85] and

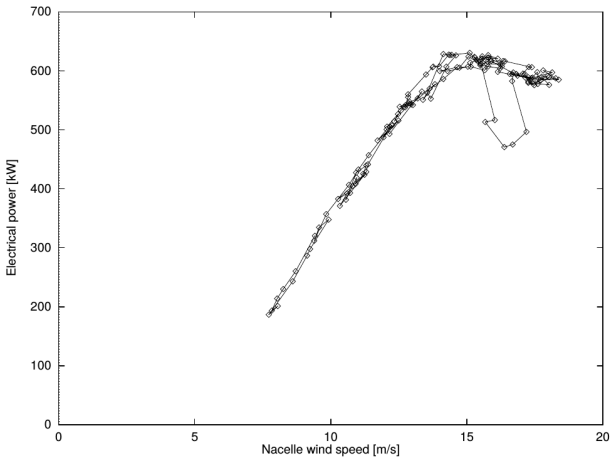


Figure 3.3: Electrical power measured on a 0.6 MW stall-regulated turbine for varying nacelle wind speed. Figure taken from Bak *et al.* [5].

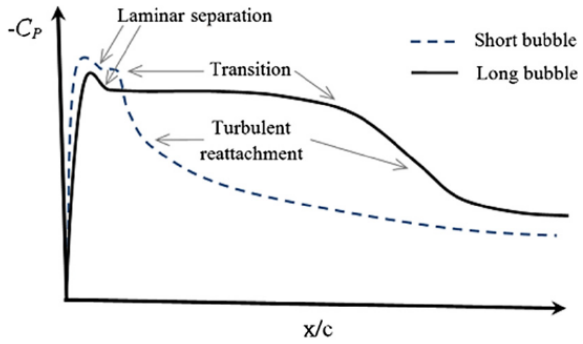


Figure 3.4: Typical pressure coefficients observed along the suction side on an airfoil subjected to a short and long LSB. Figure taken from Choudhry *et al.* [24].

in Stuttgart [3] do not present any jump in the lift curve. Furthermore, this negative jump in the lift curve is more local in Langley than in Delft as it is observed only for $5.5° \leq AOA \leq 6.5°$.

The sensitivity to the environment can even be observed in the same wind-tunnel. Figure 3.6 shows the lift measured in DTU Wind wind-tunnel for an increasing and decreasing angle of attack and for different inflow turbulence intensities. First, it appears that a slight increase of the turbulence intensity from $TI = 0.1\%$ to $TI = 0.8\%$ leads to much larger lift coefficients. Second, at the lowest inflow turbulence intensity, two lift coefficients are measured for $12° \leq AOA \leq 13°$. Therefore, depending on whether the angle of attack is increasing or decreasing, *i.e.* depending on the history of the flow, the lift for

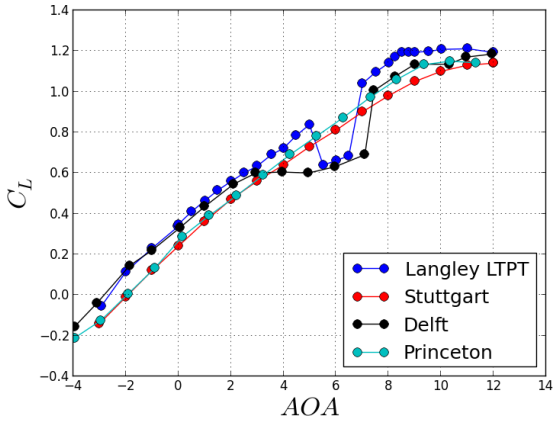


Figure 3.5: Wind-tunnel measurements of the lift coefficient (C_L $[-]$) as a function of the angle of attack (AOA $[°]$) of the E387 airfoil at $Re = 6 \times 10^4$ made in four different tunnels [59].

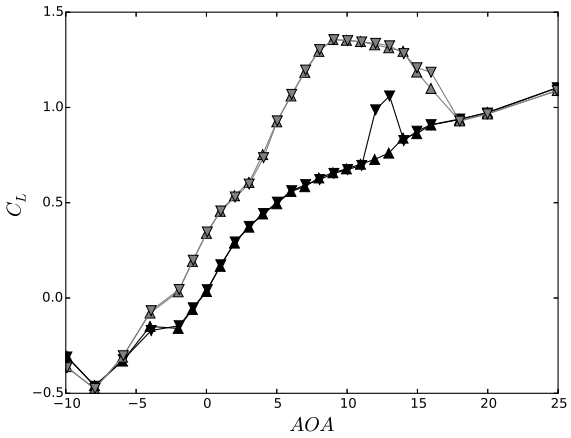


Figure 3.6: S826 airfoil at $Re = 4 \times 10^4$. Wind-tunnel measurements of the lift coefficient in regard to the angle of attack for an increasing (up triangles) and decreasing (down triangles) angle of attack and for two different inflow turbulence intensities: $TI = 0.1\%$ (black) and $TI = 0.8\%$ (gray). Data provided by H. Sarlak [75].

$12° \leq AOA \leq 13°$ will be $\simeq 0.7$ or $\simeq 1.0$. This hysteresis phenomenon results in a wider low performance region for increasing than for decreasing angles of attack.

The extreme sensitivity to the wind tunnel environment leads to uncertainty on the wind tunnel data. The use of CFD as virtual wind tunnel, where the geometry and the flow conditions are well controlled, is therefore a very attractive perspective. However, the CFD methods are usually validated by comparison to experiments. The study presented here tries to break this vicious circle by investigating the S826 and the E387 airfoils with wall-resolved LES and by comparing the results to both experimental and numerical results. For the two airfoils, the numerical results used for the comparison are performed through a collaboration with DTU Wind using well-established aerodynamic codes within the Wind-Energy sector, XFOIL, EllipSys2D and EllipSys3D. For the S826 airfoil, the present wrLES is compared to wrLES made by DTU Wind with EllipSys3D. For the E387, the wrLES is compared to state-of-the-art tools, *i.e.* panel and RANS made with XFOIL and EllipSys2D, respectively. Regarding the experimental databases, as the S826 airfoil is measured in DTU Wind, the collaboration permitted to re-analyze the raw data and to perform new tests with oil-flow visualization. For the E387 airfoil, the large database produced by McGhee *et al.* [59] has been used. The analyses of the S826 and E387 airfoils are presented in the two following sections.

3.2 S826 airfoil: wrLES-experimental cross-validation

As the experimental study of the S826 showed strong performance jumps between $Re = 4 \times 10^4$ and $Re = 1 \times 10^5$ as well as a hysteresis for angles around $12°$ [75], it is interesting to perform wrLES at these two Reynolds numbers and $AOA = 0°$ and $12°$. After a short description of the numerical setup, the results are compared to the experimental results as well as to wrLES performed by H. Sarlak from DTU Wind with EllipSys3D. The discussion is then pushed further by re-analyzing the experimental raw data and by performing new numerical and experimental studies on the sensitivity to the spanwise extent.

3.2.1 Numerical setup

Two different meshes are generated to correspond to the two Reynolds numbers. Both meshes are obtained by spanwise extrusion of a 2D unstructured O-type mesh composed mainly of triangles in the far-field combined to quadrangles in the boundary layer region, as presented in Figure 3.7. Spanwise periodicity is imposed at a spanwise distance corresponding to 10.5% of the chord. No turbulence has been introduced at the inlet and the flow conditions are chosen such that the freestream Mach number equals 0.15.

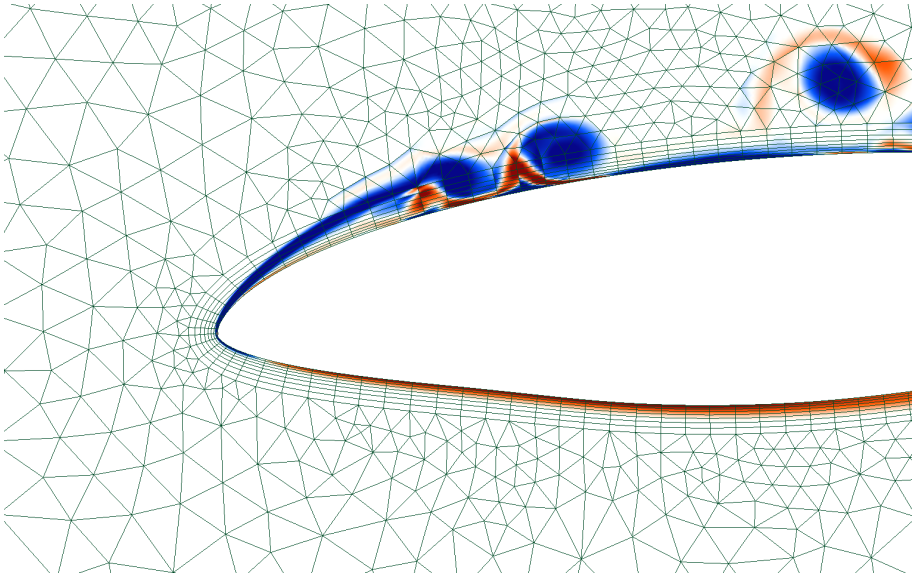


Figure 3.7: View of the 2D unstructured mesh and the instantaneous spanwise vorticity obtained at $AOA = 12°$ and $Re = 4 \times 10^4$ at some early time, thus the flow is not yet statistically established.

According to the estimate from Choi and Moin [23], wall-resolved LES needs non-dimensional grid spacings in the streamwise (x), wall-normal (y) and spanwise (z) directions of

$$\Delta x^+ \simeq 50 - 130 \qquad \Delta y^+ \simeq 1 \qquad \Delta z^+ \simeq 15 - 30. \tag{3.1}$$

This rule is however too restrictive for high-order methods in the wall normal direction [18], whereas the streamwise resolution is not appropriate for reattachment zones which demand a more isotropic mesh. The runs at the two Reynolds numbers are hence performed on meshes, designed to correspond to the following specifications in the turbulent region

$$\Delta x^+ \leq 20 \quad \Delta y^+ \leq 1.5 \quad \Delta z^+ \leq 20 \quad Re = 4 \times 10^4, \tag{3.2}$$

$$\Delta x^+ \leq 30 \quad \Delta y^+ \leq 2.0 \quad \Delta z^+ \leq 30 \quad Re = 1 \times 10^5. \tag{3.3}$$

To minimize the grid cost, the grid size has been rapidly increased from the airfoil-surface to the domain boundaries. However, the cell growth rate has been kept small and smooth in the zones of interest, as shown in Figure 3.7. Although the instantaneous contours of the spanwise vorticity shown on this figure are not truly a quantitative evaluation of the mesh resolution, their continuity seems to indicate that the mesh resolution is sufficient. Considering that elements with $p = 3$ have been used in the entire domain, a total of 2.5M degrees of freedom is found for the computations at $Re = 4 \times 10^4$ and 14.9M for the computations at $Re = 1 \times 10^5$.

3.2.2 wrLES at $Re = 4 \times 10^4$ for $AOA = 0°$ and $12°$

At Re of 4×10^4, two wrLES have been performed. The first one has an AOA of $0°$ and the second one an AOA of $12°$. Figure 3.8 presents a global view of the spanwise vorticity field obtained for both conditions, showing in both cases a laminar separation followed by a transition to turbulence. The two cases are however very different. Whereas at $AOA = 0°$, the laminar separation occurs at about 50% of the chord on the suction side and 35% on the pressure side, at $AOA = 12°$, the separation occurs very close to the leading edge on the suction side and no separation is observed on the pressure side. For an angle of $12°$, it seems that an LSB is present close to the leading edge.

Figure 3.9 compares the numerical results to the lift and drag coefficients measured at a Reynolds number of 4×10^4 for various levels of inflow turbulence intensity (ITI) [75]. The two numerical predictions are close at $AOA = 0°$, although relatively, the discrepancy is not negligible. At $AOA = 12°$, the lift coefficients are identical. Obtaining very similar wrLES values from two inherently different CFD methodologies and meshes provides confidence in the accuracy of the wrLES. A perfect correspondence with the experiment is although not achieved. Both CFD results are obtained without inflow turbulence and are expected to be closer to the low ITI experimental values. It is however not the case at $AOA = 12°$ where the LES results are much closer to the high ITI experiment.

Figure 3.10 compares the obtained pressure distributions to the numerical and experimental datasets. For $AOA = 0°$, the computational curves obtained with both codes coincide perfectly with the experiment at $ITI \leq 0.1\%$. For $AOA = 12°$, three experimental sets of datapoints are presented. At $ITI \leq 0.1\%$ hysteresis is observed, leading to two different distributions, whereas at $ITI \sim 0.8\%$ only one curve is found. The result at $ITI \leq 0.1\%$ for an increasing AOA is very different from the others. There is no pressure plateau and the performance is extremely low. In the two other measurements and in the two CFD results, there is a pressure plateau, revealing the presence of an LSB. Therefore, the jump in performance comes likely from the presence or the absence of the LSB. In the absence of LSB, the flow is completely separated and it induces a large performance loss.

Note that, in Figure 3.10, the minimum and maximum C_p measured during the experiment are provided in addition to the time-averaged C_p value. The time-averaged value is usually the only data provided, as it was in this case before the collaborative work. By indicating the range of C_p measured over the time, one can deduce the sensitivity of the measurements. It appears that the spread is considerable for $ITI \leq 0.1\%$ and decreasing angles of attack, reflecting an important fluctuation of the LSB size in time. The measurements at $AOA = 12°$ show as well that, as observed experimentally by Tan and Auld [93], an increase in inflow turbulence leads to earlier transition and reattachment, and therefore to a smaller LSB.

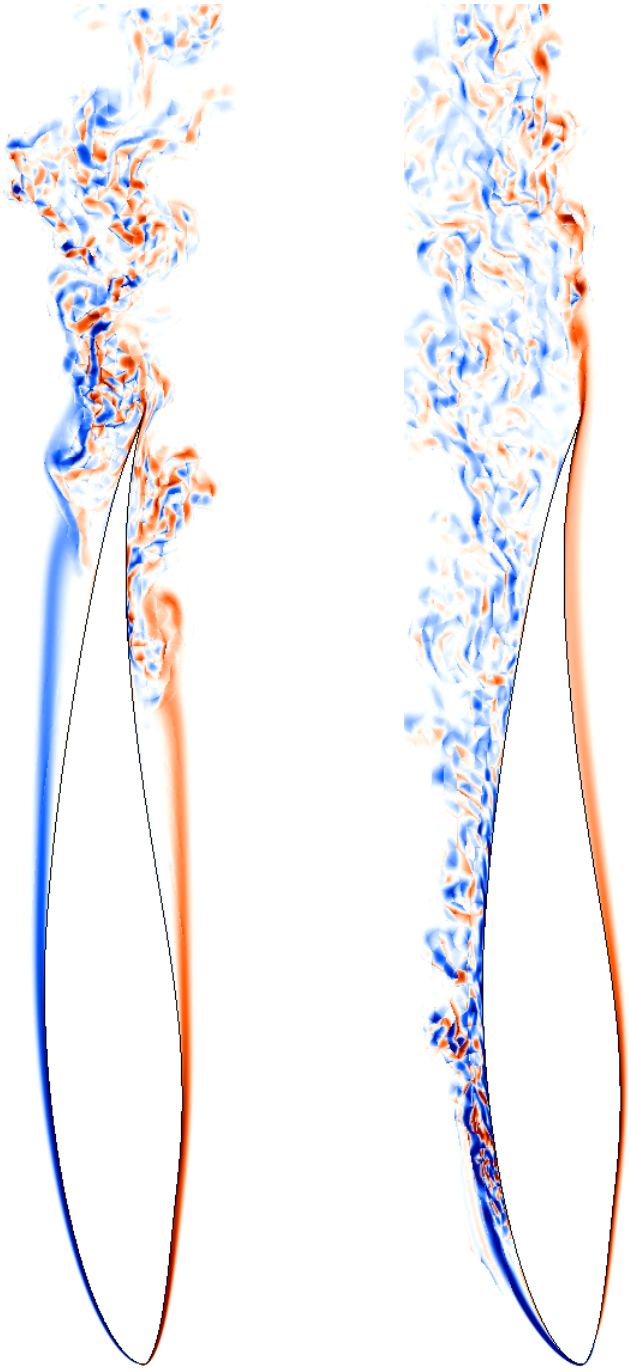


Figure 3.8: S826 airfoil at $Re = 4 \times 10^4$: separation region visualized by the spanwise vorticity in one plane at $AOA = 0^\circ$ (left) and $AOA = 12^\circ$ (right).

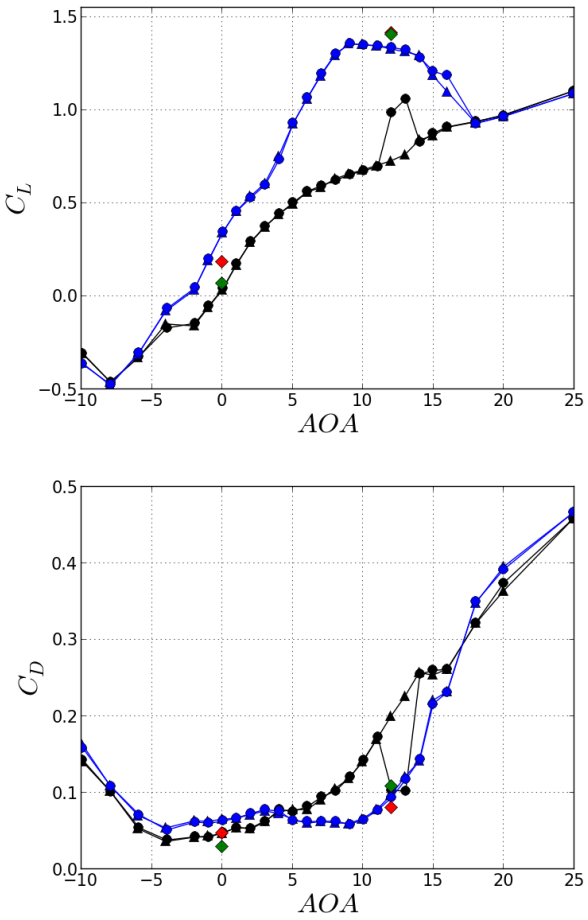


Figure 3.9: S826 airfoil at $Re = 4 \times 10^4$: lift and drag coefficient in regard to the angle of attack. The experimental data provided by H. Sarlak [75] are presented for an increasing (up triangles) and decreasing (circles) angle of attack and for two different inflow turbulence intensities: $ITI \leq 0.1\%$ (black) and $ITI \sim 0.8\%$ (blue). The wrLES results performed with the present DG method are highlighted using red squares, the ones performed with EllipSys3D are marked with green squares.

Further considering Figure 3.10 it seems that the LES results at $AOA = 0°$ are close to the experiment at low ITI and at $AOA = 12°$, they are not as similar to the high ITI experiment as thought previously on the basis of the aerodynamic performance. Indeed, the extent of the LSB (represented by the length of the pressure plateau on Figure 3.10) computed with LES is closer to the one of the LSB at $ITI \leq 0.1\%$. The persistent difference in the level of the pressure plateau could lie in the difference in ITI between the simulations ($ITI = 0\%$) and the measurement ($ITI \leq 0.1\%$). The shape of the LSB is

indeed strongly depending on the transition and reattachment locations and, as mentioned by McArthur [58], Schubauer and Skramstad [82] demonstrated that the transition over a flat plate is already affected by a turbulence level as low as 0.1%. As the natural transition is affected by this low change in TI, one can assume that it can also impact the separated flow transition process. The discussion on the reasons for the discrepancies between numerical and experimental results are pushed further in Section 3.2.4 and Section 3.2.5, after the analysis of the results for $Re = 1 \times 10^5$.

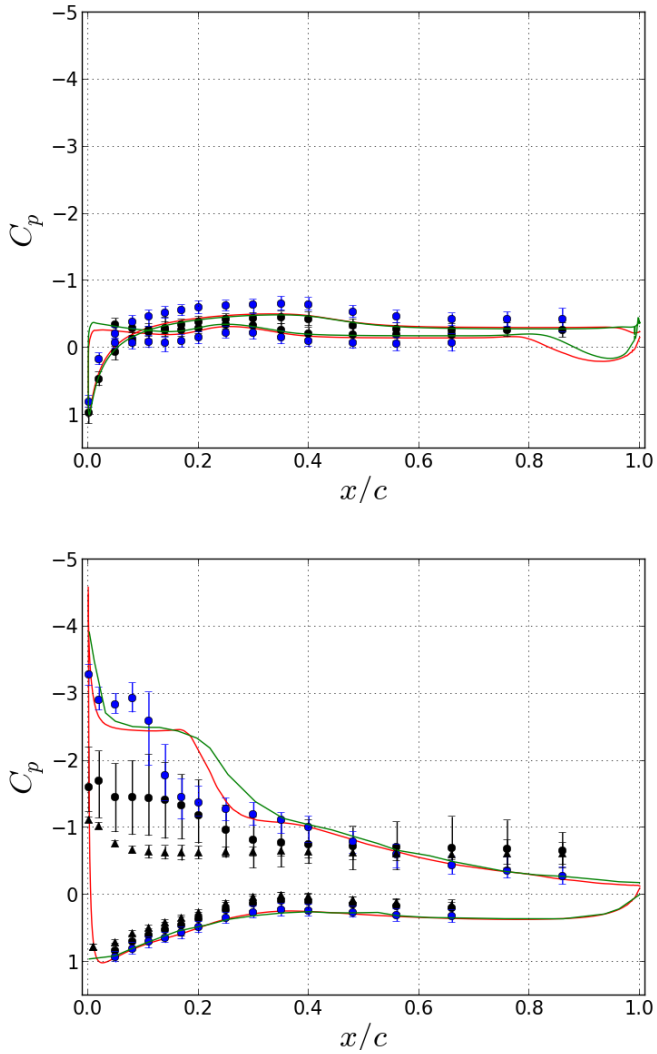


Figure 3.10: S826 airfoil at $Re = 4 \times 10^4$: chordwise pressure coefficients for $AOA = 0^\circ$ (top) and 12° (bottom). Error bars show min. and max. values obtained from the measurements with $ITI \leq 0.1\%$ (black) and $ITI \sim 0.8\%$ (blue). Markers are mean values for an angle of attack going up ($\triangle$) and down ($\circ$). The curves represent the wrLES results with the present DG method in red and EllipSys3D in green. Both wrLES consider an $ITI = 0.0\%$.

3.2.3 wrLES at $Re = 1 \times 10^5$ for $AOA = 0°$ and $12°$

As at $Re = 4 \times 10^4$, two wrLES are performed at $Re = 1 \times 10^5$, with respectively $AOA = 0°$ and $12°$. As seen in Figure 3.11, the flow features again an LSB. The transition seems however to occur earlier, coinciding with McGhee *et al.* [59] and Sarlak [75] observations that the transition point moves towards the leading edge as the Reynolds number increases. Therefore, the LSB is still present at $Re = 1 \times 10^5$ but it is considerably shortened.

Figure 3.12 presents the lift and drag coefficients measured at $Re = 1 \times 10^5$ and $ITI \leq 0.1$. Here only the case with the lowest inflow turbulence is presented as Sarlak *et al.* [75] observed that, at this Reynolds number, the results are not sensitive to the inflow turbulence. Again the LES results obtained with Argo and EllipSys3D are very similar.

The pressure coefficient distribution in Figure 3.13 shows again an excellent match between the Argo results and the experimental results at $AOA = 0°$. At this angle, EllipSys3D results are also very close to the experimental results. At $AOA = 12°$, the two codes provide similar results which are much closer to the experimental results than at $Re = 4 \times 10^4$.

There is however again a difference between the numerical and the experimental results, leading to simultaneously overestimate the lift and underestimate the drag at $AOA = 12°$. At the lower Reynolds number, the difference between the experimental and the numerical results had been attributed to the difference in ITI. Given the reduced sensitivity to ITI observed at this Reynolds number, other phenomena are expected here to explain this difference.

One explanation of this discrepancy could be a too coarse grid (likely in the spanwise direction) or an insufficient span width. To evaluate the numerical sensitivity to these aspects, Section 3.2.4 presents new wrLES for different span extents and spanwise refinements.

Another explanation could be the presence of a blockage effect in the experiments. However, using Barlow *et al.* correlations [7], the blockage effect is estimated as negligible [75] and of the same order of magnitude as in a similar study performed by Selig *et al.* [84]. These correlations are however not sufficient in the presence of large three-dimensional stalled regions. To evaluate the potential presence of 3D structures, more detailed experiments with oil flow visualizations are presented in Section 3.2.5.

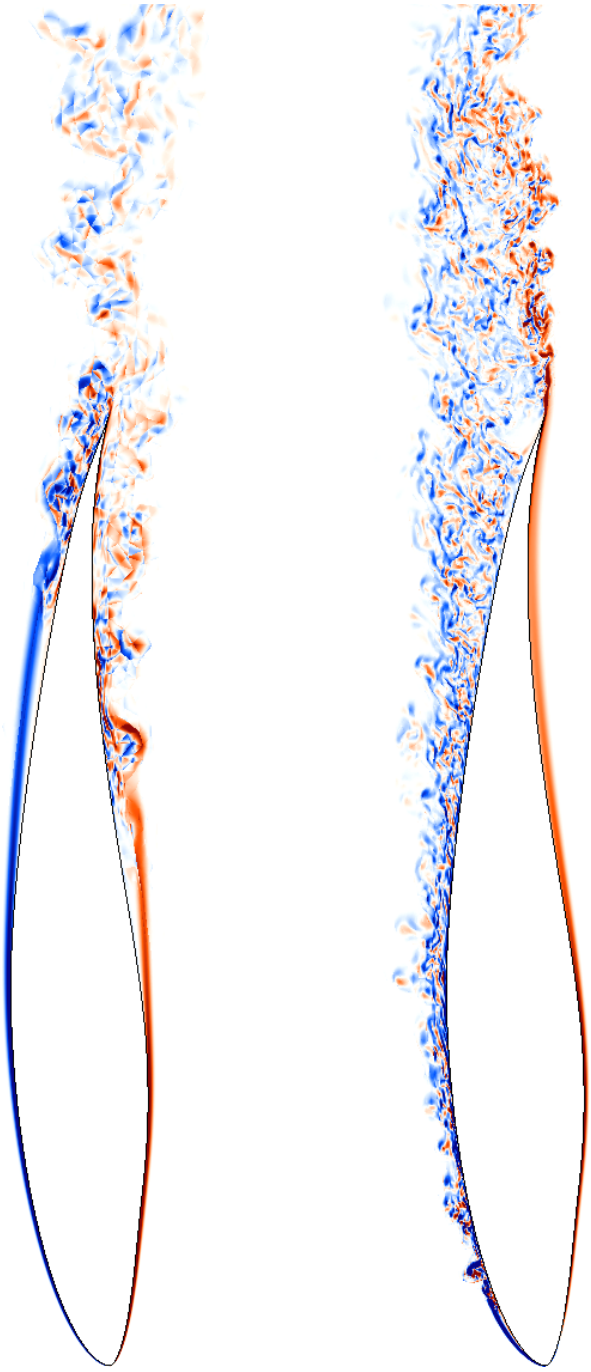


Figure 3.11: S826 airfoil at $Re = 1 \times 10^5$: separation region visualized by the spanwise vorticity in one plane at $AOA = 0^\circ$ (left) and $AOA = 12^\circ$ (right).

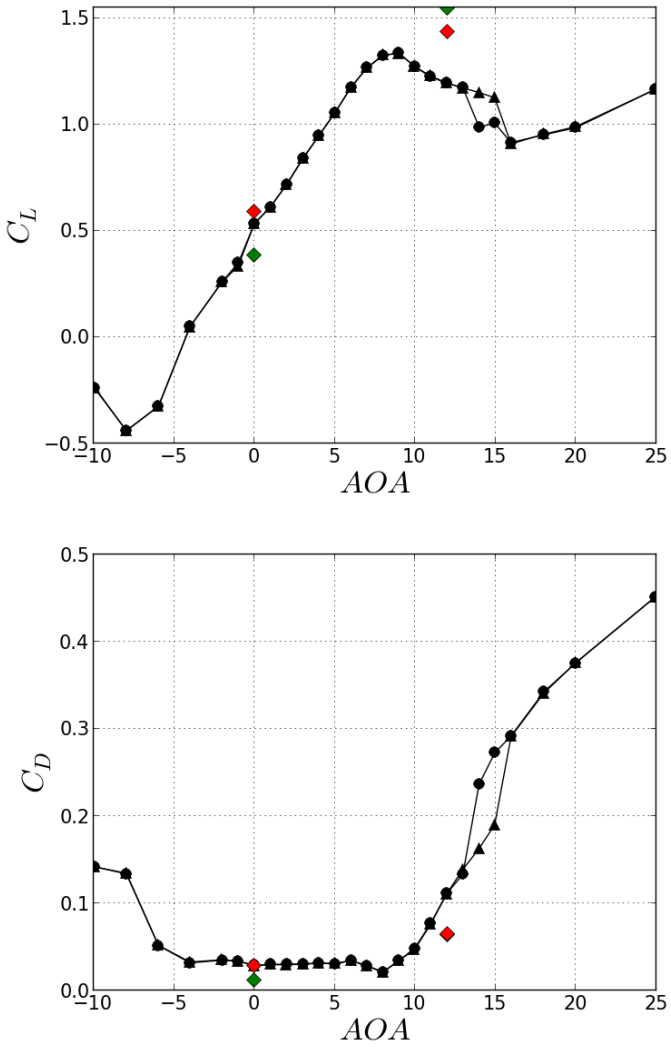


Figure 3.12: S826 airfoil at $Re = 1 \times 10^5$: lift and drag coefficient in regard to the angle of attack. The experimental data provided by H. Sarlak [75] are presented for an increasing (up triangles) and decreasing (circles) angle of attack with $ITI \leq 0.1\%$ (black curve). The wrLES results performed with the present DG method are highlighted using red squares, the ones performed with EllipSys3D are marked with green squares.

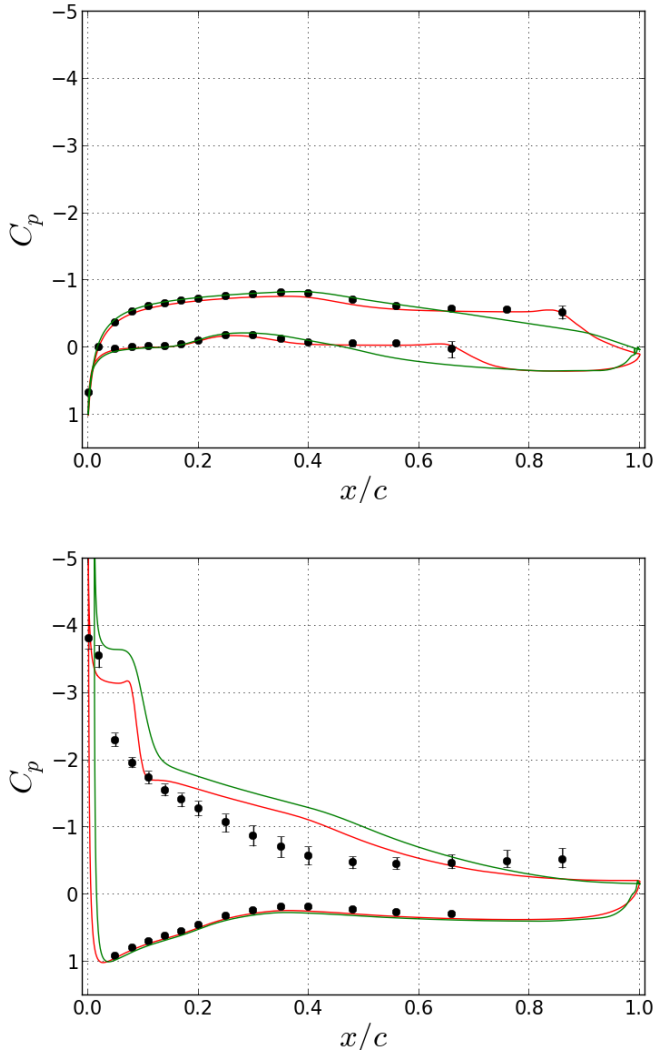


Figure 3.13: S826 airfoil at $Re = 1 \times 10^5$: chordwise pressure coefficients for $AOA = 0^\circ$ (top) and 12° (bottom). The black error bars and markers show min., mean and max. values obtained from the measurements ($ITI \leq 0.1\%$). The curves represent the wrLES results with the present DG method in red and with EllipSys3D in green.

3.2.4 Sensitivity analysis with respect to the span extent

Ideally, the wrLES should consider the full wind tunnel span extent as well as the lateral walls. However, this would require extensive computational resources. Therefore, the span extent over the chord (s/c) is limited to $s/c = 10.5\%$ and the refinement is kept as coarse as possible ($\Delta z^+ \leq 20$ at $Re = 4 \times 10^4$ and 30 at $Re = 1 \times 10^5$). To evaluate the sensitivity to the span extent and to its refinement, new wrLES are performed.

At $Re = 4 \times 10^4$ and $AOA = 12°$, three new computations are performed. The spanwise extent is doubled $s/c = 21.0\%$ and quadrupled $s/c = 42.0\%$ while keeping a similar refinement ($\Delta z^+ \leq 20$) and the spanwise refinement is doubled ($\Delta z^+ \leq 10$) while keeping the original span extent ($s/c = 10.5\%$). In all cases, the difference between the C_p curves is almost not distinguishable, as presented in Figure 3.14. This indicates that the initial span and mesh refinement were sufficient.

At $Re = 1 \times 10^5$, the mesh is coarsened in order to double the span extent while keeping the computational time acceptable. This leads to $\Delta z^+ \leq 60$. This Δz^+ is too large in comparison to wrLES grid requirements. Furthermore, the change in both mesh refinement and span length potentially precludes a clear conclusion. However, Figure 3.15, which compares the C_p curves for the two cases, indicates that these changes have a minor impact on the simulation results. Still for $Re = 1 \times 10^5$, Figure 3.16 presents the time-averaged streamwise friction fields on the suction side of the airfoil for the two span extents and for the two angles of attack. Again, the results for the two cases seem similar.

Note that, at $AOA = 12°$, some streaks are observed in the time-averaged shear. These streaks are due to the slight under resolution in the spanwise direction which induces small discontinuities between the elements. The small discontinuities, which are allowed by the DG method, are quite visible here as the plotted quantity involves a derivative of the solution. Physical streaks were clearly observed during the validation of the wrLES method in a channel flow for spanwise resolution $\Delta z^+ \simeq 30$, see [15]. They are thus likely also present here in the case for $\Delta z^+ \simeq 30$, but the near wall data were not processed at the time to illustrate them, and they are no longer available.

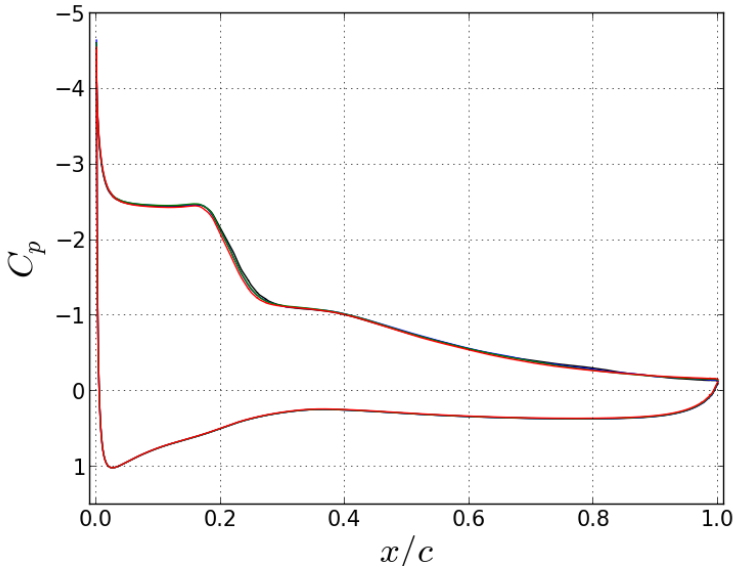


Figure 3.14: S826 airfoil at $Re = 4 \times 10^4$ and $AOA = 12°$: chordwise pressure coefficients obtained with the present wrLES for different span lengths and span refinements. The baseline ($s/c = 10.5\%$ and $\Delta z^+ \leq 20$) is given as a solid green line. The larger span extents (21.0% and 42.0% with $\Delta z^+ \leq 20$) as solid black and red lines. The refined case ($s/c = 10.5\%$ and $\Delta z^+ \leq 10$) as a solid blue line.

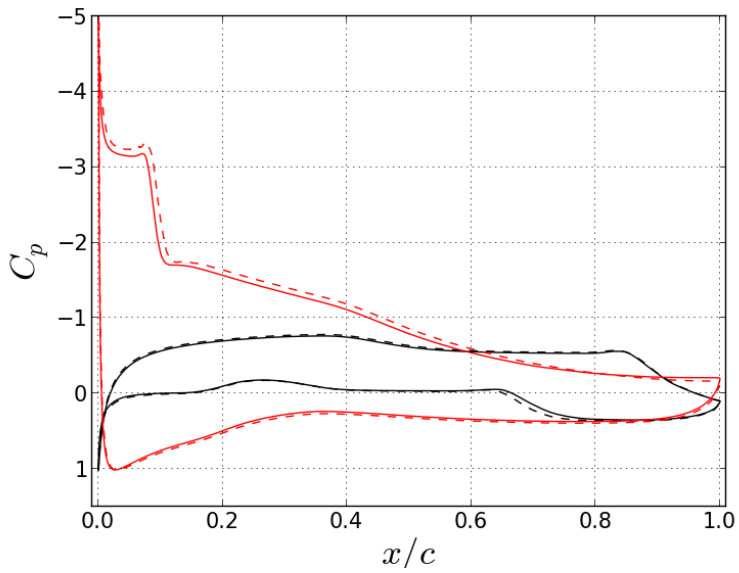


Figure 3.15: S826 airfoil at $Re = 1 \times 10^5$: chordwise pressure coefficients obtained with the present wrLES for $AOA = 0°$ (black) and $AOA = 12°$ (red). Comparison of different span extents relative to the chord: $s/c = 10.5\%$ (solid lines) and 21.0% (dashed lines).

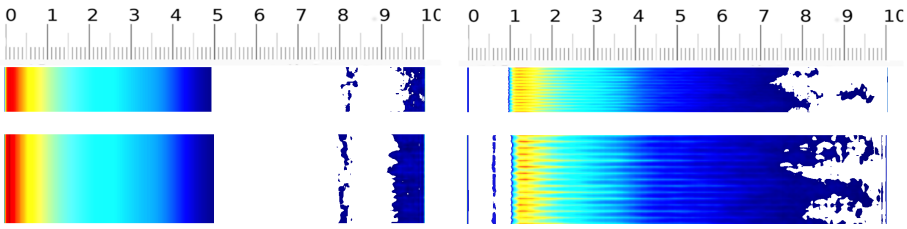


Figure 3.16: S826 airfoil at $Re = 1 \times 10^5$: separation region visualized on the suction side by stream-aligned positive component of the friction. WrLES results presented at $AOA = 0°$ (left) and $12°$(right). Comparison of different span extents relative to the chord: $s/c = 10.5\%$ (top) and 21.0% (bottom). The increase in span extent is coupled with a coarsening of the spanwise mesh: $\Delta z^+ \simeq 30$ (top) and $\Delta z^+ \simeq 60$ (bottom).

3.2.5 Oil flow visualization

To evaluate the potential presence of large 3D structures and interactions with the walls, oil flow visualizations are performed.

At $Re = 4 \times 10^4$, Figure 3.17 presents the results obtained for $AOA = 0°$ and $AOA = 12°$. It appears that the structures have a small spanwise extent, confirming the hypothesis that the span extent used in CFD is sufficient. Note on this figure that some masking tape is used to cover two screws and, at $AOA = 0°$, also to cover the pressure taps. The masking tape on the screws was already there during the previous lift and drag measurements made by H. Sarlak [75] but, obviously, no tape was masking the pressure taps then. To evaluate its impact, oil flow visualizations have been performed with and without masking tape on the pressure taps. However, no significant impact on the observed flow structures is observed.

Figure 3.18 compares the suction side of the airfoil for three angles of attack. The white regions indicate the zones of low shear and therefore, the separated regions. It appears that the three cases present an LSB that shortens and moves to the leading edge as the angle of attack increases.

At $Re = 1 \times 10^5$ and $AOA = 12°$, very large spanwise structures are observed as shown in Figure 3.19. This figure compares the full span fields obtained at $AOA = 12°$ for the two Reynolds numbers that have been analyzed with CFD ($Re = 4 \times 10^4$ and $Re = 1 \times 10^5$) as well as for a higher Reynolds number of 1.6×10^5. This figure confirms that at $Re = 4 \times 10^4$ the flow is nearly 2D. There are only two small corner vortices observed on the left and right connections with the lateral walls. At $Re = 1 \times 10^5$, the corner vortices are much larger, of about one chord and two large mushrooms structures, called stall cells, are observed along the span. As these structures are symmetric relatively to the screw holes, one could think that the screws create these structures. However, a further study with filled screw holes invalidates this hypothesis [76]. The result at $Re = 1.6 \times 10^5$ is given as it provides a better visualization of the corner vortices and stall cells.

These stall cells have been already observed [13, 74] and are problematic since, as presented by Gregory *et al.* [37], the pressure taps may not lie in a region of two-dimensional flow and may jump from pre to post-stall conditions. This is the case for the pressure taps in this experiment so it is obvious that the wrLES can not match the experiment for $Re = 1 \times 10^5$ and $AOA = 12°$.

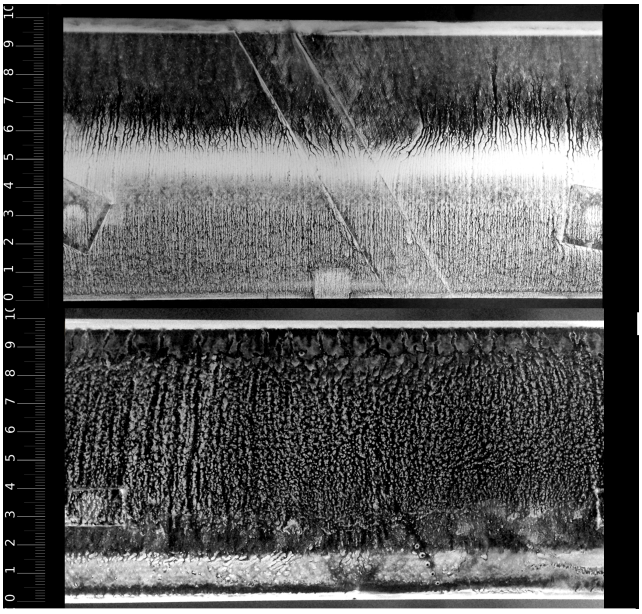


Figure 3.17: S826 airfoil at $Re = 4 \times 10^4$: oil flow visualizations on the suction side of the airfoil for two angles of attack: $AOA = 0^\circ$ (top) and $AOA = 12^\circ$ (bottom) ($ITI \leq 0.1\%$). Rulers indicate the chordwise position from 0, the leading edge, to 10, the trailing edge.

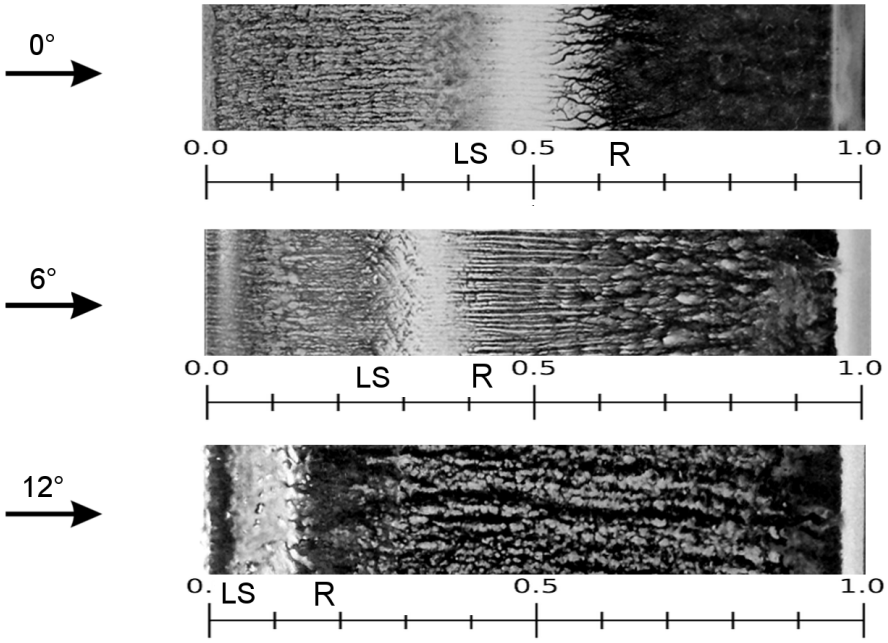
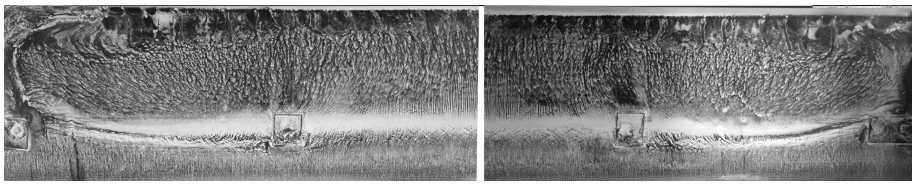
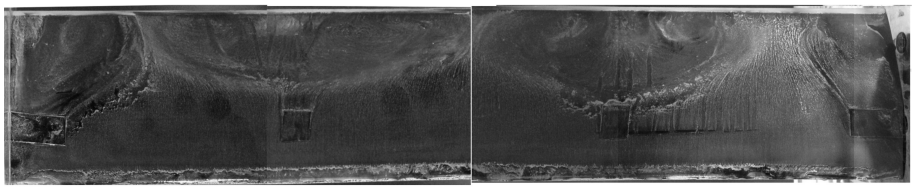


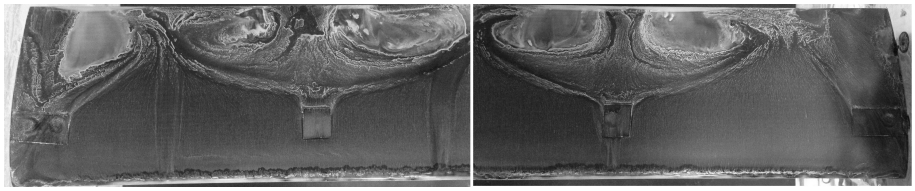
Figure 3.18: S826 airfoil at $Re = 4 \times 10^4$: comparison of the Laminar Separation (LS) and Reattachment (R) positions for different angles of attack ($AOA = 0$, 6 and 12^o). Top view on a mid-span section of the suction side.



(a) $Re = 4 \times 10^4$



(b) $Re = 1 \times 10^5$



(c) $Re = 1.6 \times 10^5$

Figure 3.19: S826 airfoil at $AOA = 12^o$ for three different Reynolds numbers. Flow visualization on the suction side with flow going from bottom to top. Two pictures joined to obtain a visualization of the full span.

3.3 E387 airfoil: comparison to state-of-the-art tools

Contrarily to the analysis of the S826 airfoil for which the wrLES results are compared to other wrLES, here the focus is on comparing the wrLES to well established numerical tools that are used in the wind industry. These tools are referred to, in this work, as state-of-the-art tools. The E387 airfoil is chosen as it has been tested in multiple wind tunnels and has well-documented databases. Although, Figure 3.5 shows slight differences in its lift measurement made by four different wind tunnels, this airfoil is considered as one of the best test case for low Reynolds number airfoil flows. The main reason for this is probably the extensive experimental campaign performed by McGhee *et al.* [59] in the NASA Low Turbulence Pressure Tunnel; providing force coefficient, chordwise pressure distribution and oil flow visualization for increasing and decreasing angles of attack, varying Reynolds numbers and inflow turbulence intensities. As the S826, the E387 is well representative of the low Reynolds flow complexities as it presents a lift hysteresis and a laminar separation bubble.

After a short description of the numerical setup, two wrLES are performed at $Re = 6 \times 10^4$ for $AOA = 4°$ and $8°$ and compared to the state-of-the-art tools. To investigate the possibility to capture the hysteresis, one additional wrLES is performed at $AOA = 6°$ and is compared to a DNS.

3.3.1 Numerical setup

The mesh created for the E387 airfoil follows the same process as the one described in Section 3.2.1 with a span extent of $\simeq 10\%$ of the chord. The mesh, shown in Figure 3.20 leads to computations of 2.7M dof with $\Delta y^+ \leq 1.5$ and $\Delta x^+ = \Delta z^+ \leq 20$.

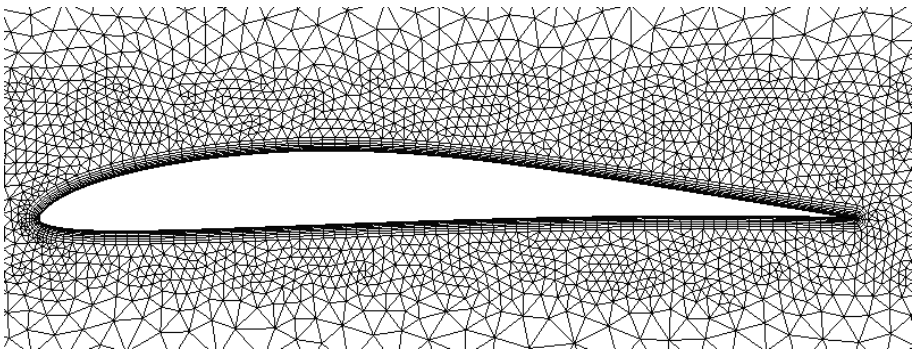


Figure 3.20: View of the 2D unstructured mesh used for the E387 airfoil wrLES.

The state-of-the-art tools are a panel method and a (U)RANS, both performed by N. Sørensen from DTU Wind. The panel method computations are per-

formed with XFOIL version 6.97 (with added boundary layer modeling). The default settings are used except for the parameter N_{crit} of the e^N transition model, parameter which mimics the impact of the environment turbulence on the transition and which is taken as close as possible to the wind tunnel turbulence level. Note that, although the e^N transition model is based on a linear theory, it is successful in the prediction of the transition location for boundary layers under pressure gradients. It is, therefore, widely used. The RANS computations are realized using the DTU in-house incompressible finite volume flow solver EllipSys2D [61, 62, 89] with the e^N transition model and the same parameter N_{crit} as for XFOIL. Although the wind tunnel turbulence level requests a $N_{crit} = 7$, $N_{crit} = 9$ is also tested to evaluate an eventual sensitivity to the turbulence intensity.

3.3.2 wrLES at $Re = 6 \times 10^4$ for $AOA = 4°$ and $8°$

The wrLES results are compared to the experimental data obtained by McGhee *et al.* [59] as well as to the above-mentioned XFOIL and RANS studies. For the lift and drag curves, shown in Figure 3.21, the computations are also compared to experiments from Delft [100], Princeton [85] and Stuttgart [3]. Please note that, as the Stuttgart original data are not available, summarized data in McGhee *et al.* [59] are used.

As XFOIL and URANS are much cheaper than LES, the full range of angles of attack are provided. To evaluate the impact of the turbulence intensity XFOIL and URANS have been run at two different turbulence levels, with $N_{crit} = 7$ corresponding to $TI = 0.16\%$ as observed experimentally and with $N_{crit} = 9$ corresponding to $TI = 0.07\%$, i.e. almost no inflow turbulence as considered for the LES simulations. The TI effect cannot be evaluated with the LES approach as the resolution of the turbulence from the domain inlet requires a too large computational resource. Both XFOIL and URANS clearly show the impact of the TI for $AOA = 4°$, a case for which the comparison of the codes will therefore be complex. The three computational approaches provide lift coefficients very similar to those of McGhee *et al.* [59] but XFOIL and LES seem to better capture the drag, URANS overestimating it.

The experiment shows in both cases a laminar separation followed by a transition in the shear layer and a reattachment, *i.e.* an LSB. Furthermore, it shows that the increase in angle of attack moves the reattachment point upstream, while displacing only slightly the separation point, thereby reducing the extent of the LSB [59]. Figure 3.22 presents the instantaneous friction and velocity fields obtained with LES. In both cases, the airfoil friction field shows a smooth 2D-like separation region (black area) that indicates the laminar separation. The flow then reattaches (white areas), indicating the turbulent reattachment and the LSB. Furthermore, the LSB starts closer to the leading edge and is shorter for the higher AOA. Therefore, the computations can be seen to reproduce the behavior observed experimentally.

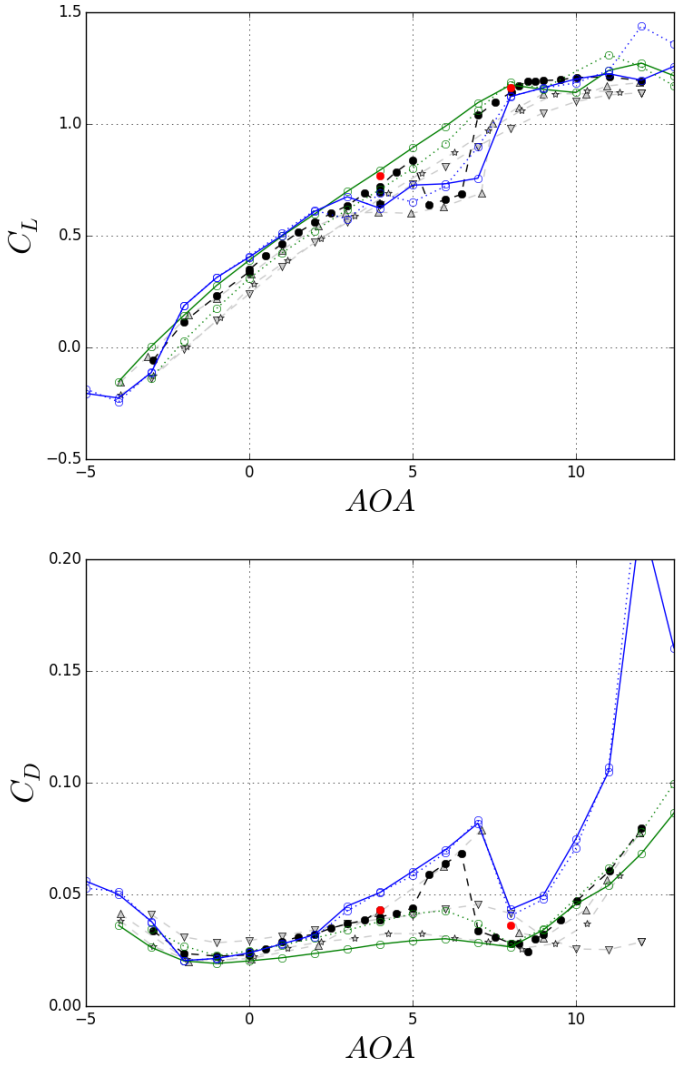


Figure 3.21: E387 at $Re = 6 \times 10^4$: comparison of the experimental and computational lift and drag coefficients. The computational results are in color: XFOIL (solid for $N_{crit} = 7$ and dashed for $N_{crit} = 9$ green), URANS (solid for $N_{crit} = 7$ and dashed for $N_{crit} = 9$ blue) and ILES (red). The experimental results are in grayscale with markers: LTPT (black circles), Delft (up triangles), Princeton (stars), and Stuttgart (down triangles).

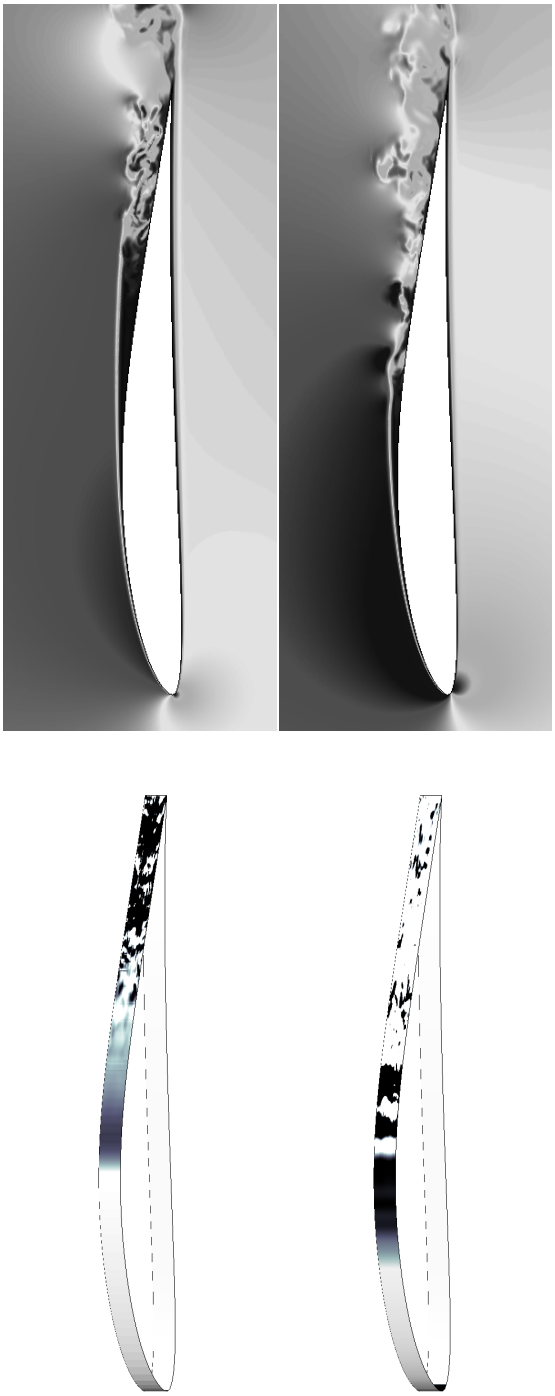


Figure 3.22: E387 LES separation: instantaneous x-aligned negative component of the friction (left, from black, fully detached to white, attached flow) and instantaneous velocity norm $\|u\|$ in one plane (right, dark corresponds to high values) at $AOA = 4^\circ$ (top) and $AOA = 8^\circ$ (bottom).

To determine the LSB and reattachment locations precisely, averaged chordwise pressure and skin friction distributions are presented in Figures 3.23 and 3.24. The LES results have been averaged over three flow passage times as well as along the span. At $AOA = 4°$, the two different flow configurations observed in the experiment are presented with a lower performance at $TI = 0.20\%$ than at $TI = 0.16\%$. The URANS results are close to the lower performance case ($TI = 0.20\%$) and this even when changing the N_{crit} of the transition model. The LES results are very well matching the higher performance case. This was expected as it is the case with the lower TI. XFOIL results are overestimating the performance, even compared to the experiment with the highest performance ($TI = 0.16\%$). Unlike the URANS results, an effect of the N_{crit} parameter is observed on the XFOIL results. At $AOA = 8°$, no turbulence effect is observed anymore and the present wrLES results are the closest to the experiment.

On the pressure curve, the LSB is identified by the pressure plateau. On the friction curve, the sign changes are used to locate the flow separation and reattachment points listed in Table 3.1. On this table, the separation and reattachment locations measured at a slightly higher Reynolds number are also given for comparison as there are almost no Reynolds number effect observed experimentally regarding separation and reattachment locations [59].

	Re	TI	$AOA = 4°$		$AOA = 8°$	
			S	R	S	R
XFOIL	6×10^4	0.16%	0.40	0.78	0.27	0.42
		0.07%	0.36	0.95	0.16	0.48
URANS	6×10^4	$0.07\% - 0.16\%$	0.34	0.66	0.11	0.36
LES	6×10^4	0.00%	0.37	0.69	0.21	0.43
exp.	1×10^5	0.16%	0.35	0.73	0.29	0.47

Table 3.1: Comparison of the computational and experimental separation and reattachment locations at $AOA = 4$ and $8°$ for different inflow turbulence intensities.

From these results, it seems that the difference between the computational results comes from a better capture of the LSB by the wrLES. However, due to the high sensitivity of the experiments and reference models to the TI, no strong conclusion can be taken regarding the small mismatch on the pressure distribution of the state-of-the-art tools.

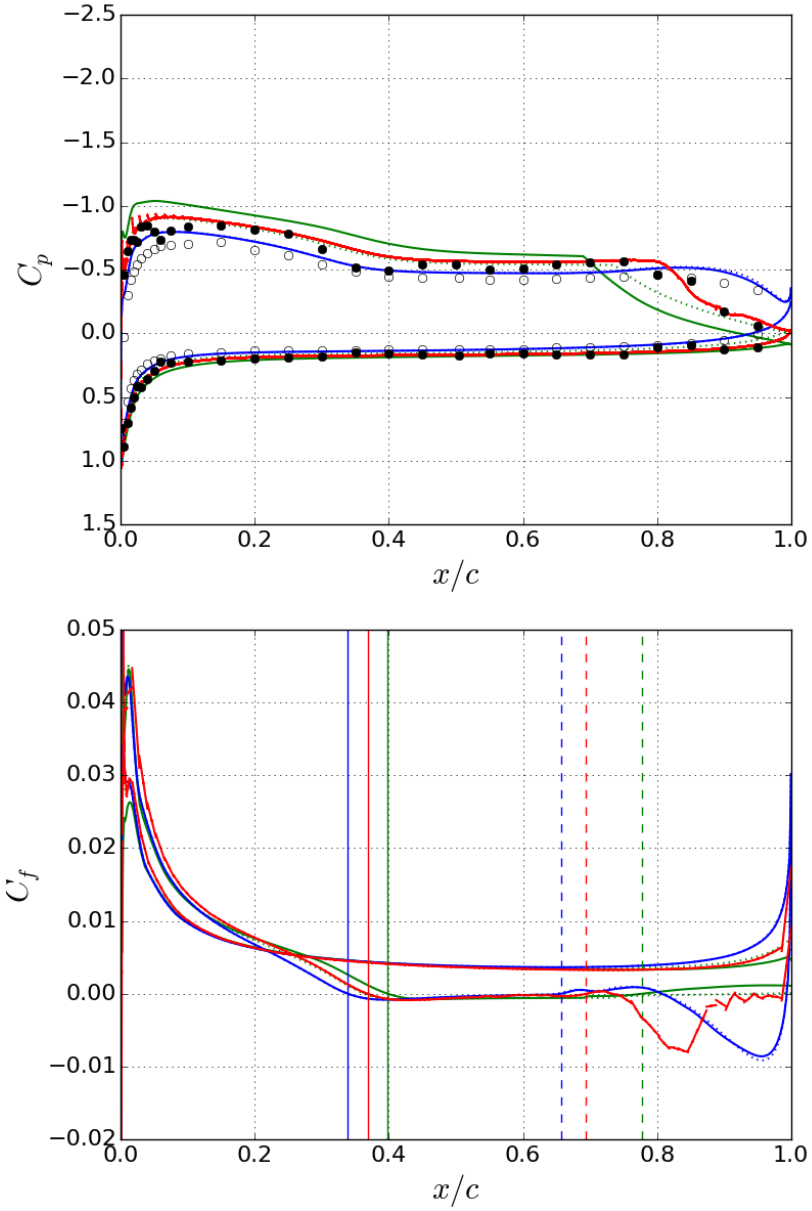


Figure 3.23: E387 airfoil at $Re = 6 \times 10^4$ and $AOA = 4°$: comparison of the chordwise pressure coefficient (top) and friction coefficient (bottom) obtained with XFOIL (solid $N_{crit} = 7$ and dotted $N_{crit} = 9$ green curves), URANS (solid $N_{crit} = 7$ and dotted $N_{crit} = 9$ blue curves) and the present wr-LES (red curves) to the experimental results (black $TI = 0.16\%$ and white $TI = 0.20\%$ circles) from [59]. Vertical solid and dashed lines present respectively the separation and reattachment locations.

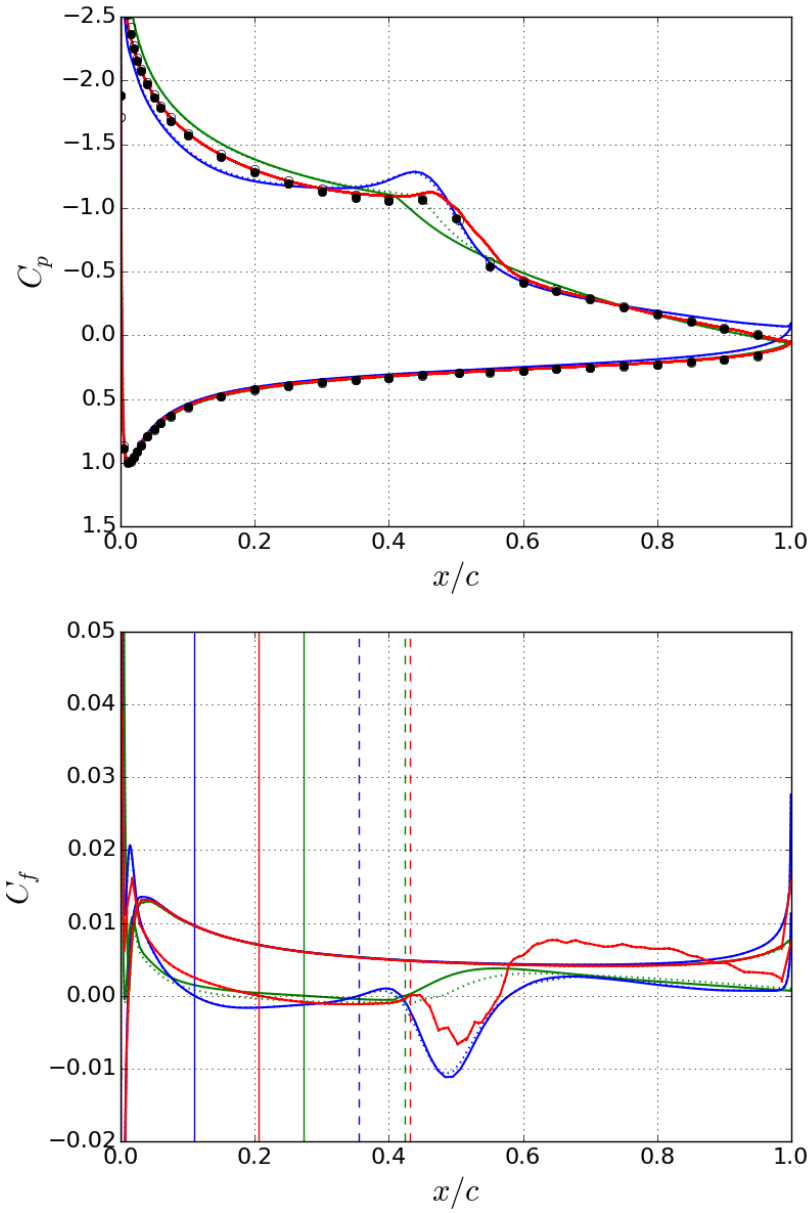


Figure 3.24: E387 airfoil at $Re = 6 \times 10^4$ and $AOA = 8°$: comparison of the chordwise pressure coefficient (top) and friction coefficient (bottom) obtained with XFOIL (solid $N_{crit} = 7$ and dotted $N_{crit} = 9$ green curves), URANS (solid $N_{crit} = 7$ and dotted $N_{crit} = 9$ blue curves) and the present wr-LES (red curves) to the experimental results (black $TI = 0.16\%$ and white $TI = 0.20\%$ circles) from [59]. Vertical solid and dashed lines present respectively the separation and reattachment locations.

3.3.3 Capture of the hysteresis at $Re = 6 \times 10^4$ and $AOA = 6°$

To investigate the possibility of predicting the performance jump and the hysteresis observed in the lift curve, one additional wrLES has been performed at $Re = 6 \times 10^4$ and $AOA = 6°$. The results are compared to DNS results obtained previously with Argo DG on a quite different mesh configuration [15].

Figure 3.25 presents the friction and velocity fields obtained during the computations. By comparing to the same flow fields presented in Figure 3.22 for $AOA = 4°$ and $AOA = 8°$, it seems that the computation stays in the continuity of these two, showing an LSB that moves towards the leading edge. This is confirmed by examining the pressure curve, see Figure 3.26.

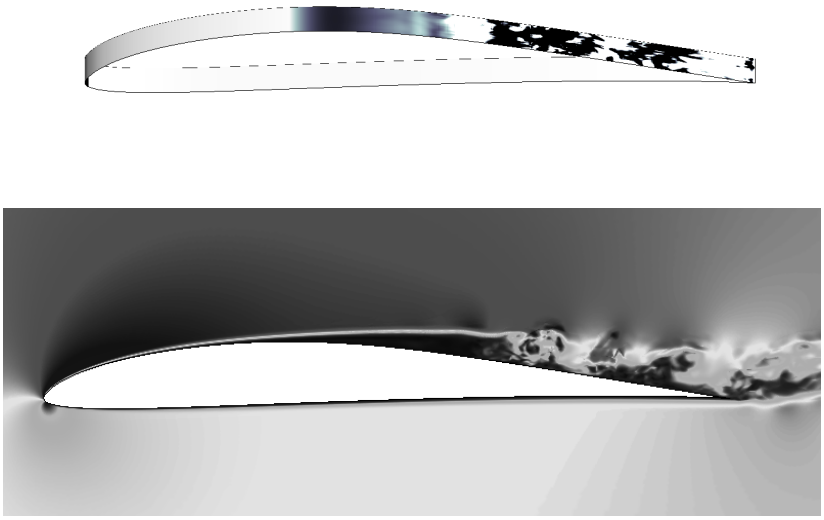


Figure 3.25: E387 airfoil at $Re = 6 \times 10^4$ and $AOA = 6°$: separation visualized by instantaneous x-aligned negative component of the friction (top) and instantaneous velocity in one plane (bottom). Note that friction goes from black (fully detached) to white (attached flow).

As for the S826 airfoil, the discrepancy between the wrLES and the experimental data calls into question the wrLES accuracy. Therefore, the wrLES results are compared to a DNS performed with Argo DG on a different type of mesh [15]. It is a C-shaped boundary layer mesh, it extends further in the spanwise direction (24% of the chord) and it has been refined according to DNS requirements with $\Delta x^+ \leq 5$, $\Delta y^+ \leq 1.1$ and $\Delta z^+ \leq 12$. Figure 3.26 compares the chordwise pressure coefficients obtained with the wrLES and the DNS to the experimental one. The DNS curve appears to be closer to the wrLES than to

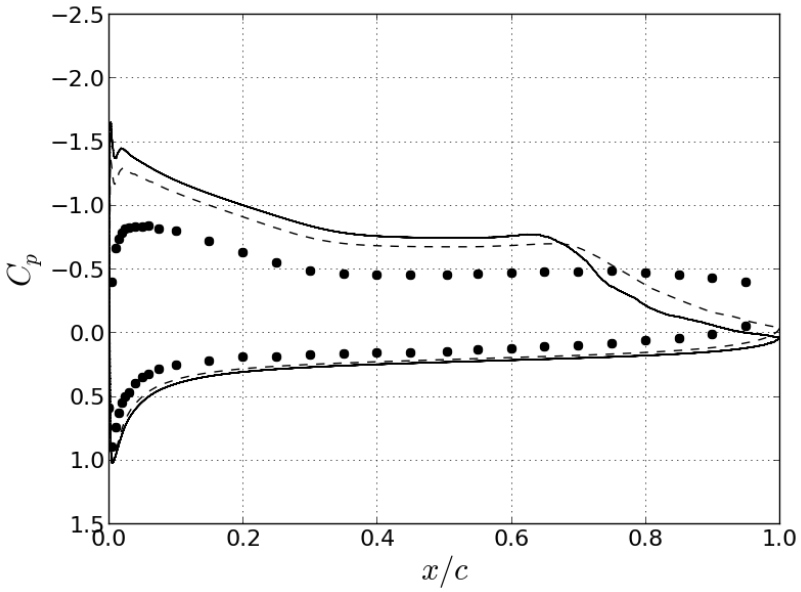


Figure 3.26: E387 airfoil at $Re = 6 \times 10^4$ and $AOA = 6°$: chordwise pressure coefficients. Comparison of the wrLES (plain line) and DNS (dashed line) performed with Argo DG to the experimental results from [59] (circle).

the experimental curve, thereby increasing the trust in the numerical quality of the wrLES. This tends also to confirm that the experimental conditions are difficult to reproduce numerically.

Furthermore, a careful analysis of the experimental data revealed, again, a strong sensitivity to the inflow turbulence. This extreme sensitivity can be observed in Figure 3.27. With an inflow turbulence of 0.16%, the laminar separation is followed by a transition to turbulence and a turbulent reattachment at 4, 5, 7 and $8°$. The exception is at $6°$, as if the LSB would burst at that specific angle. With an inflow turbulence of 0.20%, no reattachment appears before $8°$, impacting strongly the airfoil performance. Therefore, it is expected that with a zero inflow turbulence, as considered in the wrLES and DNS, the experiment at $6°$ will follow the general trend and a closer match would be obtained between the experimental and the numerical results.

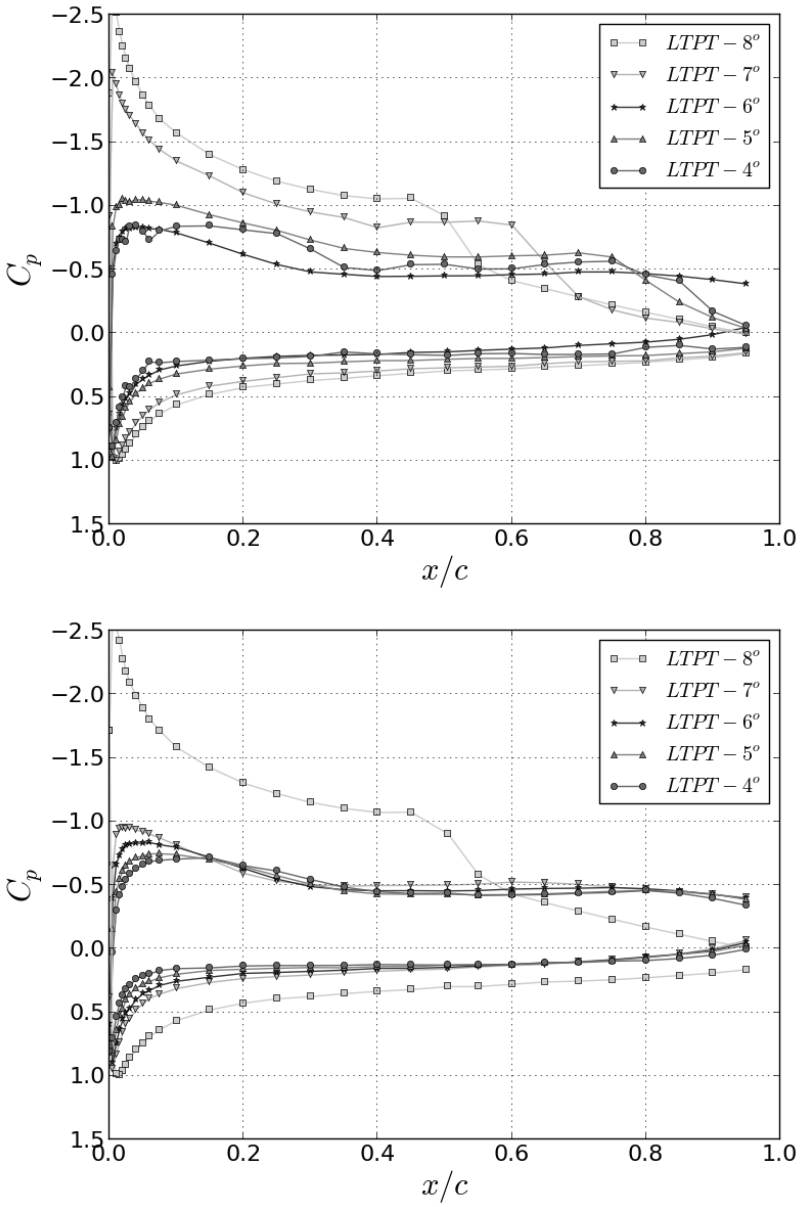


Figure 3.27: E387 airfoil at $Re = 6 \times 10^4$: chordwise pressure coefficient for five different angles of attack. Tunnel environment effect measured by McGhee *et al.* [59] for slightly different Mach (top 0.05, bottom 0.09) associated with different inflow turbulence intensities (0.16% top, 0.20% bottom).

3.4 Achievements

In this chapter, two low Reynolds number airfoils are analyzed, namely the S826 and the E387 airfoils. These two airfoils are considered relevant for the wind sector. For the two cases, various wrLES are performed and compared to both experimental and numerical references.

The S826 airfoil is analyzed at $Re = 4\times10^4$ and $Re = 1\times10^5$ for $AOA = 0°$ and $12°$. The pressure distributions over the airfoil as well as the lift and drag coefficients are compared to measurements and wrLES performed at DTU Wind. In the four cases, the wrLES results obtained by the two codes are very similar. As the discretization schemes, the SGS approaches and the meshes are totally different between the two numerical approaches, the fact that the wrLES performed with Argo DG matches the wrLES performed with EllipSys3D inspires a strong confidence in the validity of the computations.

Some differences are however observed with the experiments. To increase the confidence in the CFD results, further sensitivity analyses to the mesh and the span extent are performed, corroborating the initial results.

Also, further experiments by means of oil flow visualization are carried out. The results show small spanwise structures at $Re = 4 \times 10^4$, indicating that the span width of 10.5% of the chord used in the wrLES is sufficient for representing the flow.

At $Re = 1 \times 10^5$, the oil flow measurements show the formation of large stall cells and 3D effects. The study could not conclude on the origin of the stall cells in the investigated cases. Either a span length of about 10% of the chord is sufficient in CFD and the large structures observed experimentally are due to end walls or screw holes, or the stall cells are intrinsic flow structures and much larger spans need to be considered in CFD.

The E387 airfoil is first simulated at $Re = 6 \times 10^4$ for $AOA = 4°$ and $8°$. The force coefficients and surface pressure distributions are in very good agreement with the experiment, slightly better capturing the pressure distribution than the state-of-the-art tools (RANS and XFOIL). However, the additional wrLES made at $AOA = 6°$ fails in capturing the performance loss observed experimentally. The wrLES reveals an LSB, while no turbulent reattachment is observed in the experiment; the flow stays fully separated, leading to low performance, low lift and high drag force. To verify the quality of the wrLES, it is compared to a DNS computation, previously performed with the same code but on a different mesh-type. As the wrLES pressure curve is corroborating the DNS one, this test case confirms the quality of the wrLES and the complexity in comparing numerical to experimental databases.

Due to the extreme sensitivity of the low Reynolds number airfoil flows, their study is difficult, both at the experimental and the numerical level. Therefore,

these studies need to be performed with care. This leads to high uncertainties on the airfoil performance data, but also to important difficulties for the validation of CFD methodologies, as initially targeted by this research. Based on the difficulties observed in this study, we advice the following considerations when performing/choosing an experimental validation data set for CFD.

1. Time-averaged measurements can be misleading as the flow might oscillate between different regimes (e.g. small to large LSB) or exhibit hysteresis effects. In this case, the time evolution envelope and standard deviation should also be considered.
2. The flow is extremely sensitive to the tunnel environment, where small changes in inflow turbulence, interaction with the lateral walls, screws, taps and masking tape can have an important impact. Therefore, sensitivity analyses need to be performed and the openness about the results is crucial.
3. For some conditions large 3D stall cells may be observed. Experimentally, spanwise flow visualization and measurements at different spanwise location should be available to detect this condition. Numerically, a span sensitivity analysis is required and extremely high spanwise extents will have to be considered in order to capture the stall cells.

In view of the extreme sensitivity to the tunnel environment and considering the very good similarity between the numerical approaches, the results obtained in this chapter are considered as a strong step forward in the use of DG Method for solving low Reynolds number flows around airfoils. Further studies, based on inflow turbulence sensitivity analyses and on tunnel endwalls modeling as well as new experiments are expected to shed more light on the details of separation behavior and contribute to further reconcile the CFD simulations and experiments.

CHAPTER 4

TURBULENT CHANNEL FLOW

This chapter evaluates the wall-modeled Large-Eddy Simulation method on the turbulent channel flow. In addition to the validation of the wmLES approach, this chapter aims at defining guidelines on the use of wmLES in DGM through a rigorous sensitivity analysis. Various parameters are studied such as the wall model input location and the polynomial degree. This work has been published in the journal "Physics of Fluids" [31].

4.1 Motivation

As presented in Chapter 2, the wmLES approaches are usually differentiated by the type of wall models that are used and different models of varying complexity exist. Basic analytical models as the logarithmic law-of-the-wall enable a direct link between the LES input data and the wall shear stress. As these models are based on assumptions that limit their use to simple flow configurations (*i.e.* equilibrium flows without pressure gradients), more advanced models as the Two-Layer Model [6] are often preferred, even if they require to solve a system of equations. Although the errors due to the use of a basic or a more advanced wall model obviously have an impact on the accuracy of the global computation, the behavior of the numerical method on the coarse near-wall grid is at least as important, see Figure 4.1.

This inherent importance of the numerical errors started to be considered in the late nineties. Based on this idea that even a "perfect" wall model would never be sufficient to obtain a "perfect" wmLES, Nicoud *et al.* [64] suggested to apply a suboptimal control theory in place of the physically-based

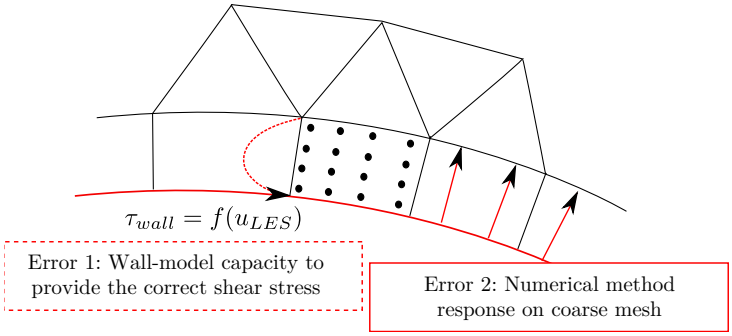


Figure 4.1: Illustration of the two main sources of errors faced with the Wall Stress approach. The wall-adjacent elements are obtained by extrusion of the wall, the other elements are not constrained, as desired for the current finite element approach. The markers represent approximately the position of the interpolation points in a fourth order accurate ($p = 3$) element.

wall models. The concept consisted in modifying the shear stress to obtain the required velocity profile, regardless of the numerical or modeling errors. However, the main approach in the wmLES community has been to keep the physically-based wall models and to reduce, or at least master, the numerical errors on the coarse near-wall grid.

In 2000, Cabot and Moin [14] showed that a considerable part of the wmLES error was coming from the inability of the subgrid-scale (SGS) model to be used on the coarse near-wall mesh. To solve this problem, they suggested a modification of the dynamic eddy-viscosity model close to the wall. In the same vein, Wu and Meyers [106] recently proposed a dynamic modification of the Smagorinsky SGS coefficient. These methods provide an improvement of wmLES accuracy. However, they are not applicable to the implicit LES (ILES) approaches, where the dissipation of the numerical scheme replaces the physical dissipation at the subgrid scale. For these implicit SGS approaches, there is obviously no coefficient that can be adjusted. The quantification and the control of the numerical errors are therefore even more crucial.

In 2012, Kawai and Larsson [47] proposed a solution to one of the most largely observed error in the wmLES community, the "log-layer mismatch" (*i.e.* error in the velocity profile). They stated that this error could be removed by changing the common practice that consists in taking the sampling data within the first off-wall grid point. This zone is, by definition, in an under-resolved region and, therefore, the input is of poor quality. By placing the sampling location at the third grid point, they could remove the mismatch and improve strongly their results. Using a different numerical method, Lee *et al.* [50] found as well an advantage in taking the input data further away from the wall. Lodato *et al.* [53] even suggested in their conclusions to dynamically adapt the input location depending on the resolution.

In a recent review on wmLES, Larsson *et al.* [48] observed that the "log-layer mismatch" is generally positive for the methods using a collocated grid or some numerical dissipation and negative for the methods using a staggered grid. The "perfect" wall model and the associated best practices (e.g. grid type, grid refinement, input position) can thereby not be transferred from one methodology to another. However, Larsson *et al.* [48] advise, for all numerical approaches, to perform a rigorous grid sensitivity study, varying the element dimensions and aspect ratios, while keeping the input location fixed and away from the first off-wall grid point.

For finite element approaches, where a large element with a high-order polynomial would typically replace several smaller elements of a finite volume or finite difference approach, it is not clear how these guidelines can be translated. For example, considering a fourth order element as presented in Figure 4.1, can we hope that the solution will be sufficiently good in the third or fourth off-wall points to be used as input data? If not, can the solution become acceptable in the first element by increasing the polynomial degree? Or does the input need to be in the second or third off-wall element? In the same logic, how does the polynomial degree affect the numerical error on the near-wall coarse grid? And could one order provide better properties when used in wmLES configuration than another?

Numerous studies based on finite volume or finite difference methods present guidelines on the use of wmLES. However, few studies have considered ILES and discontinuous high-order schemes as the Flux Reconstruction (FR), the Spectral Difference (SDM) or the Discontinuous Galerkin Method (DGM). As these methods offer high accuracy on unstructured low quality meshes, and are at the same time highly scalable, these methods are considered as highly promising for the use of LES on industrial applications [103]. Recently, Chen *et al.* [22], Lodato *et al.* [53] and Zhu *et al.* [107] presented encouraging wmLES results for respectively finite volume (with ILES), SDM (with ILES) and FR (with explicit SGS modeling) applied on the plane channel and the periodic hill test cases.

To the author's knowledge, best practice rules on the use and implementation of wmLES using discontinuous methods have not yet been published, and in particular not for ILES using DGM. The present chapter therefore focuses on a rigorous and systematic sensitivity analysis on the plane channel test case, resulting in practical guidelines for the application of wmLES with discontinuous high-order schemes. The chapter is organized as follows. Section 4.2 presents a sensitivity analysis of the plane channel flow at $Re_\tau = 5200$, illustrating the impact of various parameters such as the input location and the polynomial degree. The comparison of the average velocity profiles yields a preferred numerical configuration. Section 4.3 verifies these recommendations on a much higher Reynolds number ($Re_\tau = 50000$) and on unstructured cases to conclude, in Section 4.4, on best practice guidelines.

4.2 Sensitivity analysis at $\mathbf{Re}_\tau = 5200$

This section aims at evaluating, through a sensitivity analysis, the importance of the near-wall numerical error on the global wmLES result. The two first sections introduce the turbulent channel flow setup and the wmLES baseline cases. The three following sections permit to quantify the relative importance of the sampling position, the polynomial degree and the grid in order to suggest "best practices guidelines" for the use of wmLES techniques with a DG/ILES methodology. Finally, although these guidelines have been obtained for an instantaneous and local imposition of the wall model, they are tested for averaged approaches.

4.2.1 Computational setup

The plane channel flow test case consists of the fully developed turbulent flow between two parallel walls separated by a distance $2h$. Spanwise (z) and streamwise (x) periodicity are assumed at a distance of respectively πh and $2\pi h$. The friction Reynolds number $Re_\tau = u_\tau\, h/\nu = 5200$ is imposed through a constant pressure gradient forcing in the x-momentum equation. The DNS results by Lee and Moser [51] are used as reference as they constitute the highest Re_τ DNS that is available at the time of writing this work. The Mach number is kept at $M \simeq 0.1$ (based on the estimated bulk velocity) in order to approximate the incompressible conditions of the reference DNS.

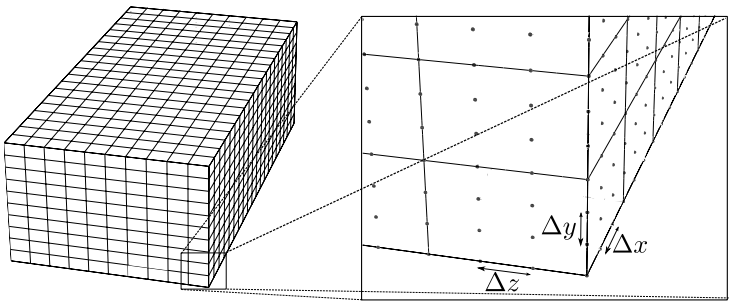


Figure 4.2: Effective resolution (Δx, Δy, Δz) in a fourth order accurate element ($p = 3$).

To limit the number of parameters in the sensitivity analysis, only structured hexahedral elements without stretching are considered. The interpolation points are hence separated by regular intervals $\Delta x_i = \frac{L_{x_i}}{n_{x_i} p}$ with L_{x_i} and n_{x_i} respectively the domain length and the number of elements in the directions $(x_1, x_2, x_3) = (x, y, z)$ and p the polynomial degree, as presented in Figure 4.2.

Although already presented in Section 3.2.1, the wall-resolved LES requirements defined by Choi and Moin [23] are recalled here to serve as comparison with the wmLES requirements

$$\Delta x^+ \simeq 50 - 130 \qquad \Delta y^+ \simeq 1 \qquad \Delta z^+ \simeq 15 - 30. \tag{4.1}$$

These grid requirements are tailored for the viscous sublayer. The wmLES approach, for its part, has grid requirements that depend on the outer boundary layer thickness only (with $\delta = h$ in the channel flow). Therefore, it makes more sense to describe the wmLES mesh in terms of δ than in terms of y^+. However, for the sake of clarity, the two notations are provided in this chapter. The recent review by Larsson *et al.* [48] suggests a resolution corresponding to $\Delta x \simeq 0.08\delta$, $\Delta y \simeq 0.01 - 0.05\delta$ and $\Delta z \simeq 0.05\delta$. For the channel test case at $Re_\tau = 5200$, this leads to a mesh having

$$\Delta x^+ \simeq 400 \qquad \Delta y^+ \simeq 50 - 250 \qquad \Delta z^+ \simeq 250, \tag{4.2}$$

hence much more than the values required for wall-resolved LES.

All computations of the parametric study will be solved using a second order accurate backward difference implicit time integration, with a timestep nondimensionalized using the eddy turnover time ($t_e = h/u_\tau$) as $\Delta\, t^+ = 1.10^{-3}$, which corresponds to 0.4% of a flow-through time ($t_c = L_x/U_b$). In all computations, at least three hundred flow-through times (*i.e.* about one hundred eddy turnover times) have been computed to evacuate the transient, leading to a kinetic energy variation of less than 0.5%. The convergence of the statistics is provided by both time averages over one hundred flow-through times (*i.e.* about 30 eddy turnover times) and spatial averages in the streamwise and spanwise directions. As described in Section 2.3, the wall model is based on Reichardt's law-of-the-wall and the input data can be taken everywhere in the first element as well as at its boundaries. Furthermore, the work aims at developing wmLES that uses polynomials of $p = 3$ or $p = 4$ as these are considered as optimal for wall-resolved LES using the present DG method [15].

4.2.2 Baseline cases using polynomials of degree 3 and 4

The design criteria for DGM lead to the definition of two baseline cases. The first, referred to as C1 in the remainder of the discussion, uses polynomial of degree $p = 4$ and the second, C2, uses polynomial of degree $p = 3$. In order to ensure a similar effective resolution between the two cases, the mesh for C1 is slightly coarser than that for C2 as illustrated in Figure 4.3 and as specified in Table 4.1.

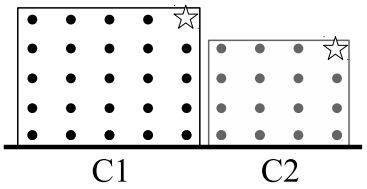


Figure 4.3: Schematic of C1 and C2 wall-adjacent element with five or four interpolation points to represent the polynomial degrees considered in each case ($p = 4$ for C1 and $p = 3$ for C2). The stars represent approximately the height where the wall model input is located.

To follow the recommendations suggesting to place the wall model input far enough from the boundary to be in a well resolved area, the input is located at the top of the wall adjacent element, see Figure 4.3. Table 4.1 presents the mesh refinement, the degree of the polynomial, the effective resolution (expressed in terms of δ and in wall units), and the distance to the wall where the input data is taken.

Figure 4.4(a) compares the velocity profile $\langle u^+ \rangle$ of C1 and C2 cases to the reference DNS data [51]. The notation $\langle \cdot \rangle$ indicates values that have been averaged in time and in both the x and z homogeneous directions. The wmLES result is represented by markers in order to visualize the degree of the polynomials. It appears that the wmLES result for the case C1 follows quite well the DNS curve with a slight overestimation of the velocity. However, the case C2 is much below the reference. The difference between the two cases is surprising. Even if an improvement going from $p = 3$ to $p = 4$ was expected, the difference still seems intuitively too large.

Figure 4.4(a) focuses on the part outside the inner layer, above the sampling point, reflecting common practice in the wmLES community. It is however interesting to observe the behavior of the wall-adjacent solution underneath the sampling location, especially if one wants to shed light on the difference between the case with $p = 4$ (C1) and $p = 3$ (C2). In this work, the velocity profiles will thence be plotted showing the polynomials of all elements and zooming on the connection between the first (wall-adjacent under-resolved) element and the second (resolved) element.

	Grid size	Deg.	Effective wall resolution		Input
	$n_x \times n_y \times n_z$	p	$\Delta x\ \Delta y\ \Delta z$	$\Delta x^+\ \Delta y^+\ \Delta z^+$	y_{wm}
	$[-]$	$[-]$	$[\%\delta]$	$[-]$	$[\%\delta]$
			Baseline cases		
C1	$20 \times 10 \times 10$	4	$8 \times 5 \times 8$	$400 \times 250 \times 400$	20
C2	$26 \times 13 \times 13$	3	$8 \times 5 \times 8$	$400 \times 250 \times 400$	15
			Wall model input position		
C3	$26 \times 13 \times 13$	3	$8 \times 5 \times 8$	$400 \times 250 \times 400$	12
C4	$26 \times 13 \times 13$	3	$8 \times 5 \times 8$	$400 \times 250 \times 400$	$B15$
C5	$20 \times 10 \times 10$	4	$8 \times 5 \times 8$	$400 \times 250 \times 400$	15
C6	$20 \times 10 \times 10$	4	$8 \times 5 \times 8$	$400 \times 250 \times 400$	$B20$
			Polynomial order		
C7	$40 \times 20 \times 20$	2	$8 \times 5 \times 8$	$400 \times 250 \times 400$	$B10$
C8	$16 \times 8 \times 8$	5	$8 \times 5 \times 8$	$400 \times 250 \times 400$	$B25$
C9	$26 \times 13 \times 13$	$B2/3$	$12 \times 8 \times 12$	$600 \times 400 \times 600$	$B15$
C10	$26 \times 13 \times 13$	$B4/3$	$6 \times 4 \times 6$	$300 \times 200 \times 300$	$B15$
C11	$26 \times 13 \times 13$	$B5/3$	$5 \times 3 \times 5$	$250 \times 150 \times 250$	$B15$
			Mesh refinement and aspect ratio		
C12	$40 \times 20 \times 20$	4	$4 \times 3 \times 4$	$200 \times 150 \times 200$	$B10$
C13	$40 \times 13 \times 20$	4	$4 \times 4 \times 4$	$200 \times 200 \times 200$	$B15$
C14	$26 \times 16 \times 13$	4	$6 \times 3 \times 6$	$300 \times 150 \times 300$	$B13$

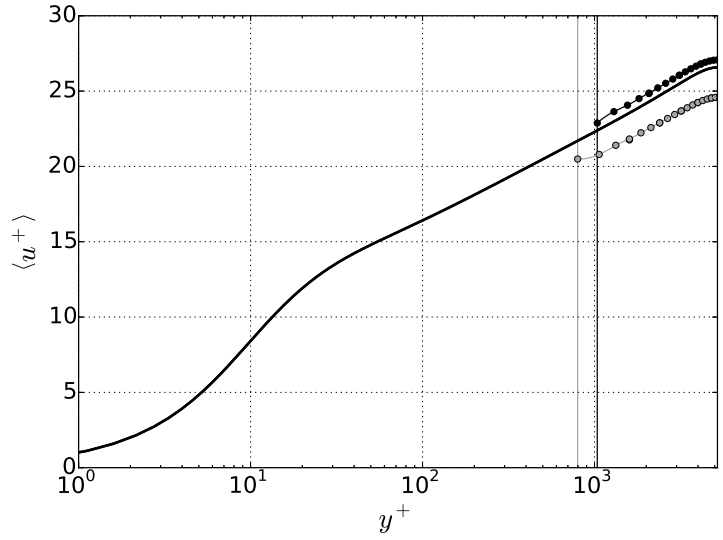
Table 4.1: Turbulent channel test cases description ($Re_\tau = 5200$): number of elements in each direction, polynomial degree, effective resolution (in terms of δ and of wall units, rounded to 50) and distance from the wall where the input velocity data is taken. For the sake of clarity, all cases are fully specified with shaded text for non changing parameters. The letter B is used in the sampling position column to differentiate the cases run in the "buffer element" configuration from the cases having the sampling location in the first off-wall element. When different polynomial degrees are used through the domain, the letter B is added next to the degree used in the "buffer element".

Figure 4.4(b) allows to observe that the value at the input position, hence the highest point of the first element, is very close to the DNS reference, for both cases C1 and C2. The fact that, at the input position, the velocity is not exactly on the DNS reference but only very close to it, seems to come from unsteady effects. The non-linearity of the wall model that is applied in an instantaneous and local manner makes that the averaged velocity divided by the averaged friction velocity is not exactly equivalent to the DNS reference value. This small mismatch and its relation to the averaged method will be discussed further in section 4.2.6. Figure 4.4(b) shows as well that, after the first element, the slopes of the velocity profiles appear to be correct. Therefore, to match the reference profile in the resolved region, one should reduce the large discontinuity between the first and the second element. It seems possible to reduce this jump by increasing the order of accuracy. However, it seems impossible

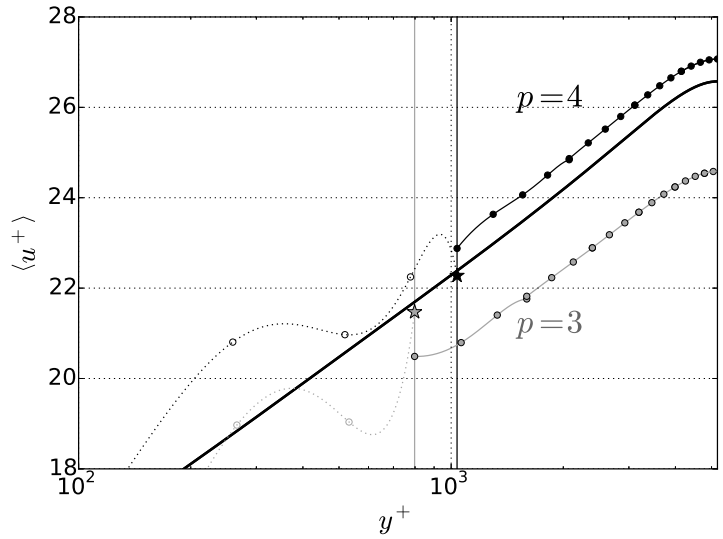
to remove it completely as, by construction, the first element is too coarse to solve the flow gradient correctly.

Figure 4.4(b) shows also that, in the under-resolved region, the solution exhibits an activation of all its inflection points, and thus a highly oscillatory character. These inflections are not problematic as, by virtue of DGM conservation property, the wall friction force is transmitted entirely through the upper element interface to the next cell. From the second cell onward, the gradient can be captured with good accuracy and an acceptable velocity profile is obtained. However, the number of the inflection points within the first cell differs between the $p = 3$ and the $p = 4$ cases. Therefore, the velocity profiles present different slopes in the approach of the top interface with a positive slope for $p = 3$ and a negative slope for $p = 4$. These different slopes induce jumps of opposite signs, negative for $p = 3$ and positive for $p = 4$, thereby leading in the resolved region to velocity profiles translated below (negative log-layer mismatch) and above the reference (positive log-layer mismatch), respectively.

Relying on the top of the wall-adjacent elements for the wall model input is then probably not an interesting option. Two potential solutions studied in the next section will involve the sampling of the input data at different locations. Firstly, the input will be taken inside the wall-adjacent element but closer to the wall and away from a potential discontinuity at the interface. Secondly, the point will be taken directly across the upper interface inside the next element.



(a) Classical visualization



(b) Visualization recentered on the bulk profile and the top interface of the first element

Figure 4.4: Mean velocity profiles of the two baseline wmLES cases: case C1 (black line with markers), case C2 (gray line with markers) and DNS reference [51] (black line without markers); the vertical lines and the stars indicate respectively the position and the value of the wall model input data. In each element, $p + 1$ equally spaced markers are used to represent the degree p of the Lagrange polynomial used. To distinguish the under-resolved and resolved regions, the polynomials are drawn with respectively dashed and solid lines.

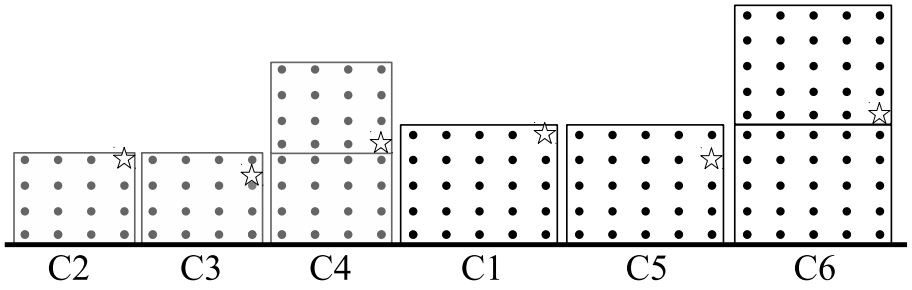


Figure 4.5: Schematic of C1 to C6 wall-adjacent element with four or five interpolation points to represent the polynomial degrees considered in each case ($p = 3$ for C2, C3 and C4 and $p = 4$ for C1, C5 and C6). The stars represent approximately the height where the wall model input is located. For C4 and C6 cases, a second element is drawn as the input is located at the bottom of the second element (*i.e.* using the "buffer element" configuration).

4.2.3 Impact of the input location

To evaluate the impact of the input location, which is in our case intrinsically linked to the wall-normal refinement, six different configurations are compared. Figure 4.5 shows a schematic of the six cases with, on the left, three cases with $p = 3$, and on the right, three cases with $p = 4$. Starting from the baseline cases (C2 for $p = 3$ and C1 for $p = 4$) where the input is taken at the top of the first element, the cases C3 and C5 take their input at 75% of the first element height. The cases C4 and C6 take their input at the interface with the second element, but, contrary to C2 and C1, using the value from the second element. In this case, the first element is considered as a buffer element and the cases are differentiated in Table 4.1 by adding the letter B in the input position specification.

Figure 4.6 compares the velocity profiles of the different configurations to the reference DNS data. It appears that displacing the input inside the first element or moving it to the second element improves the result. Moving the input position translates the velocity profile vertically until the input point is slightly below the DNS reference. For a given curve, the input position can then be optimized to match the DNS. We recall that the solution in the first element is unphysical, due to its under-resolution. The role of this first element lies solely in the transmission of the wall stress to its neighboring elements, as guaranteed by the conservativity of the DG formulation. Sampling information from within that element is then most probably a futile effort, as an optimized sampling position might very well be case dependent. The second element is much less impacted by under-resolution, and therefore taking the information there appears more robust. As for C1 and C2 in the previous section, it appears also here that the $p = 3$ and $p = 4$ cases react very differently. As they are based on equivalent resolutions, the large difference in behavior might be related to the polynomial order. The next section studies this effect.

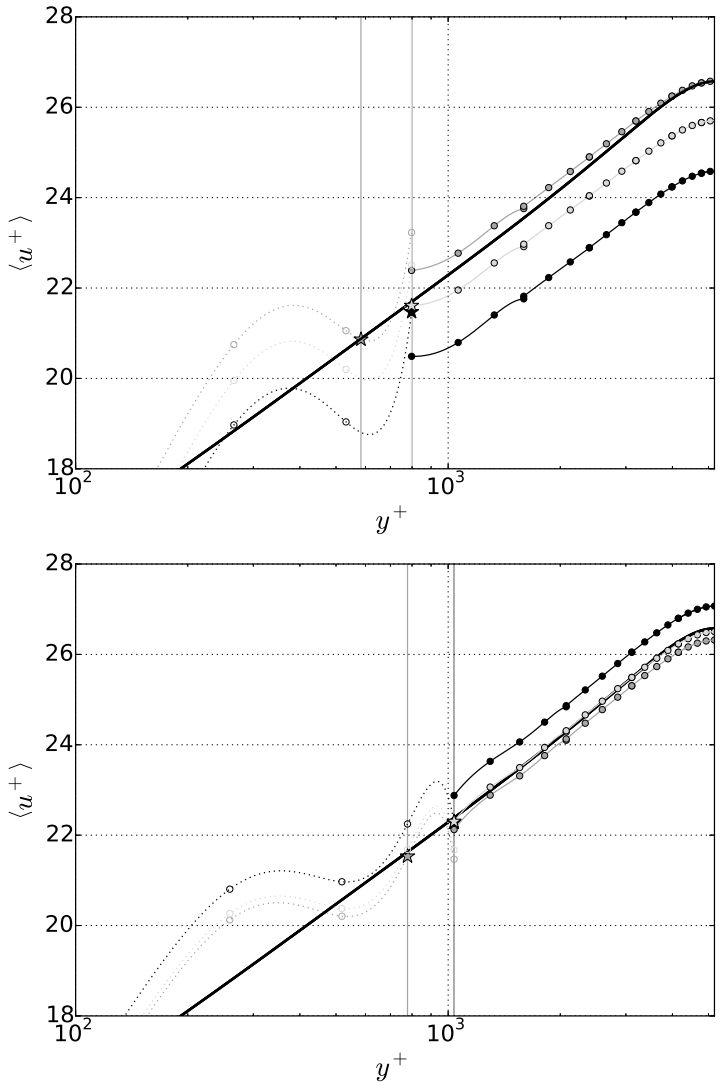


Figure 4.6: Mean velocity profiles of the wmLES cases with different wall model input positions: cases C2/C1 with input at the top of the first element (black line with markers), cases C3/C5 with input at 75% of the first element height (dark gray line with markers) and cases C4/C6 with input at the bottom of the second element (light gray line with markers) using $p = 3$ (top) and $p = 4$ elements (bottom); DNS reference [51] (black line without markers); the vertical lines and the stars indicate respectively the position and the value of the wall model input data.

4.2.4 Impact of the interpolation order

To evaluate the impact of the polynomial degree, four different configurations are compared, C7 ($p = 2$), C4 ($p = 3$), C6 ($p = 4$) and C8 ($p = 5$) with similar effective resolution as presented on the schematic of Figure 4.7 and as specified in Table 4.1. Based on the conclusion from the previous section, the input data is taken at the bottom of the second element (*i.e.* buffer element configuration).

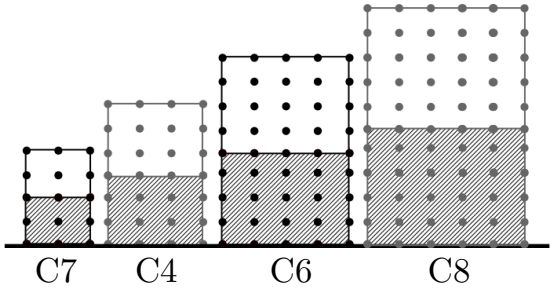


Figure 4.7: Schematic of the cases using different polynomial degrees but similar effective resolution with, from left to right, C7 ($p = 2$), C4 ($p = 3$), C6 ($p = 4$) and C8 ($p = 5$) cases. Even and odd degrees are differentiated by being drawn in respectively black and gray. Wall adjacent elements are hatched to express that the input is taken at the bottom of the second element according to the buffer element configuration.

Figure 4.8 presents the velocity profiles of the four cases, differentiating the odd from the even degrees. The odd/even cases were grouped together as they seem to have similar characteristics. The odd polynomial degrees overestimate the velocity at the top boundary of the buffer element, while even degrees under-estimate it at the same location. This difference could come from the number of inflection points in the buffer element. The odd cases have an odd number of inflection points and, for that reason, typically a positive slope at the interface with the second element. The even cases have a negative slope. The velocity jump between the first and second element is negative for the odd cases and positive for the even cases.

For both odd and even polynomials of degree p, increasing the degree to $p + 2$ reduces the jump and improves the result. It is however not true when increasing the order as $p + 1$ as C7 ($p = 2$) and C6 ($p = 4$) results are better than respectively C4 ($p = 3$) and C8 ($p = 5$) results. The difference between the odd and even orders seems to come from the respectively positive and negative slopes at the upper boundary of the first element, and hence would only depend on the order in this element.

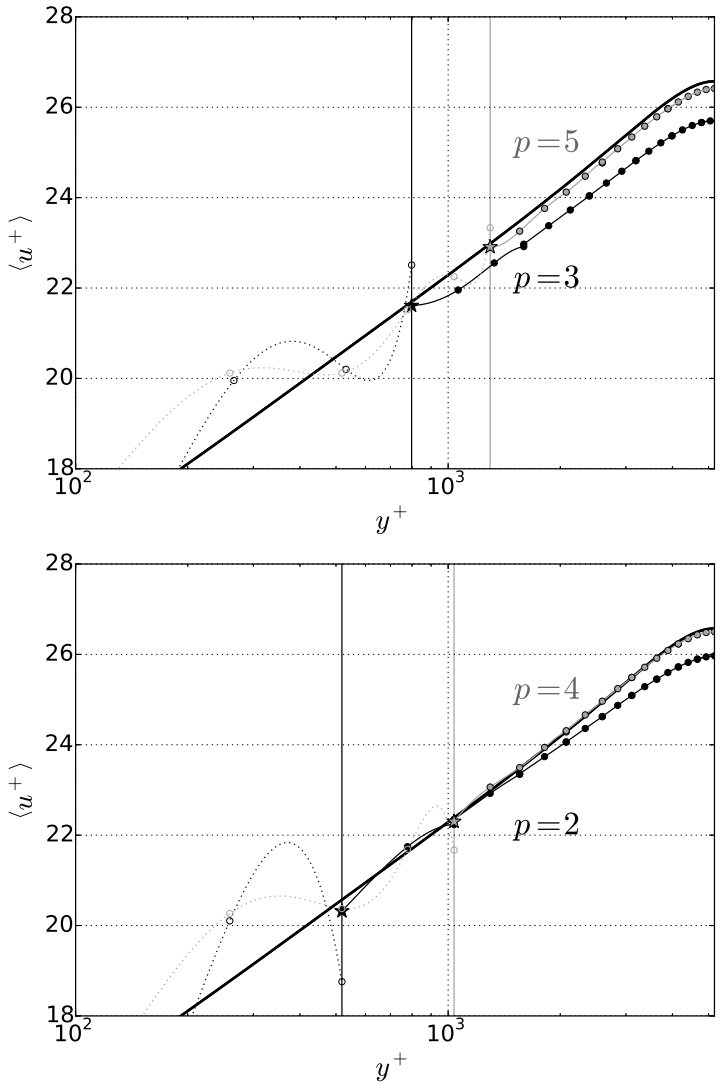


Figure 4.8: Mean velocity profiles of the wmLES cases with different polynomial degrees. Odd orders are on the top with $p = 3$ (C4-black line with markers) and $p = 5$ (C8-gray line with markers). Even orders are on the bottom with $p = 2$ (C7-black line with markers) and $p = 4$ (C6-gray line with markers). The DNS reference [51] is shown as a solid black line without markers. The vertical lines and the stars indicate respectively the position and the value of the wall model input data.

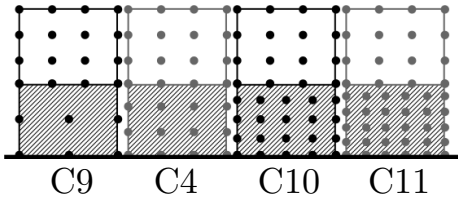


Figure 4.9: Schematic of the cases varying the polynomial degree in the first or buffer element only, with from left to right, C9 ($p_B = 2$), C4 ($p_B = 3$), C10 ($p_B = 4$) and C11 ($p_B = 5$) cases. Even and odd degrees are differentiated by being drawn in respectively black and gray. Wall adjacent elements are hatched area to express that the input is taken at the bottom of the second element according to the buffer element configuration.

To verify this, four other cases are compared using a constant polynomial degree $p = 3$ in all the domain except for the buffer element in which the order is varied from $p_B = 2$ to $p_B = 5$, as presented in Figure 4.9. The choice for $p = 3$ in the largest part of the domain is inspired by the design desiderata specified in Section 2.3.3.

Figure 4.10 confirms that the overall shape is driven by the polynomial degree in the first element. To use the wmLES approach in this DG methodology the first element should then be of an even degree and preferably $p_B = 4$ to minimize the jump at the interface. The degree in the rest of the domain can be chosen freely, to conform to other considerations. The remainder of this chapter mainly considers mesh refinement studies which will be performed with $p = 4$ polynomials in the entire domain. For completeness, similar grid sensitivity studies with buffer elements of $p_B = 4$ and $p = 3$ in the rest of the domain are provided in Appendix A.1. Furthermore, to limit the scope of the study, only the velocity profiles are compared in the chapter but the fluctuations are provided in Appendix A.2.

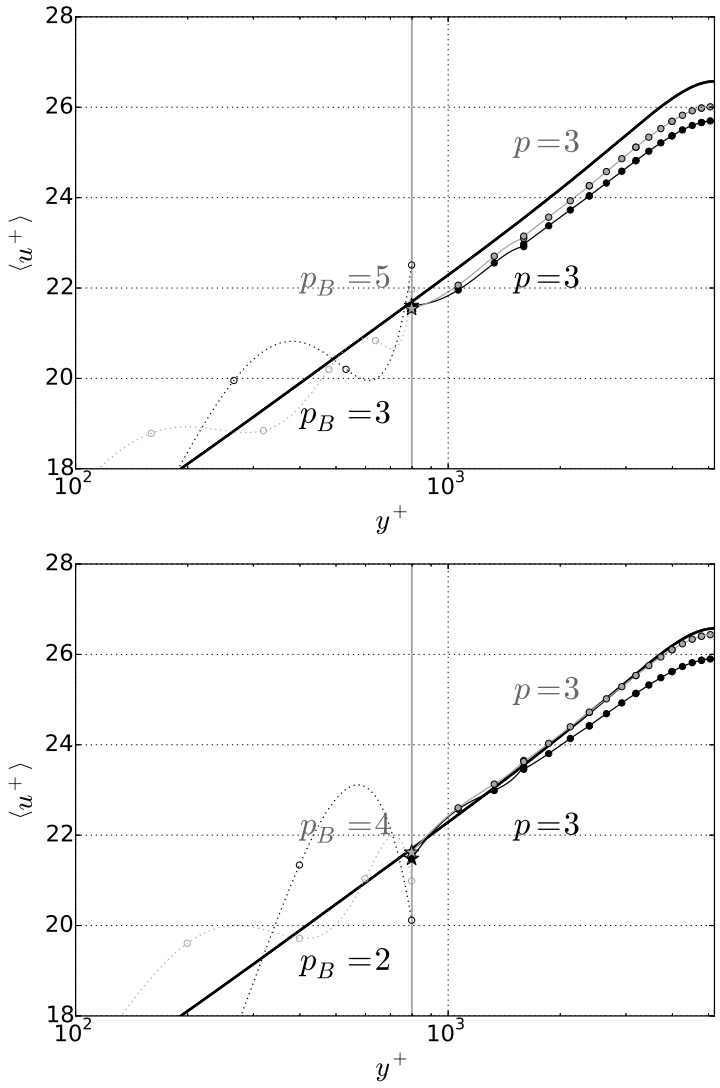


Figure 4.10: Mean velocity profiles of the wmLES cases with different polynomial degrees in the buffer element. Odd orders are on the top with $p_B = 3$ (C4-black line with markers) and $p_B = 5$ (C11-gray line with markers). Even orders are on the bottom with $p_B = 2$ (C9-black line with markers) and $p_B = 4$ (C10-gray line with markers). The DNS reference [51] is shown as a solid black line without markers. The vertical lines and the stars indicate respectively the position and the value of the wall model input data.

4.2.5 Grid refinement and aspect ratio study

To evaluate the impact of the grid refinement, the case C12 is created by dividing the mesh of the case C6 twice in the three directions, hence keeping the same aspect ratio between the elements. The aspect ratio used up to now in this chapter was $\frac{\Delta x}{\Delta y} = \frac{\Delta z}{\Delta y} = AR = \pi/2$. To evaluate the impact of the aspect ratio while keeping the initial constraint of $\Delta x = \Delta z$, two cases are considered: the case C13 with $AR = 1$ and the case C14 with $AR = 2$. These ratios have been chosen to be in the range of those used in the state-of-the-art wmLES approaches as provided on Table 4.2 for turbulent channel flow studies.

Reference	Re_τ	Aspect ratio	
		$\frac{\Delta x}{\Delta y}$	$\frac{\Delta z}{\Delta y}$
Balaras *et al.* [6]	2000	π	1.0
Cabot *et al.* [14]	4000	π	1.1
Chen *et al.* [22]	2000	π	$\pi/2$
Lodato *et al.* [53]	2000	$\pi/2$	$\pi/2$

Table 4.2: Aspect ratio used in the literature for wmLES of the turbulent plane channel flow at similar Reynolds numbers.

Examining the velocity profiles in Figure 4.11, it appears that refining the mesh does not change significantly the result. Using a mesh $\Delta x \times \Delta y \times \Delta z$ of $0.08\delta \times 0.05\delta \times 0.08\delta$ seems hence sufficient. Figure 4.11 shows also that, for the considered test cases with $1 \leq \frac{\Delta x}{\Delta y} = \frac{\Delta z}{\Delta y} \leq 2$, the aspect ratio does not impact the result.

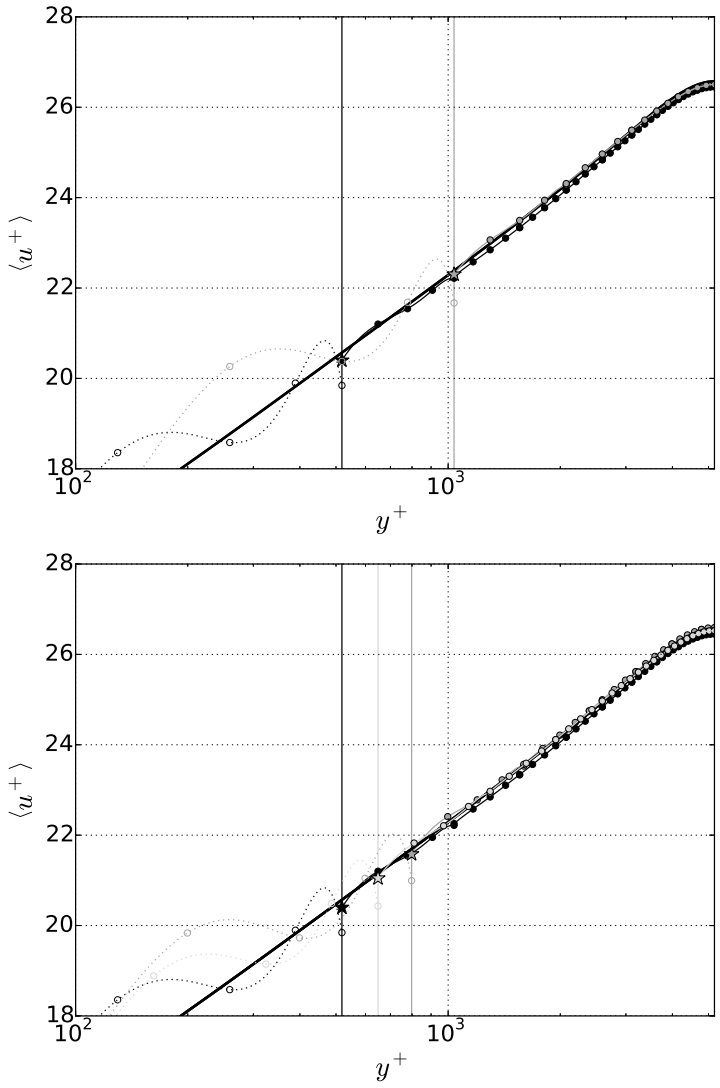


Figure 4.11: Mean velocity profiles of the wmLES cases with different meshes. Refinements with constant element aspect ratio are on the top with the baseline (C6-dark gray line with markers) and the refined case (C12-black line with markers). The different aspect ratios are on the bottom with the baseline aspect ratio $AR = \pi/2$ (C12-black line with markers) versus the smaller $AR = 1.0$ (C13-dark gray line with markers) and bigger $AR = 1.9$ (C14-light gray line with markers) aspect ratios. The DNS reference [51] is shown as a solid black line without markers. The vertical lines and the stars indicate respectively the position and the value of the wall model input data.

4.2.6 Space and time averaging

The analytical profiles are only applicable to the mean flow, and therefore, theoretically, the wall model should be evaluated using averaged flow quantities. In fact, most of the wmLES approaches are applied in an averaged manner [48].

The use of averaged quantities adds considerable complexity to the code in case of spatial averaging, and may impede statistical convergence for time-averaging. Moreover, for many applications neither spatial nor temporal statistical homogeneity is present. Therefore, until now, neither space or time averaging were considered in the studies.

It is however interesting to determine the impact of averaging in this particular case, as in this case it actually makes sense (*e.g.* extruded span and constant inflow). In case a significant impact is found, this should be taken into account for the further development.

In the present section, two different averaging approaches are evaluated. Figure 4.12 presents these approaches in regard to the approach used previously. The local and instantaneous approach will first be compared to a space averaged but instantaneous approach, then to a local but time averaged approach.

One constraint in this study being to limit the communication between the elements, the space average is performed here by using the control points of one element. In this approach the input velocity is based on the average over all interpolation points from an element which are placed at a certain distance from the wall. In this case the average is hence performed over the 25 points ($p = 4$) placed at the bottom interface of the second element. As suggested by Schumann [83], the mean shear stress which is calculated based on this mean velocity is then multiplied by the local and instantaneous velocity variation

$$\tau_w = \langle \tau_w \rangle \, \frac{u_\parallel}{\langle u_\parallel \rangle}. \tag{4.3}$$

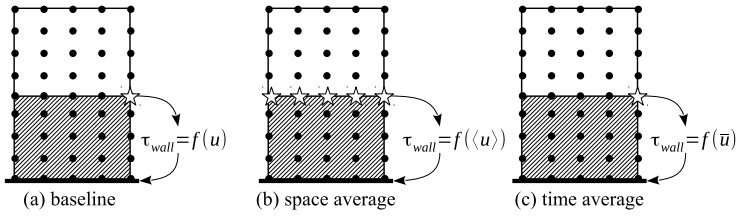


Figure 4.12: Sketch of the different evaluated averaging methodologies. Wall adjacent elements are hatched area to express that the input is taken at the bottom of the second element according to the buffer element configuration.

For the time average, the wall model input velocity is given by

$$\overline{u_\parallel(t)} = \overline{u_\parallel(t-dt)}\, e^{-dt/T} + \left(1 - e^{-dt/T}\right) u_\parallel, \tag{4.4}$$

where the timescale depends on the simulation timestep dt, and the bulk velocity U_b ($T = h/U_b$). As for the space averaging, the shear stress is applied using Schumann's relation. Both the time and space average approaches are presented in Figure 4.13 in regards to the baseline case C6. The difference between the three techniques is almost not distinguishable, confirming Lee *et al.* [50] who showed that imposing a mean value instantaneously was sufficient to accurately predict the mean velocity profile.

The zoom near the input location in Figure 4.13 permits to observe small differences between the three approaches. These differences lie in the application of the non-linear relation $u^+ = f(y^+)$ before or after the averaging of u and τ_w. The (small) mismatch observed previously for the non-averaged method thus results from this averaging commutation errors. Both averaging methods improve the agreement with the DNS reference with respect to the baseline approach. The match is even excellent for the time-averaged approach. For the averaging in space, a larger sampling region would likely allow to mimic the time-averaged method. The improvements brought by the averaging seem however too small to justify the overhead and reduced applicability of averaged approaches. Therefore, the remainder of this work will focus on the baseline approach, using instantaneous and local values.

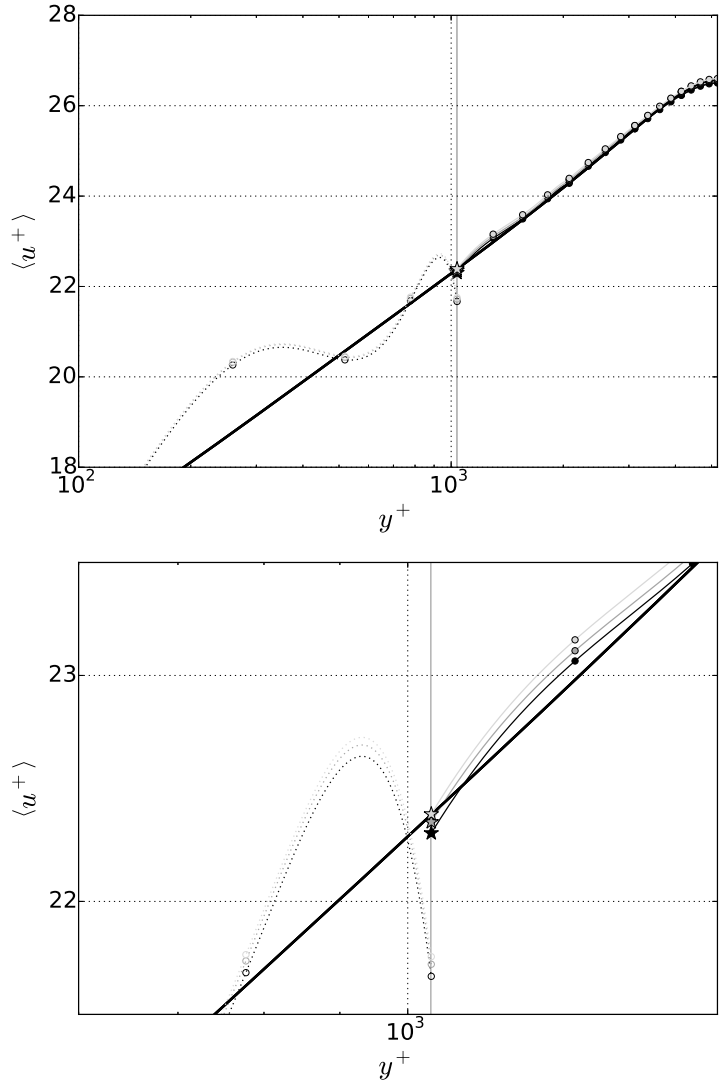


Figure 4.13: Mean velocity profiles of the wmLES cases with different averaging approaches: the baseline pointwise and instantaneous approach (black line with markers) is compared to the space averaged (dark gray line with markers) and time averaged (light gray line with markers) approaches. A global view is provided on the top, a closed view is given on the bottom. The DNS reference [51] is shown as a solid black line without markers. The vertical lines and the stars indicate respectively the position and the value of the wall model input data.

4.3 Additional evaluation: unstructured meshes and $\mathbf{Re}_\tau = \mathbf{50000}$

To limit the extent of the previous parametric study, only structured meshes at $Re_\tau = 5200$ were considered. As one of the main interests of the DG methodology is the geometric flexibility, it is important to test the wmLES approach on unstructured meshes. In that purpose, the case C6 has been adapted to two test cases as presented in Figure 4.14.

To evaluate the capacity of the method to model higher Reynolds number flows, a turbulent channel flow at $Re_\tau = 50000$ is also considered. As the wmLES mesh is supposed to depend only on the boundary layer height, and not on y^+, the mesh used in the previous section for the case C6 is kept.

Figure 4.15 compares the velocity profiles obtained with the three meshes. The fact that the three meshes provide as good results as the structured mesh indicates that the developed wmLES methodology can be extended to more complex meshes. Meanwhile, Figure 4.16 compares the wmLES performed at $Re_\tau = 5200$ and $Re_\tau = 50000$ and shows that the velocity profile obtained at $Re_\tau = 50000$ follows perfectly the theoretical law. Therefore, these two figures provide very promising results both for the use of unstructured meshes and the increase of the Reynolds number. It confirms that the wmLES approach permits to limit the mesh requirements and to model high Reynolds number flows for a limited computational cost.

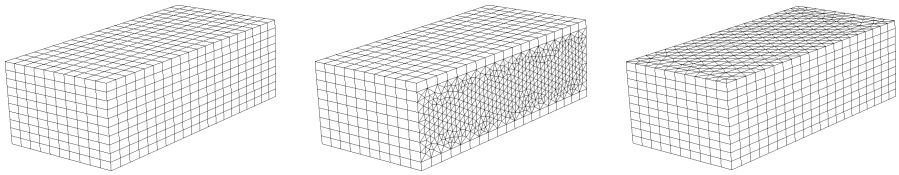


Figure 4.14: Structured (left - original case C6), x-unstructured (center) and z-unstructured (right) meshes.

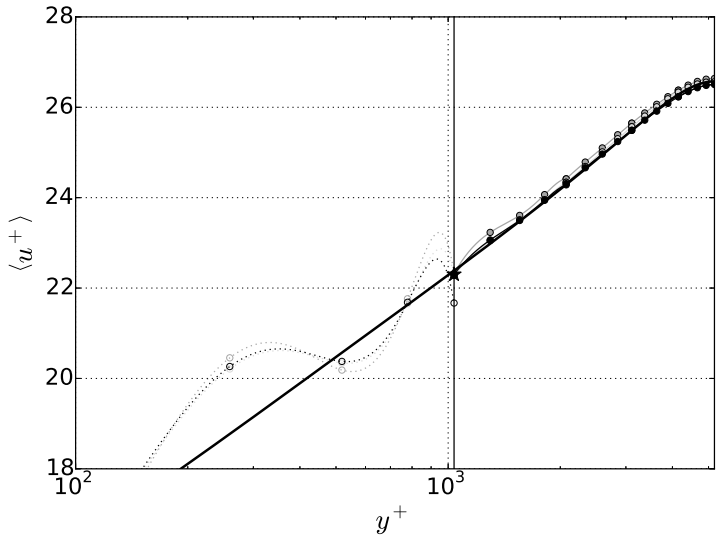


Figure 4.15: Mean velocity profiles of the wmLES cases with different types of mesh: the baseline structured mesh case (black line with markers), the x-unstructured mesh case (dark gray line with markers) and the z-unstructured mesh case (light gray line with markers). The DNS reference [51] is shown as a solid black line without markers. The vertical lines and the stars indicate respectively the position and the value of the wall model input data. For the x-unstructured case the markers are representing an equivalent order and refinement rather than the actual position.

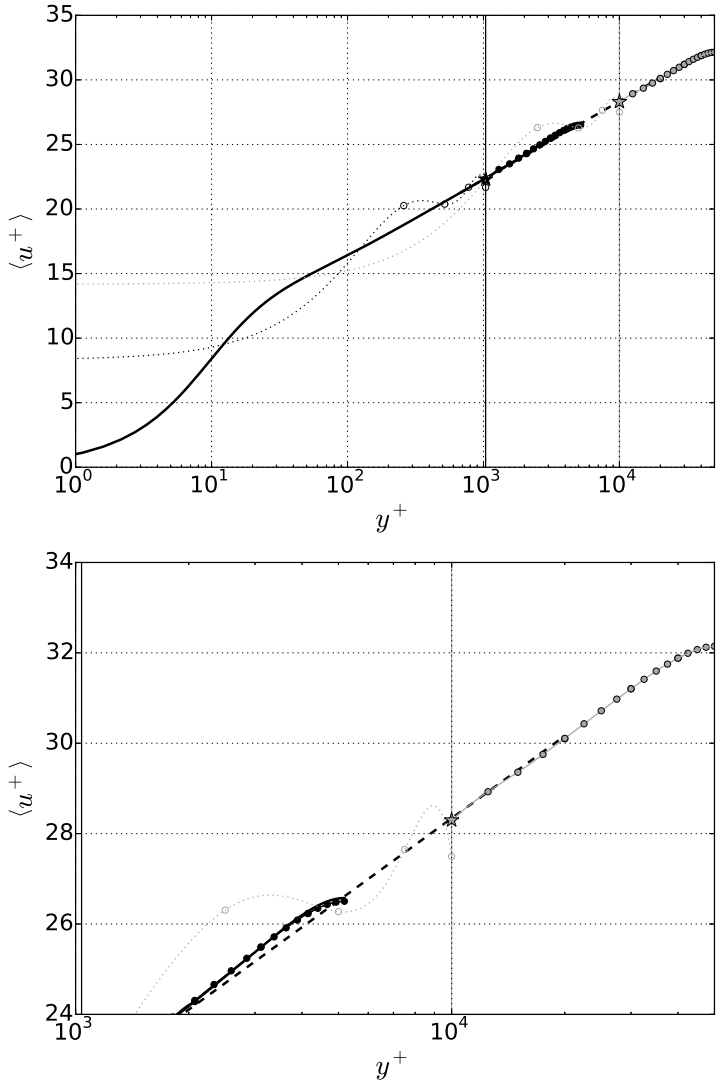


Figure 4.16: Mean velocity profiles of the wmLES cases at different Re_τ: the baseline $Re_\tau = 5200$ case (black line with markers) and the $Re_\tau = 50000$ case (gray line with markers). A global view is provided on the top, a closed view is given on the bottom. The DNS reference [51] at $Re_\tau = 5200$ is shown as a solid black line without markers. The log-law is used as reference for the case at $Re_\tau = 50000$ (dashed line without markers). The vertical lines and the stars indicate respectively the position and the value of the wall model input data.

4.4 Conclusions and best practice guidelines

In this chapter, the wmLES approach has been successfully validated. To thoroughly evaluate the impact of the numerical errors on the global wmLES accuracy, this chapter presents a sensitivity analysis on the turbulent channel flow. This work is, according to the author's knowledge, the first to perform a rigorous and systematic characterization for a discontinuous finite element method. Therefore, in addition to the guidelines provided in the wmLES community [48], this work focuses largely on the influence of the polynomial degree on the total wmLES precision. The sensitivity analysis indicates the following best practice guidelines.

- Averaging procedures do not seem to improve the results compared to a pointwise and instantaneous application, thus preserving a full mesh flexibility and scalability.
- The wall model input data should not be taken at the top of the wall-adjacent element, where the solution is very irregular. The most accurate and robust option appears to be achieved through sampling points located at the bottom interface of the second element. In this configuration, the first element is considered as a "buffer element".
- The degree of the polynomial in the buffer element p_B appears to be of high importance. For the DG method used in this work, it should be of even degree and preferably at least $p_B = 4$. If this is not possible, $p_B = 2$ is still better than $p_B = 3$. The order in the remainder of the domain has less importance and can be chosen on the basis of other considerations (*e.g.* mesh complexity and computational resource).
- The mesh resolution $\Delta x = \Delta z \simeq 0.08\delta$ and $\Delta y \simeq 0.05\delta$ seems sufficient to capture the flow irrespective of the Reynolds number, and is therefore independent of wall units.
- Element aspect ratios in the range $1 \leq \frac{\Delta x}{\Delta y} = \frac{\Delta z}{\Delta y} \leq 2$ provide equivalently accurate results.
- The type of elements (rectangular cuboids or triangular prisms) has limited impact on the results. The only apparent restriction identified in this study is the requirement for extruded wall-adjacent elements (*i.e.* right prisms). This restriction is assumed here to limit the scope of the study and should, therefore, be more extensively studied to provide complete guidelines.

Although the sensitivity study is performed mainly at $Re_\tau = 5200$ and for structured meshes, some cases are performed at $Re_\tau = 50000$ and for unstructured meshes. Following the previous guidelines, all cases provide promising results. This work is hence an important step forward in the use of wmLES for discontinuous finite-element-like methods.

As the wmLES results depend in part on the numerical dissipation caused by the near-wall coarse grid, the precise conclusions concerning resolution, interpolation order and matching location might not be transferred directly to

another method. However, the main guidelines is likely transferable to all discontinuous finite-element-like methods (DGM, FR, SDM). For example, although the use of $p_B = 4$ might not be the best option for other methods, the finding that increasing the order in the wall-adjacent element helps in reducing the error but is much less efficient than taking the information in the second element is likely transferable. In the same vein, the large difference observed between the even and odd polynomial degrees should at least be used as warning for future wmLES implementations with finite elements. Finally, given that spatial averaging impedes scalability, that temporal averaging slows down statistical convergence and that both require homogeneity, the fact that one can use an instantaneous and local application of the model is an important conclusion for all practical computations.

To solve complex industrial flows, some further steps are needed. On one hand, the wmLES method developed here should be evaluated on more complex flow configurations that comprise pressure gradients, transition and separation. For this purpose, wmLES with the equilibrium wall model considered here is performed in the next chapter on the NACA4412 airfoil test case. On the other hand, the equilibrium wall model should be upgraded to take into account these physical complexities. To this end, the validity of different wall models is assessed in a priori manner in the next chapter.

CHAPTER 5

HIGH REYNOLDS NUMBER AIRFOILS

This chapter starts by presenting a wall-modeled LES of an airfoil at high Reynolds number and at near-stall condition. The NACA4412 airfoil is a widely used test case for the validation of turbulence models. To evaluate the quality of the simulation, a wall-resolved LES of the exact same test case is performed. In addition to the deep analysis of the airfoil aerodynamics, the wrLES data is used to compare different wall models and to conclude on their respective ability to represent a turbulent boundary layer subject to an adverse pressure gradient. This work [32], presented at DLES11 conference, has been selected for a special edition in the journal "Flow, Turbulence and Combustion" and is, at the time of writing this thesis, under review. This work also permitted to obtain the PRACE computational allocation "R2Wall" to reproduce the computation on a larger span extent. As these simulations are currently ongoing at the BlueGene/Q system "JuQueen" at the Jülich Supercomputing Centre, only a few preliminary results are presented in this work.

5.1 Motivation

As presented in Chapter 3, the low Reynolds number airfoils are of high interest for the laboratory-scaled wind turbines and for the development of the design tools. However, the Reynolds numbers observed by the medium-size and large wind turbines are much larger, of at least a million. Therefore, it is important to capture also the flow physics of high Reynolds number airfoils. In order to do so without increasing the computational cost too dramatically, we use the wmLES methodology developed in Chapter 4.

For this analysis, the NACA4412 airfoil is chosen as it is a well documented test case frequently used in code comparisons. Furthermore, it has been recently studied for testing different wmLES methods [67, 11]. The main benchmark associated to this airfoil, referred to as 2DN44 in the NASA database, concerns $Re = 1.52 \times 10^6$ and $\alpha = 13.9°$, based on the Coles and Wadcock experiment from 1979 [27]. However, a later work from Wadcock [101] demonstrated that the original experiment was subject to strong tunnel effects and that the characteristics measured at $\alpha = 13.9°$ were more representative of a flow at $\alpha = 12.0°$. Therefore, the simulations considered in this work use the later experiment performed by Wadcock in 1987 [101] with $Re = 1.64 \times 10^6$ and $\alpha = 12.0°$.

At this condition, the flow over the suction side of the NACA4412 airfoil presents a short laminar region, a laminar/turbulent transition and a separation close to the trailing edge, at $\simeq 85\%$ of the chord [101]. As the wall model developed in Chapter 4 uses Reichardt's law-of-the-wall and assumes an equilibrium turbulent boundary layer, the laminar region, the transition and the separation will *a priori* not be captured adequately by the model. However, it is interesting to evaluate the performance of the most computationally affordable model before testing more advanced wall models.

5.2 NACA4412 airfoil: wall-modeled LES

As for the E387 airfoil presented in Chapter 3, the results provided by the LES approach are compared to XFOIL and RANS predictions, considered as the state-of-the-art tools within the wind industry. The XFOIL and RANS computations have been performed by Niels Sørensen from DTU Wind.

5.2.1 Numerical setup

The mesh methodology is equivalent to the one used for the E387 airfoil (see Section 3.3), using an O-type mesh around the airfoil with quadrangles in the boundary layer and triangles in the rest of the domain. However, whereas the mesh required for the RANS is refined to keep $y^+ \simeq 2$, the wmLES mesh is kept almost identical to the one of the E387 at $Re = 6 \times 10^4$.

According to the guidelines developed in Chapter 4, the wall model input needs to be taken at the bottom interface of the second element and it should be at about 20% of the boundary layer thickness δ. As δ varies along the chord and as the mesh quality limits us to use first elements that have a constant normal height, the height needs to be taken in order to have $y_{wm} = 0.2\delta$ on most of the chord.

Figure 5.1 presents the boundary layer thickness measured by Wadcock [101]. It appears that the boundary layer grows largely on the airfoil. It stays lower than 1% of the chord on the first 35% of the chord and then increases to more than 10% close to the trailing edge. Note that, on the last 25% of the

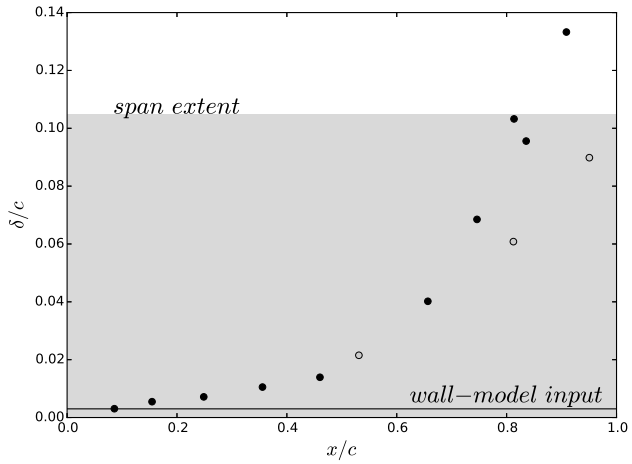


Figure 5.1: Boundary layer thickness along the chord measured by Wadcock [101] with two different measurement techniques (black and gray circles). The horizontal black line represents the height of the first grid element and thus also the position of the wall model input. The gray area represent the span extent of the computation.

chord, the experiment provides a strongly varying boundary layer thickness. At $x/c = 0.8$ for example, two results are provided, one with $\delta \simeq 6\%$ and $\delta \simeq 10\%$. These differences come from the fact that Wadcock used two different measurement techniques and they illustrate the complexity in the acquisition of accurate boundary layer thicknesses.

Considering this significant growth of the boundary layer and a trade-off between accuracy and grid cost, the first element height is taken in order to fulfill $y_{wm} = 0.2\delta$ around the mid-chord position. Figure 5.1 compares this height to the evolution of δ as well as the total span extent. It appears that the boundary layer thickness δ is of the same order as the span in the last 20% of the chord. Although it is advised to use a span extent of at least 5 times δ [44], this is not possible here due to the limitation in the computational resources.

Still, to follow the guidelines developed in Chapter 4, the mesh at the wall follows approximately $\Delta x = \Delta z = 2\Delta y$ and polynomials of even degree are used in the wall-adjacent (buffer) element. To limit the computational cost, the discretization is third order accurate ($p = 2$) in the buffer element and fourth order accurate ($p = 3$) in the rest of the domain. The mesh leads to approximately $8M\ dof$; that corresponds to an increase as $Re^{0.35}$ with respect to the computation of the E387. The average resolution in wall units on the suction side is characterized by $\Delta x^+ \simeq 200$, $\Delta y^+ \simeq 100$ and $\Delta z^+ \simeq 200$.

As for the E387 airfoil, the wmLES results presented here are averaged along the span and three flow-through times ($ftt = c/u_\infty$). Figure 5.2 presents the

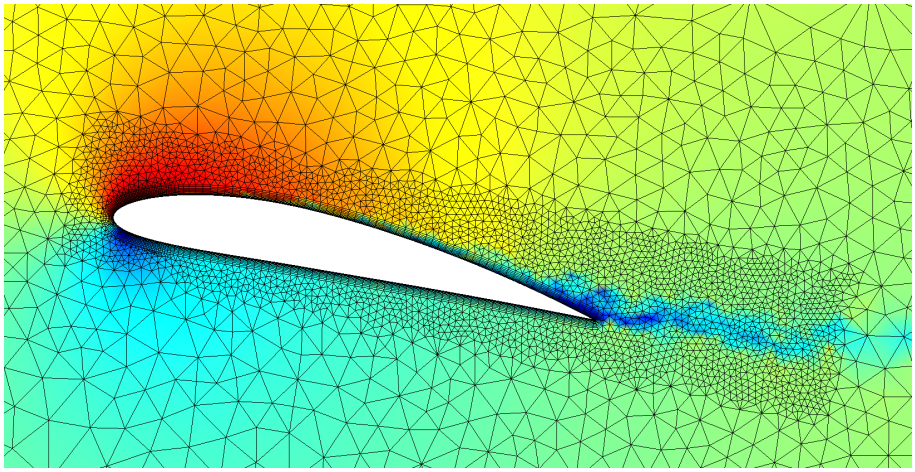


Figure 5.2: View of the 2D mesh for the wmLES of the NACA4412 at $\alpha = 12^\circ$ and $Re = 1.64 \times 10^6$ and instantaneous velocity field.

mesh obtained with this method together with an instantaneous velocity field in one plane. Note that, considering the doubts about the adequacy of the mesh and of Reichardt's wall model for this type of flow, the wmLES presented here needs to be considered only as a first step to understand the potential of wmLES to perform LES of high Reynolds number airfoils. The first test, to see the value added by the wall model, is to run a LES with this mesh but with no-slip wall conditions, hence under-resolved wrLES. This case could not converge, most likely due to the too coarse mesh, not able to capture the gradients. Therefore, although not perfect, the wall model helps already the computation.

5.2.2 Comparison to state-of-the-art tools

Figure 5.3 compares the lift and drag coefficients obtained numerically to the experiment of Wadcock [101]. As XFOIL and RANS calculations are affordable, the full polar are computed for $0^\circ \leq \alpha \leq 16^\circ$. RANS and XFOIL results match well the experiment for $\alpha \leq 10^\circ$ and then the difference grows markedly, especially beyond the stall angle $\alpha \geq 12^\circ$. This difference between the numerical and the experimental data illustrates the need to better capture the flow physics for high Reynolds number airfoils at near-stall angle.

At $\alpha = 12^\circ$, the three modeling tools provide a similar lift coefficient that is slightly higher than the lift measured by Wadcock. For the drag coefficient, XFOIL and RANS values are again similar but the wmLES prediction is a bit closer to the measurement.

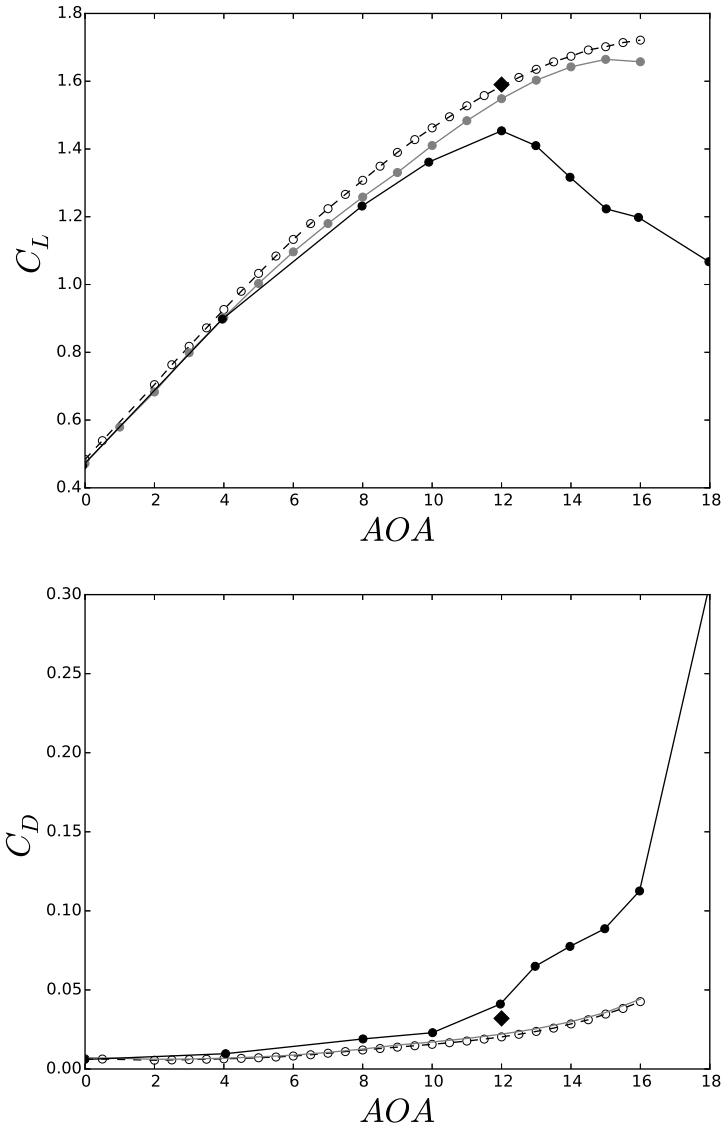


Figure 5.3: NACA4412 at $Re = 1.64 \times 10^6$: comparison of the lift and drag coefficients obtained with XFOIL (dashed black line with circles), RANS (gray line with circles) and wmLES (black square) to the experimental data from Wadcock [101] (solid black line with circles).

Figure 5.4 compares the chordwise pressure coefficient distributions obtained with XFOIL, RANS and wmLES to the experimental results. The same global behavior is captured by the four techniques. However, on the suction side, the wmLES is closer to the experiment in the region $0.05 \leq x/c \leq 0.6$, *i.e.* for about half of the chord length. The three numerical approaches then merge and there is a significant difference with the experiment over the last 20% of the chord. Experimentally, a pressure plateau is observed while, numerically, the pressure goes almost linearly to zero. This difference likely comes from a disagreement in the phenomenology of the trailing edge separation. Figure 5.4 provides more insights into this separation by also presenting the chordwise friction distribution obtained with the three numerical approaches. As XFOIL and RANS have $C_f \leq 0$ for $x/c \gtrsim 85\%$, they predict a separation close to the one observed by Wadcock [101]. For the wmLES, the C_f stays positive and there is no separation. Note also on this figure that the three estimates of C_f are close on the suction side. However, on the pressure side, the wmLES approach provides a friction that is about four times bigger than for the two other approaches.

Figure 5.5 then compares the experimental and computational velocity profiles. The extensive database from Wadcock [101] contains the velocity and fluctuations profiles in the three directions at three stations along the airfoil suction side and at two stations in the wake. However, as a first evaluation, only the values of the main component of the velocity are compared. For the three stations on the airfoil the wall tangential velocity is compared, whereas for the two wake stations, it is the velocity parallel to the wind tunnel wall surface as presented on Figure 5.5.

Figure 5.5 shows that the flow measured by Wadcock is attached in station 1. It then decelerates due to the adverse pressure gradient and obtains a slope $du/dy \simeq 0$ at station 2. At station 3, it is slightly separated as $u \leq 0$. At station 1, both RANS and wmLES match the experiment. At station 2, both RANS and wmLES show a deceleration but RANS is closer to the experiment. At station 3, the deceleration continues for both numerical approaches and RANS is again closer to the experiment. In the wake, for stations 4 and 5, the differences between the 3 approaches is maintained.

This comparison shows that the RANS captures the trailing edge separation better than the wmLES. This observed behavior constituted a strong indication that the wall model is not able to capture the effect of the APG. If this is the case, the use of a more elaborate wall model would permit to obtain a wmLES prediction closer to the experimental result.

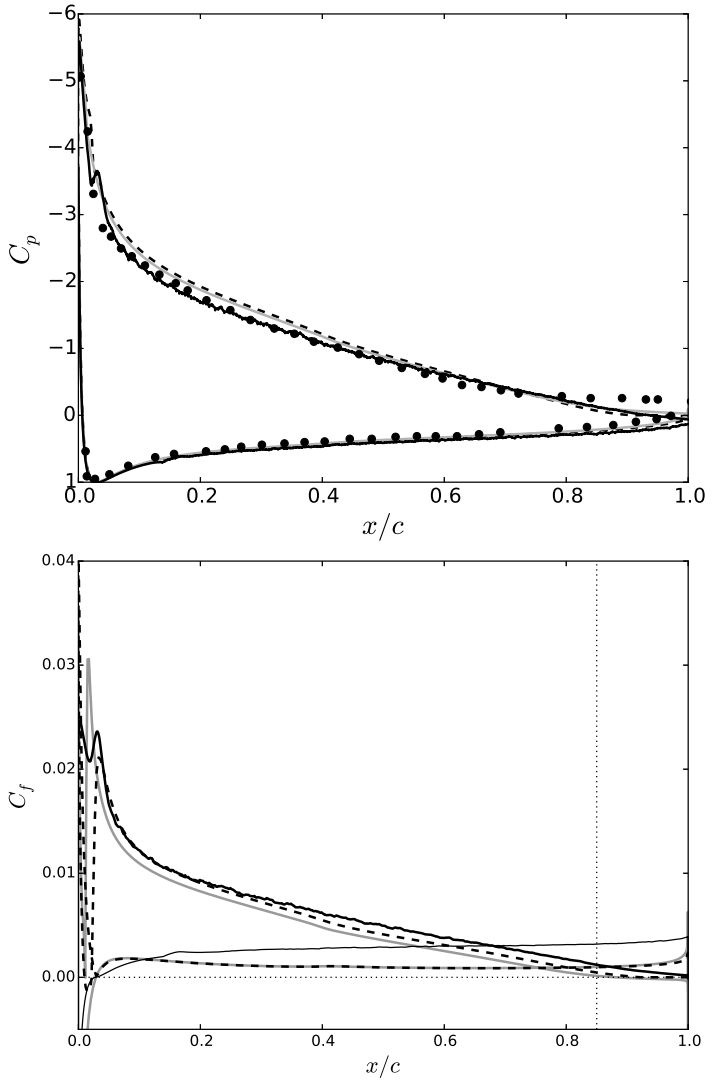


Figure 5.4: Comparison of the chordwise pressure (top) and friction (bottom) coefficients obtained at $\alpha = 12^{\circ}$ and $Re = 1.64 \times 10^6$ with XFOIL (black dashed line), RANS (gray line) and wmLES (black solid line) to the experimental results (black circles) from Wadcock [101]. On the bottom figure, the vertical dotted line represents the separation measured by Wadcock. The horizontal dotted line separates positive and negative C_f, *i.e.* attached and separated flows.

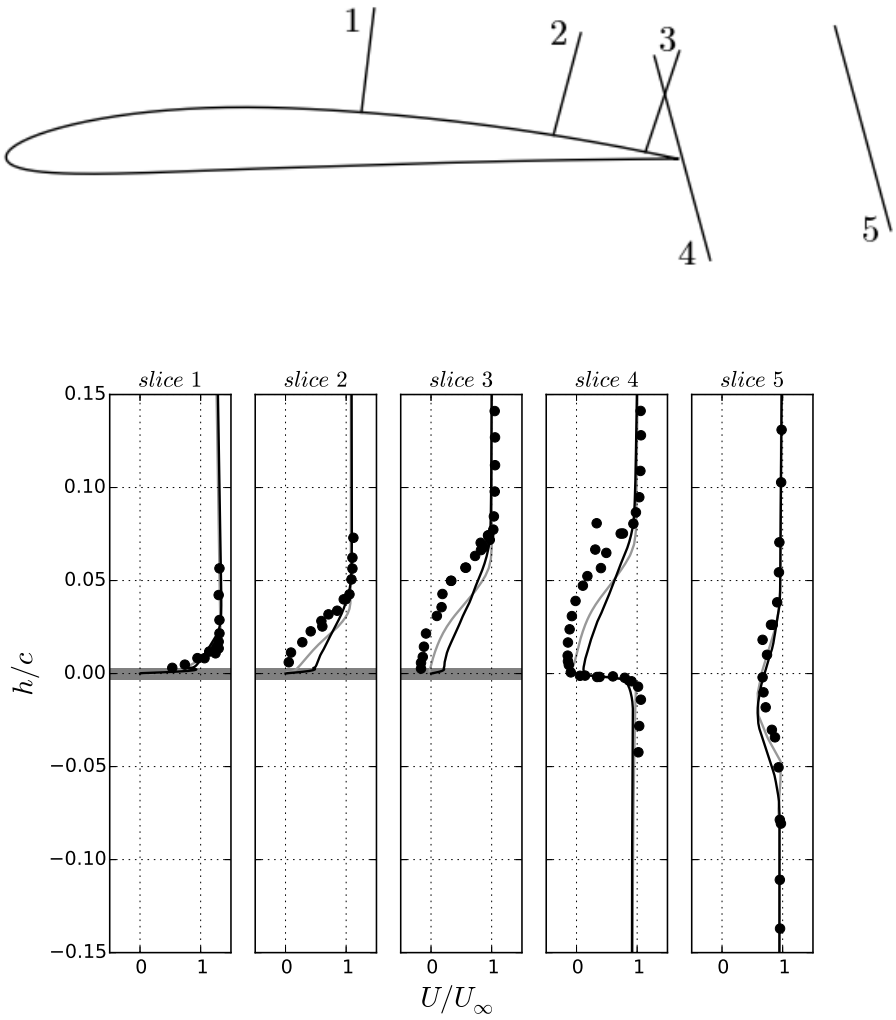


Figure 5.5: Comparison of the velocity profiles. A schematic of the measurement slices is given on the top with from left to right, 3 slices perpendicular to the airfoil suction surface at $x/c = 0.529, 0.815, 0.952$ and 2 slices perpendicular to the wind tunnel bottom wall at $x_t/c = 0.007, 0.282$. The mean tangential velocity profiles at these 5 locations are given on the bottom for RANS (gray line), wmLES (black line) and the experiment of Wadcock [101] (black circles). For the three first slices, the horizontal gray zone represents the thickness of the buffer element considered in wmLES.

5.2.3 Challenges for wmLES development

As described in Chapter 2, although Reichardt model is developed for equilibrium flows, it should also be applicable to APG as long as the boundary layer velocity profile features a log-layer region and the wall model input is before the end of that region. However, many authors suggest to use more elaborate expressions as the one from Shih [86] or more widely used the "Two-Layer Model" (TLM) of Balaras *et al.* [6] that couples LES to simplified RANS equations

$$\left(\frac{\partial^2 u^+}{\partial {y^+}^2} + \frac{\partial(-\overline{u'v'}^+)}{\partial y^+}\right) = \left\{p^+\right\} + \left[u^+\frac{\partial u^+}{\partial x^+} + v^+\frac{\partial u^+}{\partial y^+}\right]. \quad (5.1)$$

In its full form, the model is computationally more expensive since it requires the solution of these equations on an auxiliary, boundary fitted grid. It is therefore often simplified. The most frequent simplification neglects the convective terms [30], indicated by the square brackets. However, a recent review by Larsson *et al.* [48], states that the convective terms approximately balance the pressure gradient term (term within curly brackets), such that both should either be considered or neglected together.

The common approach in wmLES development consists in performing different wmLES, each with a different wall model, and to compare them *a posteriori*. However, as there exists many models, this approach requires to perform many wmLES. Considering that the "cheap" wmLES performed here requires already 500 CPU during a few days, testing *a posteriori* various models is not judicious and an *a priori* approach is chosen here.

Furthermore, even with a more advanced model, the wmLES might not reproduce perfectly the validation case. Three recent studies [11, 67, 20] attempted the validation of wmLES by simulating the flow over the NACA4412 airfoil. In all cases, as for us, the overall flow was captured but differences were observed with respect to the experimental reference. These differences could be due to an inability of the wall models to capture the APG. However, all authors put forward the difficulty, or even the impossibility, to exactly reproduce the experimental conditions. In particular, the trip wire is not reproduced considering the coarse near-wall grid used with wall models [67, 11, 20]. Furthermore, the study that obtains the best match with the experiment [67] is also the only one to model the effect of the wind tunnel blockage. Therefore, it is difficult to conclude on the origin of the differences between the experimental and numerical results and on the ability of the different wmLES approaches to capture the APG. However, whatever the actual origin of the observed differences, it is clear that the inherent difference between the experimental and the numerical setup leads to difficulties in developing and validating the wall model approaches. Therefore, the ideal wmLES validation case is a wall-resolved LES or DNS run under exactly the same conditions as the wmLES. The next section aims at performing this wrLES.

5.3 NACA4412 airfoil: wall-resolved LES

Based on the challenges observed in the previous section for the development of wmLES techniques, this section aims at performing a wrLES of the NACA4412 at $Re = 1.64 \times 10^6$ and $\alpha = 12^\circ$ in order to obtain an ideal validation case and to compare different widely used wall models *a priori*. The steps of the study consist of

- providing a numerical reference, which can be reproduced for the validation of wmLES or related approaches;
- extracting from this database the quantities used as wall model in- and outputs;
- using these quantities to assess the validity of various existing wall models.

Instead of comparing the different models *a posteriori* by analyzing the results of different wmLES computations, the models will be confronted here in an *a priori* manner on the basis of a wall-resolved LES. The focus of the comparison presented in this section is on evaluating the models' capacity to represent APG effects and, more specifically, on answering the following questions:

1. Can an analytical approach that assumes equilibrium match velocity profiles in APG boundary layers at high Reynolds number?
2. How does the use of Reichardt equilibrium law-of-the-wall compare to that of Werner and Wengle's model?
3. Does the use of the analytical model of Shih [86], which explicitly includes the pressure gradient, improve upon that of the equilibrium law ?
4. Can the more advanced and expensive "Two-Layer Model" [6] be simplified by removing the convective and/or the pressure gradient terms?

The work is organized as follows. Section 5.3.1 describes the computational setup. Section 5.3.2 compares the wrLES results to seven previous numerical and experimental studies. Section 5.3.3 uses the wrLES results to characterize a flow submitted to an APG. Finally, Section 5.3.4 compares the different wall models to address the questions raised above.

5.3.1 Numerical setup

The wrLES computation is performed at $\alpha = 12^\circ$ and $Re = 1.64 \times 10^6$ on a 2D mixed-element mesh, extruded in the spanwise direction on a narrow extent of about 1% of the chord. Contrarily to the previous computations performed in this thesis, the 2D grid consists in a C-type mesh rather than an O-type. The C-type mesh should improve the representation of the trailing edge flow. This improvement is made possible through a collaboration with A. Johnen and J.-F. Remacle from the GMSH meshing tool development team. As for the previous runs, the mesh consists of quadrangles in the boundary layer and triangles in the far-field as presented on Figure 5.6. The low resolution of the

mesh is deliberate: cubic polynomials ($p = 3$) indeed interpolate the solution within each cell. Starting from a statistically converged computation using $p = 2$, the computation is run over eight additional flow-through times ($ftt = c/u_\infty$) to evacuate the transient. Then time- and spanwise-averaged statistics are obtained during two additional flow-through times.

The obtained effective streamwise, wall-normal and spanwise resolutions are in agreement with Choi and Moin's guidelines [23], see Figure 5.7. Figure 5.8 illustrates the coarsening of the refinement in the wall-normal direction. It shows that the wall-normal mesh is constant through the chord and that the layers grow smoothly until $y/c \simeq 0.05$. After that point, the mesh is unstructured and has been coarsened rapidly to limit the required computational resources, see Figure 5.6. By comparing the extent of the wall-normal structured mesh to the boundary layer thickness measured in the experiment, it appears that the boundary layer is fully in the well-resolved mesh for a small portion of the chord close to the leading edge $x/c \leq 0.2$. Therefore, although the refinement is sufficient at the wall, it might be too coarse to capture the full boundary layer height for $x/c \geq 0.2$.

The use of the unstructured mesh makes possible to obtain a rapid increase of the element size and to reduce the grid cost, allowing to fix the far-field conditions at a distance of more than 10 chords. However, due to computational restrictions, the span extent corresponds to $\simeq 1\%$ of the chord only. The use of such a narrow span also leads to two-dimensional near-wake vortices, as can be observed in Figure 5.9. However, this wrLES is considered sufficient for the purpose of developing and partially validating wmLES.

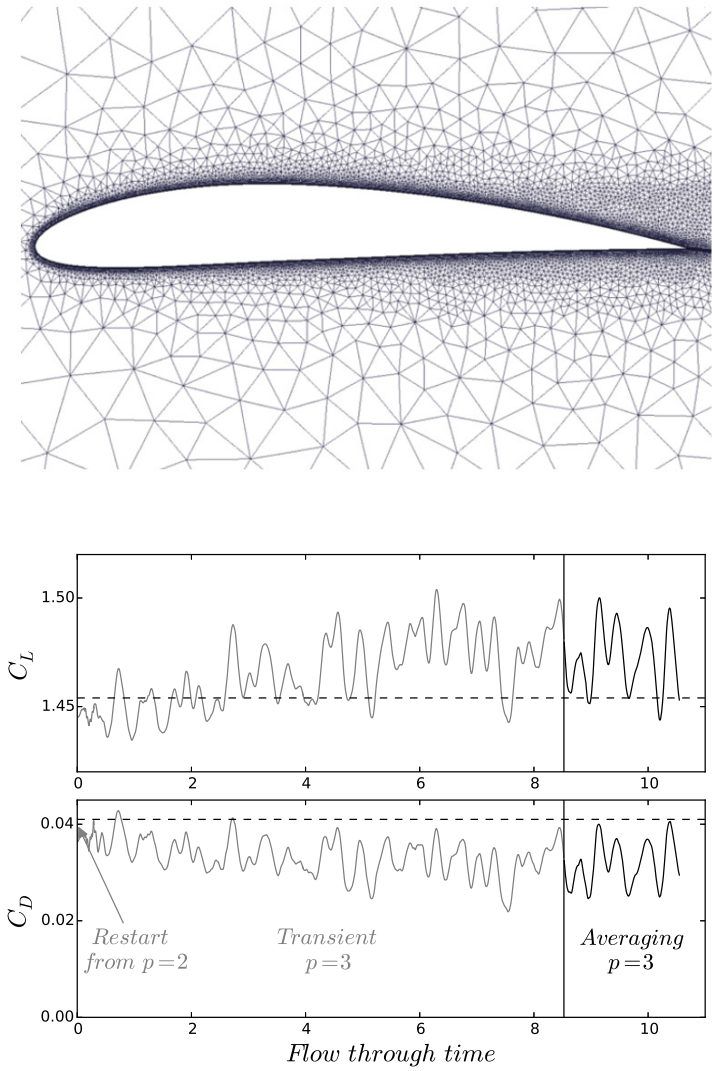


Figure 5.6: A view of the mesh is given on the top with quadrangles in the boundary layer and triangles in the far field. Timewise lift and drag coefficient evolutions are given on the bottom. The dash line corresponds to the lift and drag values measured in the experiment of Wadcock [101].

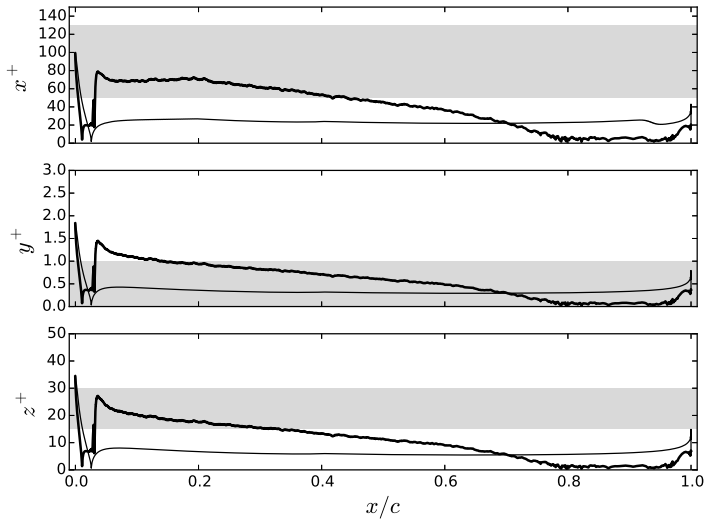


Figure 5.7: Chordwise wall-refinement in the streamwise (x), normal (y) and spanwise (z) directions. The wrLES results (black) are compared to Choi and Moin guidelines [23] (gray area). The suction side data are highlighted by using a thicker line.

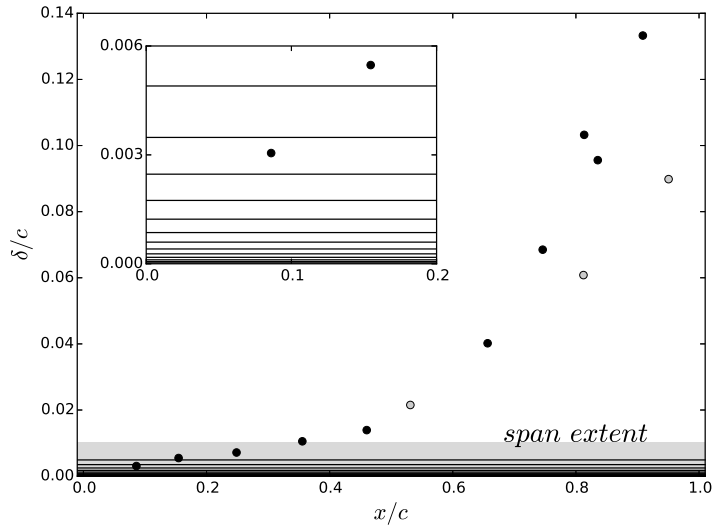


Figure 5.8: Chordwise boundary layer thickness evolution measured by Wadcock [101] with two different techniques (black and gray circles) compared to the layers used as wall-normal structured grid along the chord (black line) and the span extent (gray area). The small inset provides a zoom on the wall-normal grid.

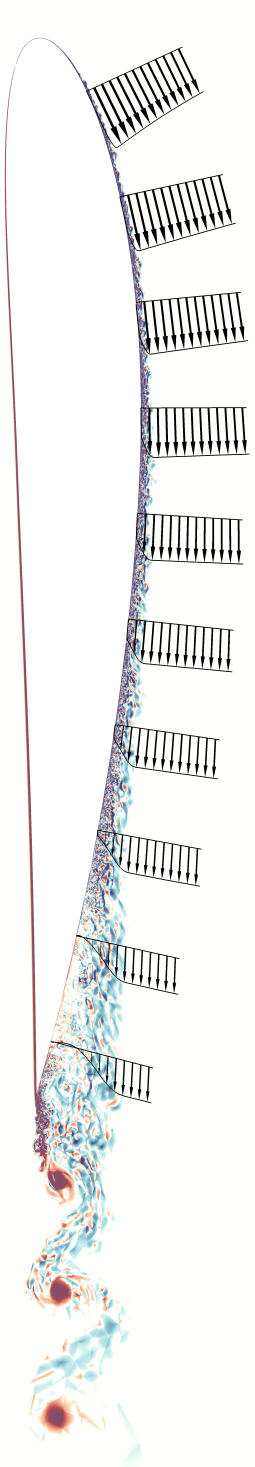


Figure 5.9: Mean velocity profiles and instantaneous spanwise vorticity over the NACA4412 airfoil at $\alpha = 12^{\circ}$ and $Re = 1.64 \times 10^{6}$.

5.3.2 Comparison to previous studies

The wrLES results are compared to two experiments [101, 39], four wrLES [43, 45, 44, 80] and one wall-modeled LES [67]. The first aim of this comparison is to verify the quality of the proposed new computation. The second aim is to discuss the impact of the different configurations.

All studies used in the comparison have been performed at $Re = 1.64 \times 10^6$ and $\alpha = 12.0°$. However, the computational configurations differ in some aspects that are summarized in Table 5.1. In that table, the configurations are differentiated based on three important setups: the forcing of the transition, the modeling of the wind tunnel blockage and the span extent. Note that, as the flow statistics are averaged over the time and the span, it would be interesting to add the number of flow-through times considered in the statistics. However, this information is rarely provided, or it is not complete. Kaltenbach and Choi [45] mention the use of $2\ ftt$ for the statistics, but do not precise how is the calculation initialized and how many ftt are needed to evacuate the transient. Schmidt *et al.* [80] specify only an entire computation time of $8\ ftt$. Park and Moin [67] mention the use of $12\ ftt$ to evacuate the transient, followed by $4\ ftt$ for the statistics. Furthermore, in an equivalent study performed on the DU96 airfoil ($Re = 1.5 \times 10^6$, $\alpha = 10.3°$ and $s/c = 12\%$), Venugopal *et al.* [96] initialize the calculation based on a 2D computation; they then use $2.6\ ftt$ to evacuate the transient and $1\ ftt$ for the statistics.

The most important flow features are to be found along the suction side. Close to the leading edge, the thin laminar boundary layer separates and then reattaches, creating a laminar separation bubble (LSB). Further downstream, the now turbulent boundary layer grows under the effect of the APG and finally separates at about 80% of the chord. The chordwise pressure and friction coefficients as well as the velocity profiles are compared hereafter.

Table 5.1: Summary of the different setups considered in the comparison of Section 5.3.2.

	Type	Forced transition	Tunnel walls	Span extent as % chord
Wadcock [101]	exp.	yes	yes	280%
Hasting and Williams [39]	exp.	yes	yes	400%
Kaltenbach and Choi [45]	wrLES	yes	no	$2.5 - 5\%$
Jansen [43]	wrLES	no	no	$2.5 - 5\%$
Jansen [44]	wrLES	yes	yes	$2.5 - 5\%$
Schmidt *et al.* [80]	wrLES	yes	no	5%
Park and Moin [67]	wmLES	no	yes	72%
Current work	wrLES	no	no	1%

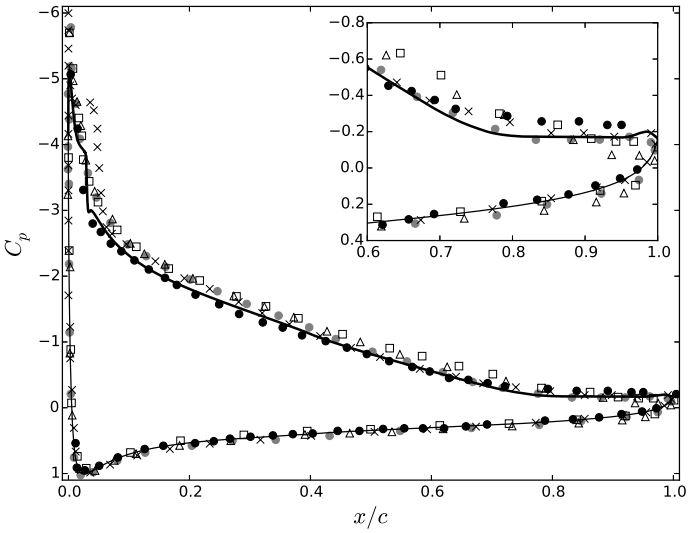


Figure 5.10: Chordwise pressure coefficient evolution. Different wmLES and wrLES are compared to Wadcock's experiment (black circles) [101] and to the present wrLES (solid black line): Kaltenbach and Choi (squares) [45], Jansen (triangles) [43], Schmidt *et al.* (crosses) [80] and Park and Moin (gray circles) [67]. For Argo wrLES, the suction side data are highlighted by using a thicker line. Except for Argo data, all wm- and wrLES data have been digitized manually based on the reference papers.

Pressure and friction coefficients Figure 5.10 presents the chordwise pressure coefficient obtained by the different studies. As the experimental pressure curve obtained by Hasting and Williams [39] is very similar to the one obtained by Wadcock [101], only the latter is shown in this figure. From this comparison, it appears that the present simulation is within the range of the previous studies and in good agreement with the experimental reference.

A closer look at the last 20% of the chord shows that the pressure plateau observed in the experiment is rarely captured numerically. For instance Jansen's wrLES from 1995 does not present a plateau [43]. In 1996, Jansen showed that considering the tunnel blockage helped in obtaining a plateau [44]. This seems to be confirmed by the wmLES from Park and Moin [67].

However, although the wrLES performed here does not consider the blockage, it captures the plateau.

Jansen [43] compared two span extents of $2.5\%c$ and $5\%c$ and observed that the narrow span artificially leads to a pressure plateau closer to the experiment. However, as his comparison was made using two different grid refinements, he added that no strong conclusion can be drawn. The same year, Kaltenbach and Choi [45] compared also the span extents of $2.5\%c$ and $5\%c$

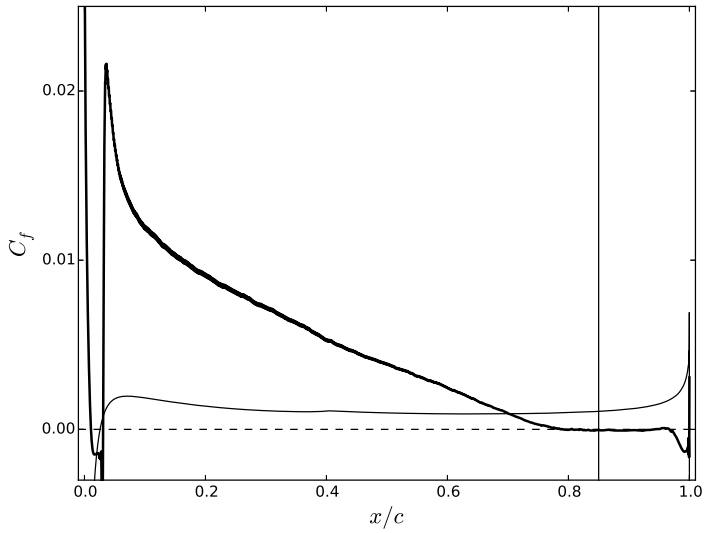


Figure 5.11: Chordwise friction coefficient evolution. The present wrLES friction coefficient (black curve) is compared to the separation point measured by Wadcock (vertical black line). The suction side data are highlighted by using a thicker line.

while keeping the refinement constant and concluded that the span extent was not impacting the C_p curve. Therefore, the impact of the span is not clear. However, even if this new wrLES is artificially close to the experiment only due to its narrow span extent, the goal of the present computation is to be reproducible using a wmLES approach, and not to match the experimental data.

Further interesting information can be inferred from the evolution of the friction coefficient along the airfoil, presented on Figure 5.11. One notices that the wrLES results contain two separated regions. The first separation region, corresponding to the laminar separation bubble, starts at $x/c = 0.01$ and reattaches at $x/c = 0.03$. After $x/c = 0.76$, a relatively large zone of near zero C_f is observed, before an actual separation (*i.e.* with C_f clearly negative) that occurs at about $x/c = 0.97$. Although it might be induced by the narrow span extent, such a large zone of near zero C_f is interesting as it is rarely seen in the literature.

Transition induced by the laminar separation bubble In the experiment, the laminar-turbulent transition is forced by a boundary layer trip on both suction and pressure side. Given the modeling ambiguity of such a device, the tripping is not considered in the present computation. Nevertheless, transition occurs on the suction side almost exactly at the same position as in the experiment.

In all the studies in which transition is not forced, the authors observe an LSB near the leading edge. However, only Jansen characterizes it by providing the velocity profiles in that region [43]. Furthermore, Hasting and William [39] mentioned that they did a few tests without tripping and observed, at an angle near stall, an LSB spanning between $x/c = 0.01$ and $x/c = 0.017$. Figure 5.12 and Figure 5.13 provide a visualization of the LSB as well as a comparison of the tangential velocity profile in the LSB region. For this figure and for the rest of this work, the tangential and normal directions are defined separately at each chordwise location.

Although Jansen used the terms "coarse" and "fine" to differentiate between his two meshes, they are called here "a" and "b" because the "fine" mesh has been run on a twice narrower span of 2.5%; so the origin of the small differences is not clear. Therefore, the two cases are seen here only as two different computations.

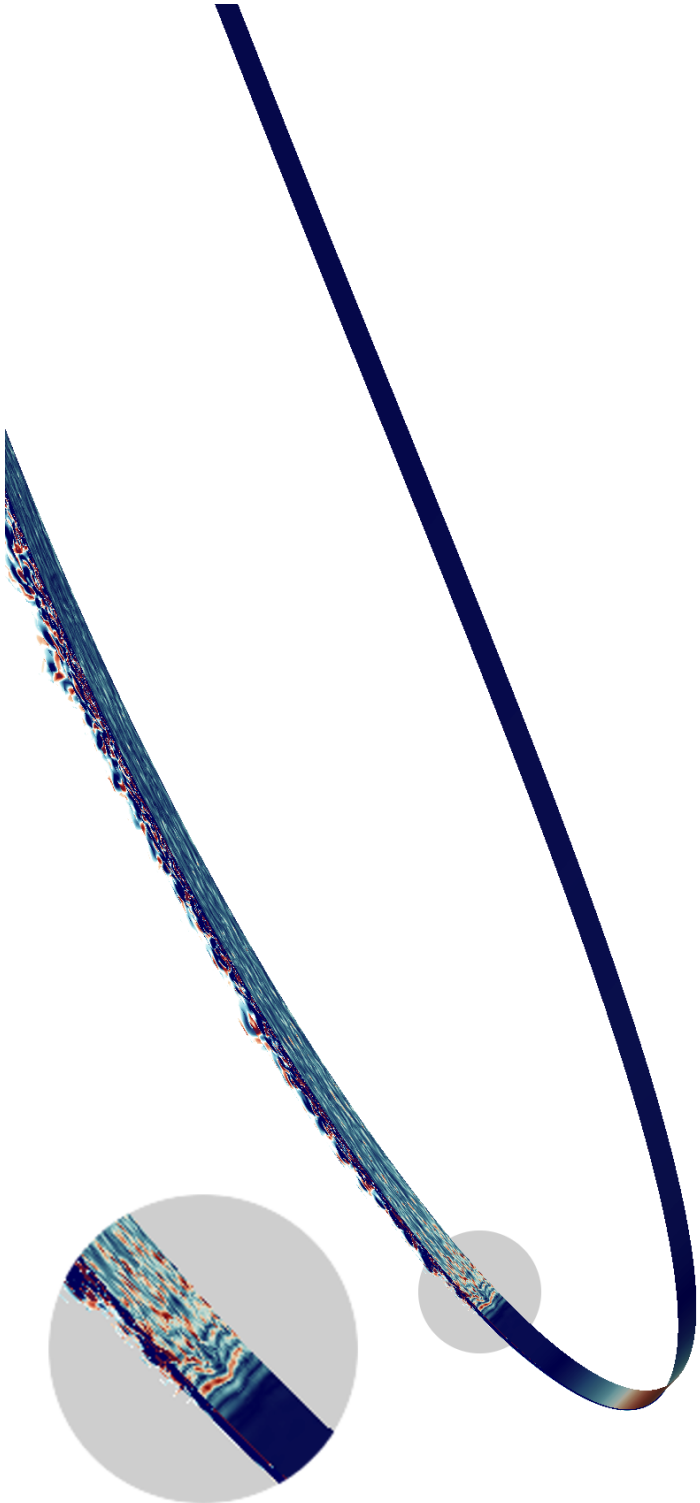


Figure 5.12: Characterization of the laminar separation bubble. View of the instantaneous shear on the airfoil surface and of the instantaneous spanwise vorticity.

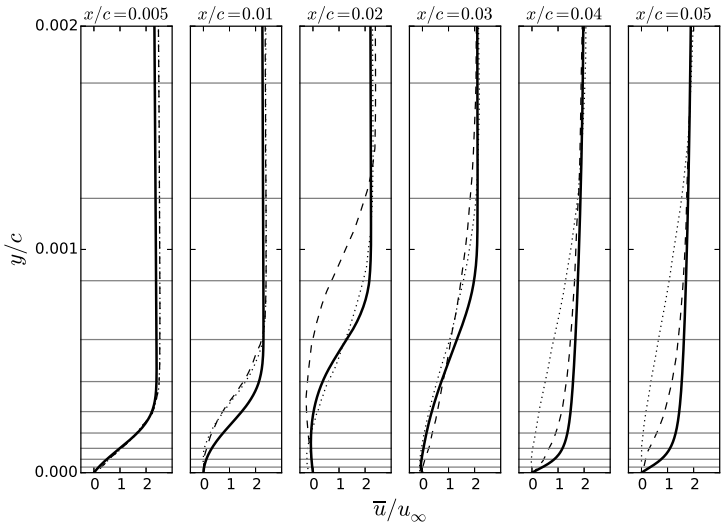


Figure 5.13: Comparison of the tangential velocity profiles along the chord in the LSB region. The results (solid line) are compared to the two previous wrLES from [43], on mesh a (dotted) and mesh b (dashed). The horizontal gray lines represent the wall normal grid refinement.

The comparison shows that all simulations present an LSB in the region $0.01 \leq x/c \leq 0.05$ and that the maximum thickness observed is $\simeq c/1000$. At $x/c = 0.02$, the LSB thickness obtained by the mesh b is twice bigger than the one obtained by the two other wrLES. However, already at $x/c = 0.04$, the velocity obtained with the mesh b is almost identical to that from the current wrLES. As the differences between the three wrLES are small in absolute value, it is concluded from this comparison that the three wrLES have globally the same LSB.

Velocity profiles Figure 5.14 compares the obtained tangential velocity to the previous results. The six positions used in this comparison are mostly placed on the second half of the chord. Furthermore, more reference data are provided for the two positions close to the trailing edge. This comes from the fact that the focus of the studies was the capture of the separation. Again, the current wrLES simulation is in the range of the previous studies and appears to agree even better with the experimental results. This allows us to trust the computations sufficiently to use them to complement the experimental data. The wrLES results are thus used in the next section to characterize the flow under an APG.

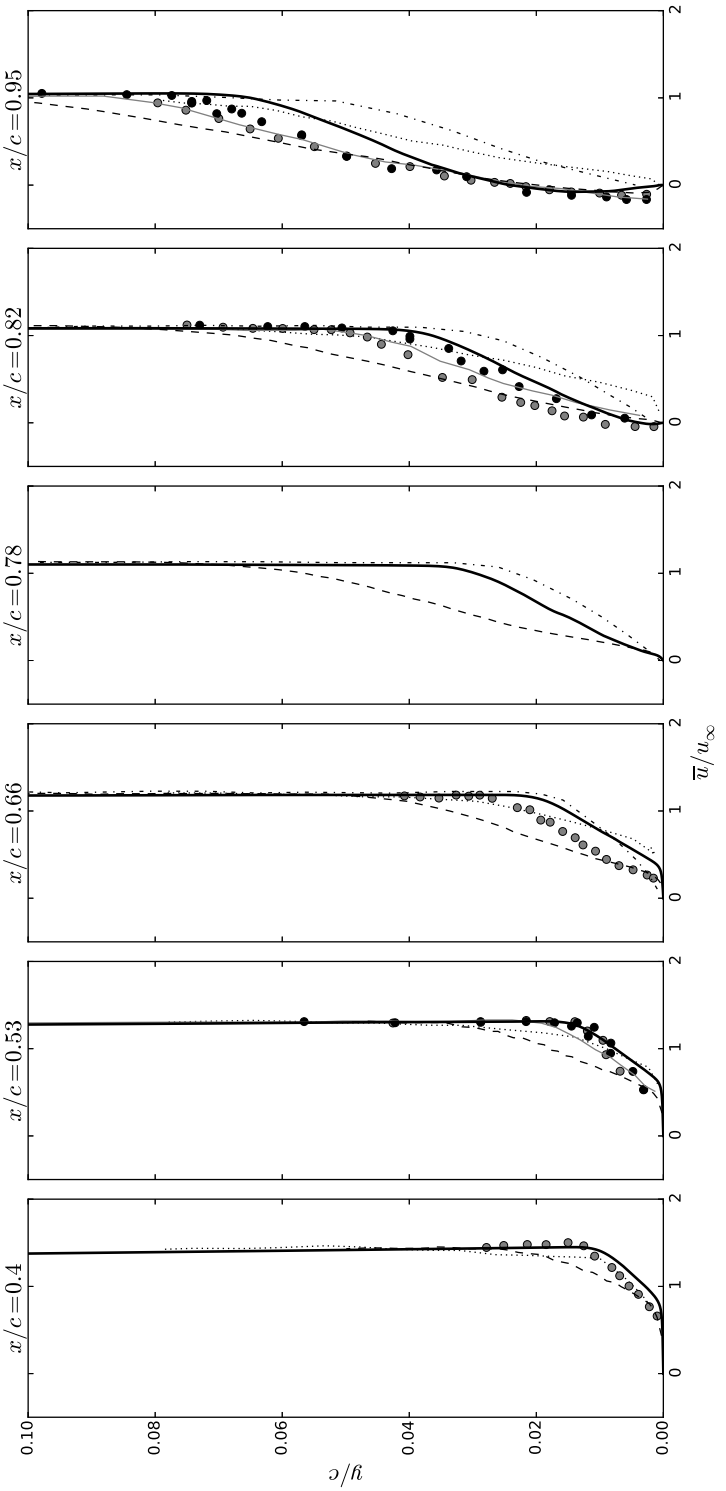


Figure 5.14: Comparison of the tangential velocity profiles. The wrLES results are represented by black lines: present study (solid), Schmidt *et al.* [80] (dashed), Kaltenbach and Choi [45] (dotted), and Jansen [44] (dashed-dotted). The wmLES from Park and Moin [67] is represented by solid gray lines. Experimental results are represented by circles: Hasting and Williams [39] (gray) and Wadcock [101] (black).

5.3.3 Characterization of the boundary layer subject to an APG

This section presents the evolution of the boundary layer thickness, the velocity and the Reynolds stresses on the suction side of the airfoil with a focus on the region subject to the APG, before the separation. Figure 5.15 shows the evolution of the tangential velocity along the chord at positions x/c ranging from 0.05 to 0.95 with steps of 0.05. On the global view, the deceleration of the flow is observed with a maximum edge velocity $u_e/u_\infty \simeq 2$ at $x/c = 0.05$ that reduces to $u_e/u_\infty \simeq 1$ after $x/c \geq 0.7$. The growth of the boundary layer thickness is also observed, ranging from $\delta/c \simeq 0.005$ at $x/c = 0.05$ to $\delta/c \simeq 0.03$ at $x/c = 0.7$.

The negative slope obtained for $x/c \geq 0.85$ indicates that the flow is separated in that region. However, the friction coefficient presented previously in Figure 5.11 shows a large region with essentially zero friction coefficient ranging within $0.77 \leq x/c \leq 0.97$. Therefore, a close-up is also provided to visualize the slopes at the wall. This confirms that, for all profiles with $0.80 \leq x/c \leq 0.95$, the slope, and thus the friction, is negligible.

The non-separated velocity profiles of Figure 5.15 are also presented in Figure 5.16 in wall units and logarithmic scale. It appears that all curves collapse in the viscous sublayer and in a part of the logarithmic region ($y^+ \leq 100$ for the least favorable cases close to the separation and $y^+ \leq 400$ for $x/c \leq 0.65$), to separate in the wake region.

Figure 5.17 presents the evolution of the boundary layer thickness δ, the displacement thickness δ^*, the momentum thickness θ and the pressure gradient term. The three characteristic thicknesses are compared to the measurements of Wadcock [101]. It appears that, although the span extent is $s/c = 0.01$, the computed boundary layer evolution is similar to the experimental one up to $x/c \simeq 0.5$ where $\delta/c \simeq 0.015$. After that point, the evolution remains qualitatively similar, although it is quantitatively different. It also appears that the computed displacement and momentum thicknesses are similar to the experimental one up to $x/c \simeq 0.7$. This is quite remarkable for such a short span wrLES and deserves to be noted.

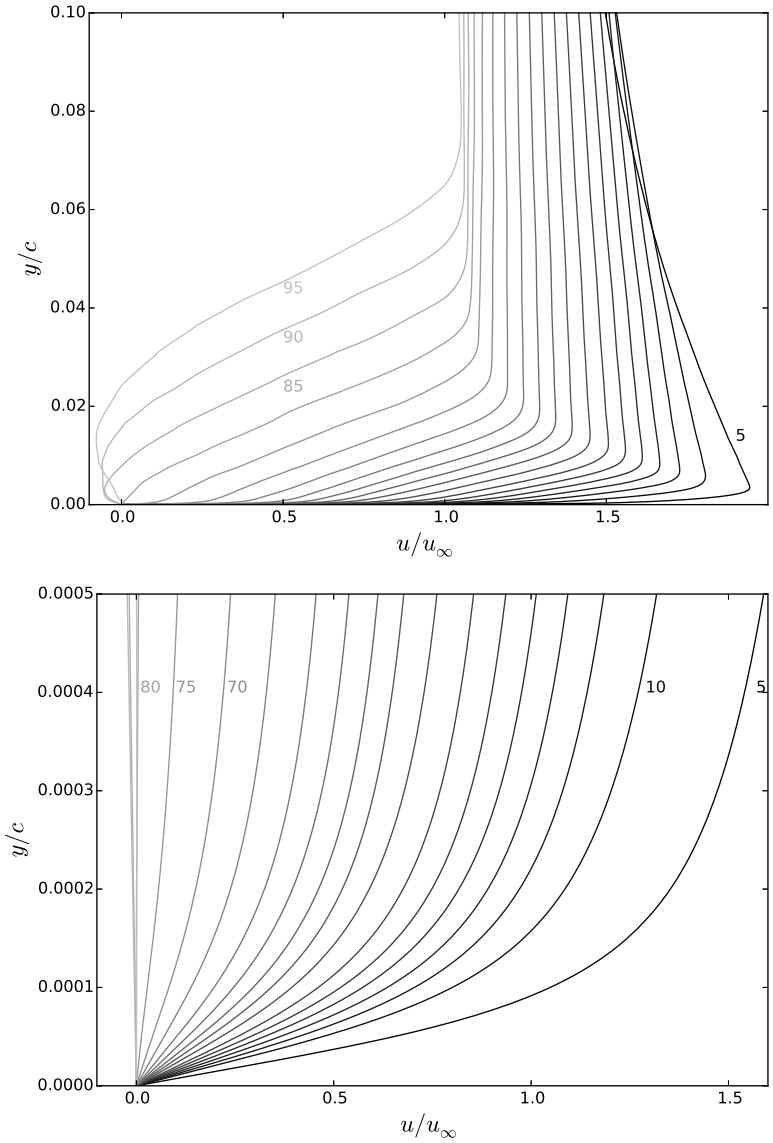


Figure 5.15: Tangential velocity profile evolutions along the chord. The profiles are given at positions x/c ranging from 0.05 to 0.95 with steps of 0.05 and are colored from black to light gray. A global view is given at the top. A close-up of the near-wall region is given at the bottom.

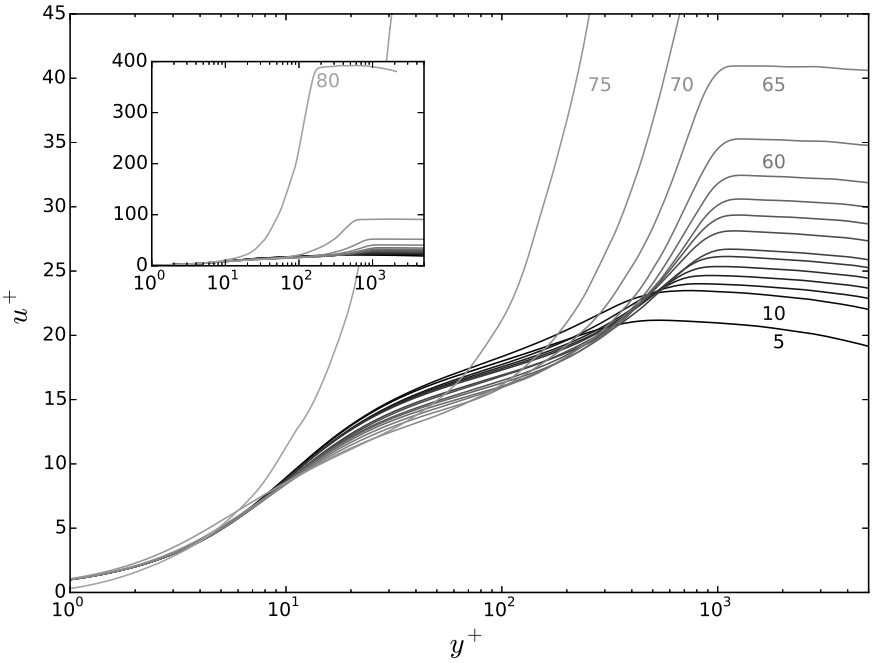


Figure 5.16: Tangential velocity profile evolutions along the chord in wall units and logarithmic scale. The profiles are given at positions x/c ranging from 0.05 to 0.80 with steps of 0.05 and are colored from black to light gray. The small figure presents the global view. The main figure zooms in near the wall.

In Figure 5.17, the pressure gradient term is expressed using both its value in wall units p^+ as well as the Clauser parameter $\beta = \delta^* \frac{dp/dx}{\tau_w}$. As these two go to the infinity at the separation, they are presented up to $x/c = 0.75$, where $p^+ \simeq 0.4$ and $\beta \simeq 100$. Vinuesa *et al.* [99] studied the NACA4412 airfoil by DNS at a lower angle of attack and a lower Reynolds number ($Re = 4 \times 10^5$ and $\alpha = 5°$). They studied the chordwise evolution of β and obtained an evolution similar to our result with a maximum value $\beta = 87$. In their case, this maximum is obtained close to the trailing edge, at $x/c = 0.98$, hence indicating that no separation occurred. Vinuesa *et al.* observed a strong increase of the Reynolds stresses and the apparition of a second peak in the streamwise fluctuation profile. Figure 5.18 performs the same evaluation as in Vinuesa *et al.* 's work and a similar behavior is observed. Note that, for the sections where $y^+ \geq 100$, some oscillations appear, and they are bigger for large x/c. These are due to the fact that the mesh is too coarse in that region, as discussed in Section 5.3.1.

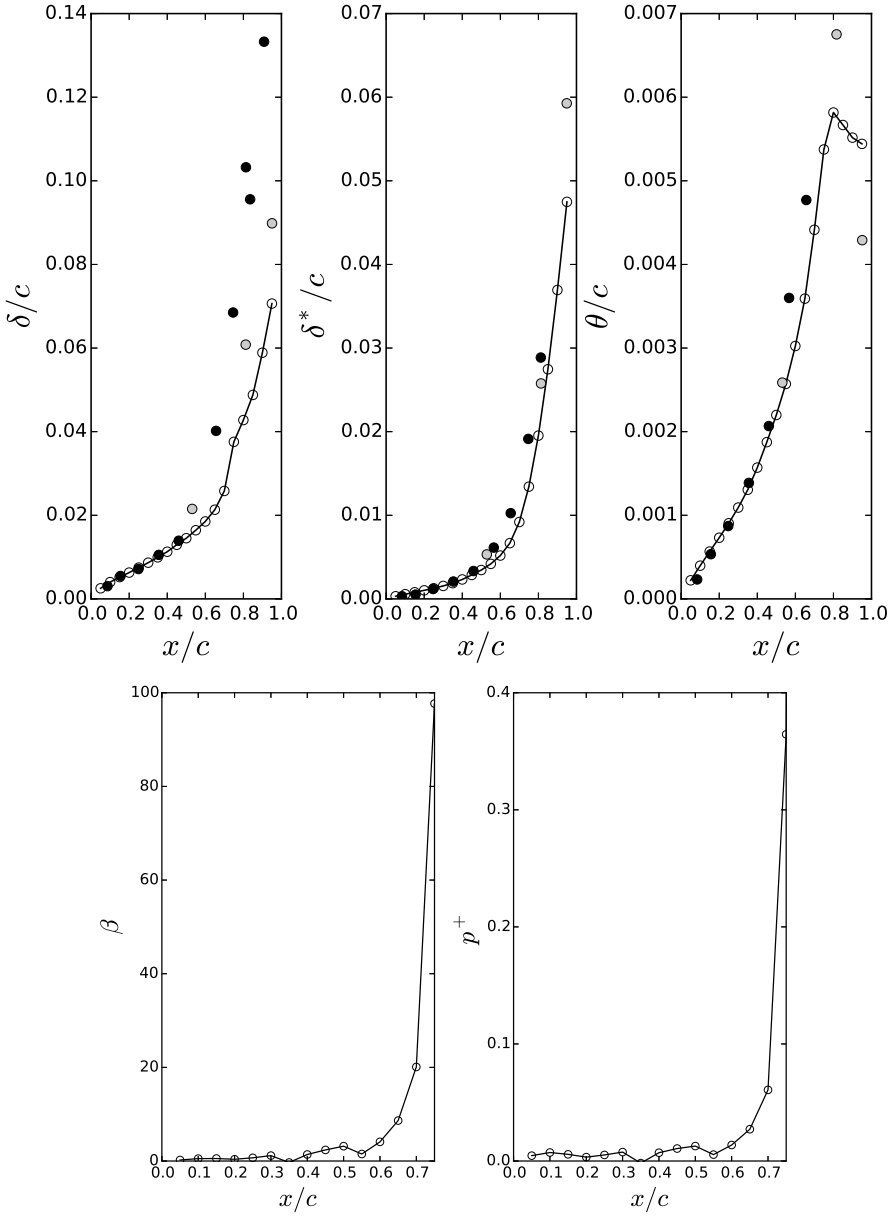


Figure 5.17: Chordwise evolution of the boundary layer parameters. Boundary layer thickness (left), displacement thickness (center) and momentum thickness (right) are given at the top. The experimental results obtained by Wadcock [101] with two different measurement techniques are also provided for comparison (black and gray circles). Clauser pressure gradient parameter (left) and p^+ (right) are given at the bottom.

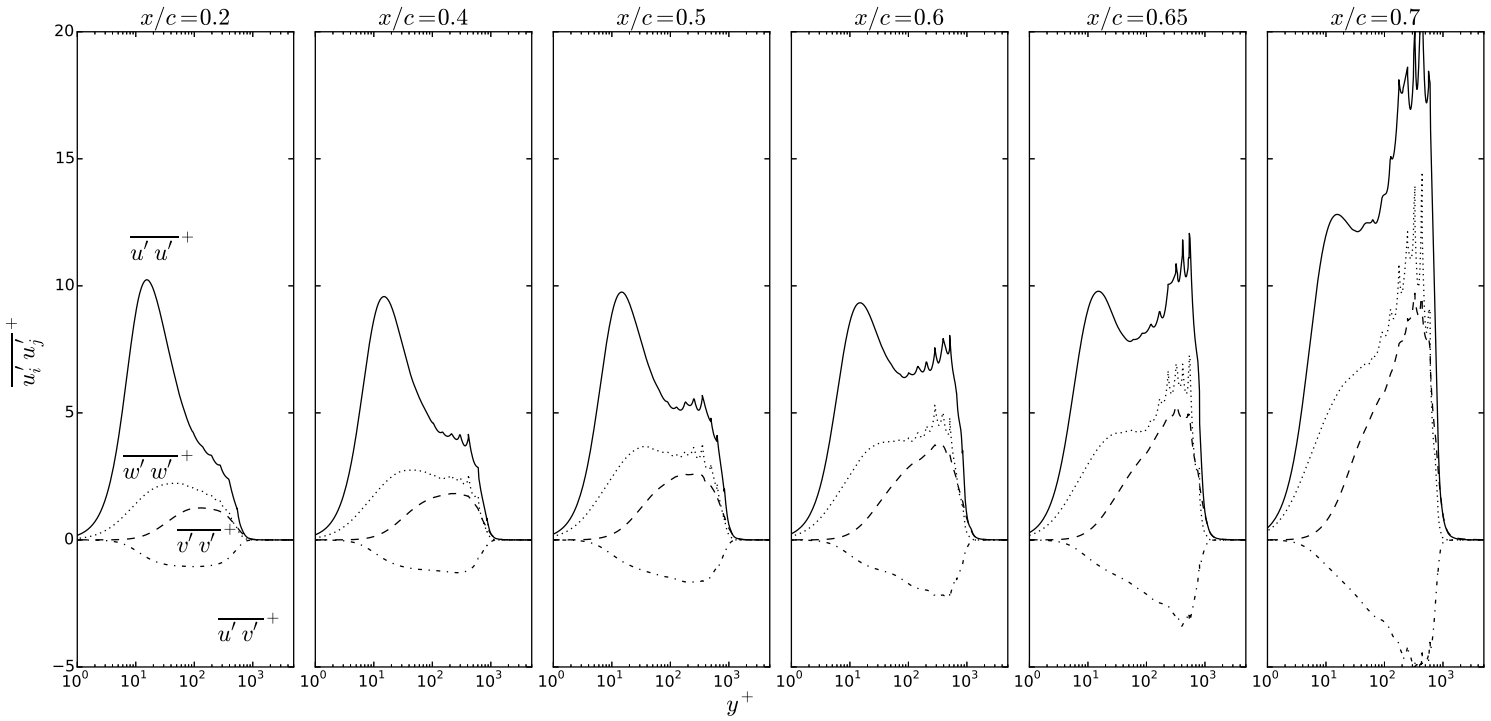


Figure 5.18: Reynolds stresses along the suction side of the airfoil for different chordwise positions. All subfigures presents from top to bottom, the streamwise $\overline{u'u'}$ (solid), spanwise $\overline{w'w'}$ (dotted), normal $\overline{v'v'}$ (dashed) velocity fluctuations and, in negative, the Reynolds shear stresses $\overline{u'v'}$ (dash-dotted).

5.3.4 Comparison with different wall model estimates

A typical approach for comparing different wall models consists in performing multiple wmLES. An alternative approach, used in the current study, evaluates the models (Reichardt Eq. (2.16), Werner and Wengle Eq. (2.20), Shih Eq. (2.22) and TLM), in an *a priori* manner using the time-averaged wrLES data. The procedure is the following:

1. the wall model inputs $(u(y_{wm}), dp/dx)$ are interpolated in the wrLES results;
2. the wall shear stress is computed following the model;
3. the wall model is assessed by comparing the predicted shear stresses and corresponding velocity profiles to the wrLES results.

This analysis is undertaken for three different positions along the chord and before the separation region, namely $x/c = 0.2, 0.5, 0.7$, and for five different wall model input positions, namely $y_{wm}/c = 0.1, 3, 6, 9, 11 \times 10^{-3}$. For the TLM model, two laws are used. The first one, referred to as TLMdp neglects the convective terms. The second one, referred to as TLMequi neglects both convective and pressure gradient terms. In both cases, the following relation is used

$$-\overline{u'v'}^{+} = \frac{\nu_t}{\nu}\frac{\partial u^+}{\partial y^+}, \tag{5.2}$$

and the turbulent viscosity is approximated by $\nu_t/\nu = \kappa y^+(1 - \exp -y^+/19)^2$ as used in [102, 22].

Figure 5.19 compares the velocity profiles estimated by the wall models to the wrLES database at the three chordwise locations. As Werner and Wengle's model provides the shear stress directly, without passing by an estimate of the velocity profile, only the four other models are compared here. For each chordwise location and wall model, a sub-figure shows the velocity profiles obtained for the five input locations. If, for one input location, the model did not converge, no profile is given. One sees that Reichardt and Shih's models always converged, but that problems occurred for the two TLM simplifications.

For all models, a Newton iteration is used. A more advanced algorithm could permit to obtain a better convergence of the models. However, this constitutes an interesting example of the complexity added by the models that are not based on simple analytic relations. Each subfigure also provides the wall distance in y/c and y^+ defined based on the wrLES wall shear stress. Recall that the wall model input positions are at constant y/c for the three chordwise locations and not at constant y^+. This choice is deliberate, as the common meshing practice typically uses a constant wall-normal grid size along the chord.

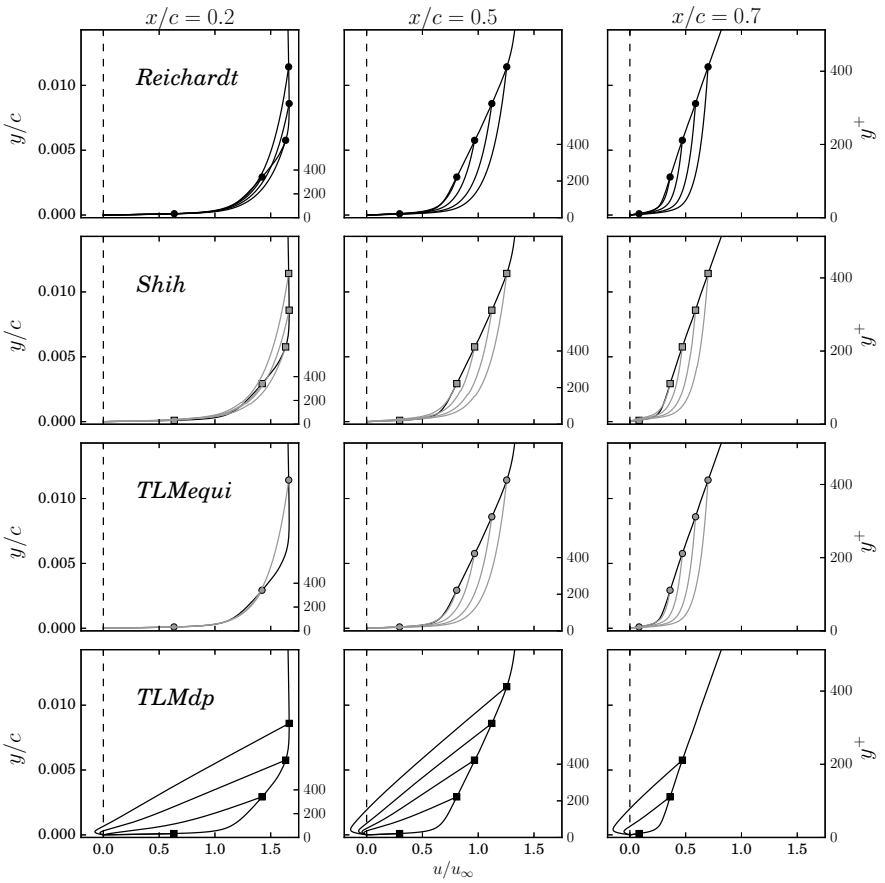


Figure 5.19: Comparison in the physical scale of the velocity profiles estimated by the wall models to the wrLES data (solid black line) at three different chordwise locations. Four models are compared with from top to bottom Reichardt, Shih, TLMequi and TLMdp. The markers show the position of the wall model input. Wall models that assume an equilibrium state are marked by circles with Reichardt (black) and TLMequi (gray). Wall models that add the contribution of the pressure gradient are marked by squares with Shih (gray) and TLMdp (black).

Figure 5.19 shows that the TLM variant that neglects both the convective and the pressure gradient terms (TLMequi) matches the wrLES reference better than the alleged more advanced variant (TLMdp) that neglects only the convective terms. Already at $x/c = 0.2$, the TLMdp estimates that the flow separates. This model thus appears to overestimate the impact of the APG. On this figure, Reichardt, Shih and TLMequi models are hardly distinguishable. Therefore, Figure 5.20 compares the three models in wall units and in logarithmic scale. As Reichardt and TLMequi's laws are defined as a relation be-

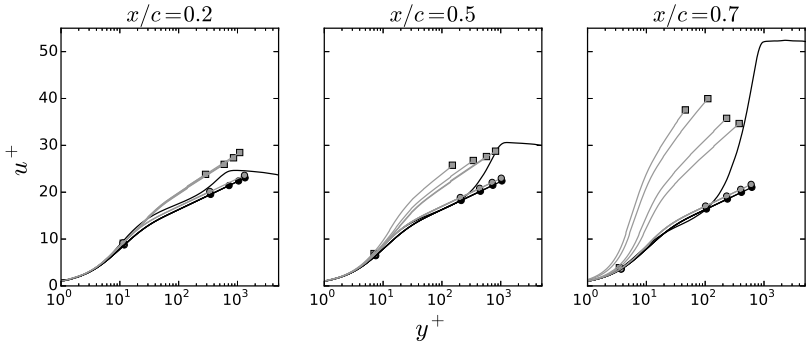


Figure 5.20: Comparison in wall units and logarithmic scale of the velocity profiles estimated by three wall models to the wrLES data (solid black line) at three different chordwise locations. The markers show the position of the wall model input. Wall models that assume an equilibrium state are marked by circles with Reichardt (black) and TLMequi (gray). Shih's model that adds the contribution of the pressure gradient is marked by gray squares.

tween u^+ and y^+ only, the curves at the three chordwise locations are similar. As Shih's law takes also p^+ into account, the curve deviates from Reichardt's curve for increasing p^+ and x/c. It appears that Reichardt and TLMequi's laws provide a good estimate as long as the input position is placed in the log region. In the most restrictive case, that is at $x/c = 0.7$, the log region stops at $y^+ \simeq 100$. Thus, one can expect Reichardt and TLMequi's models to be correct as long as the input $y^+_{wm} \leq 100$. Again, the alleged more advanced model, that is here Shih's law, appears to be further from the wrLES. Shih's law does not produce a common log region, as if the APG impact is overestimated or as if the model is made to capture a lower Reynolds number flow. Shih's model therefore appears not adapted to the flow physics concerned here.

Although it is interesting to compare the velocity profiles obtained with the different models, the only critical output of the wall model is the wall shear stress. Figure 5.21 compares the shear velocity $u_\tau(wm)$ obtained with the five models to the wrLES shear velocity u_τ. It appears that Reichardt, Werner and Wengle and TLMequi models, namely the models assuming an equilibrium flow, provide results that are very close to each other. At $x/c = 0.2$ their error is smaller than 20% for the five input positions. At $x/c = 0.5$, the error stays low but it increases slightly for the highest input location. At $x/c = 0.7$, the error is slightly higher for the two highest input locations where $y^+ \geq 200$.

This confirms the observations from Section 2.1.4: a model based on the law-of-the-wall can be used to model a flow subjected to an APG as long as the input position stays below the end of the log region. Here, the most restrictive case in term of y^+ is at $x/c = 0.7$ where the purely log region ends at $y^+ \simeq 100$. This corresponds to $y/c \simeq 0.003$, which is already more than 100 times larger

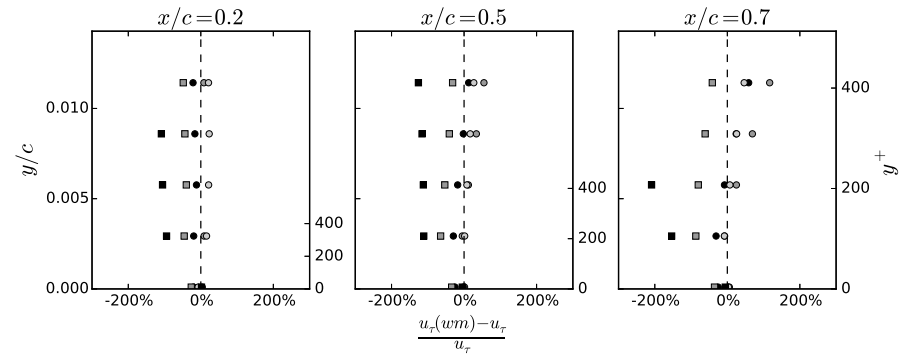


Figure 5.21: Comparison of the shear stress estimated by the wall models to the wrLES data. Wall models that assume an equilibrium state are marked by circles with Reichardt (black), Werner and Wengle (light gray) and TLMequi (dark gray). Wall models that add the contribution of the pressure gradient are marked by squares with Shih (gray) and TLMdp (black).

than the current wrLES wall-normal mesh. It also appears in Figure 5.21 that the two models that solely consider the pressure gradient (Shih and TLMdp) overestimate the impact of the APG and underestimate the shear. Their error is, except at $x/c = 0.7$ and at the highest y_{wm}, always larger than for the equilibrium models.

Figure 5.22 presents a balance of the TLM terms at six positions along the chord between $x/c = 0.2$ and $x/c = 0.7$. Although the two terms that compose the left hand side term of the TLM equation ($\frac{\partial^2 u^+}{\partial y^{+2}}$ and $\frac{\partial(-\overline{u'v'}^+)}{\partial y^+}$) stay of the same order of magnitude at the different chordwise locations, both the pressure gradient and the convective terms increase largely. At all the chordwise locations, the pressure gradient and the convective terms essentially are of the same order of magnitude. Hence, if the convective terms are neglected in the TLM, the pressure gradient term should be neglected as well. Note that, as for Figure 5.18, the oscillations that appear on this figure are due to the fact that the mesh is slightly too coarse in that region, as discussed in Section 5.3.1.

If one wants to keep the pressure gradient term but does not want to pay for the convective term calculation, a possible solution is to make a hypothesis about the behavior of the convective terms between the wall and the wall model input location. One interesting option suggested by Berger and Aftosmis [8] is to use the value of the convective terms at the input location y_{wm} and to assume that they grow proportionally to the tangential velocity. Examining the different terms that compose the convective terms in Figure 5.23, another option could be to assume a linear increase of the normal velocity and a constant streamwise velocity gradient. These two options should be tested in a future work.

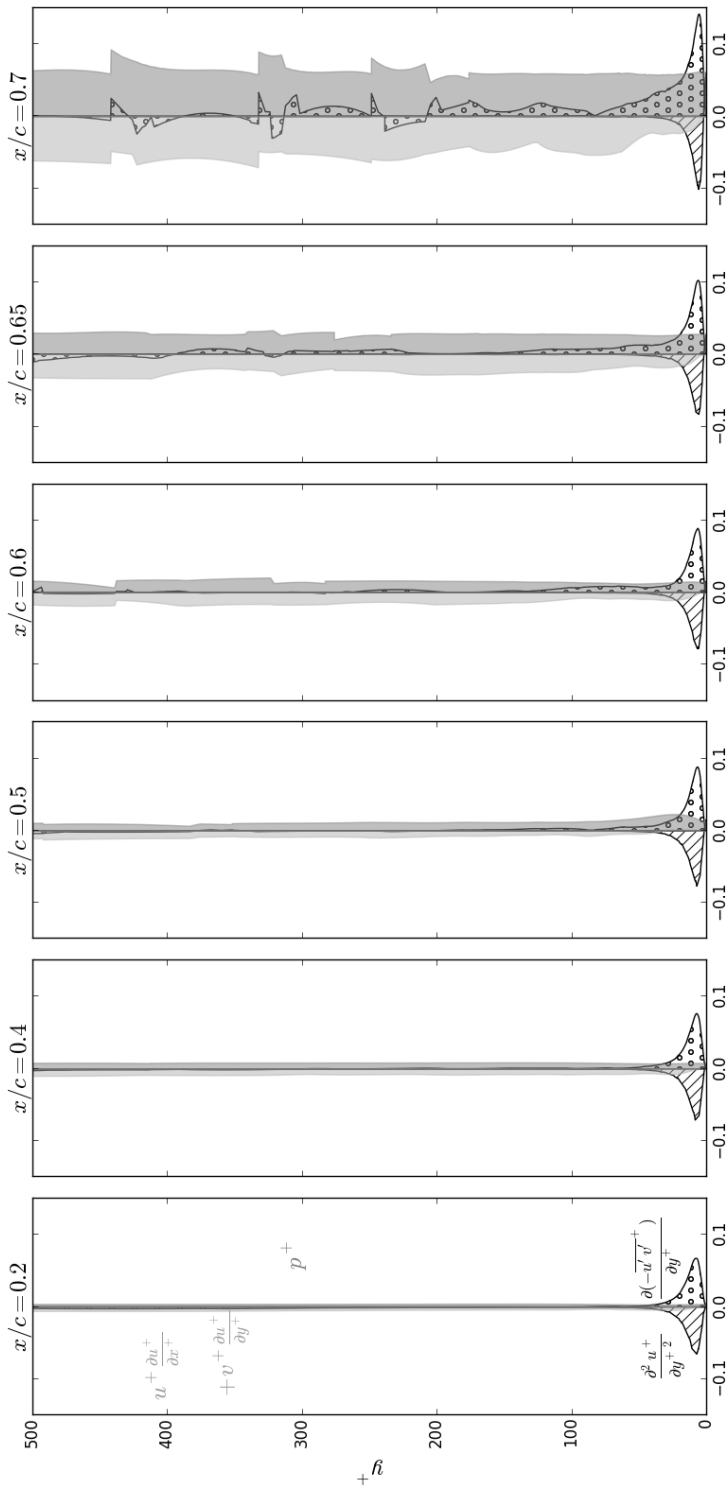


Figure 5.22: Balance along the chord and along the wall distance of the convective (light gray), pressure gradient (dark gray) and left-hand side terms (hatched and dotted) considered in the TLM equation Eq. (5.1).

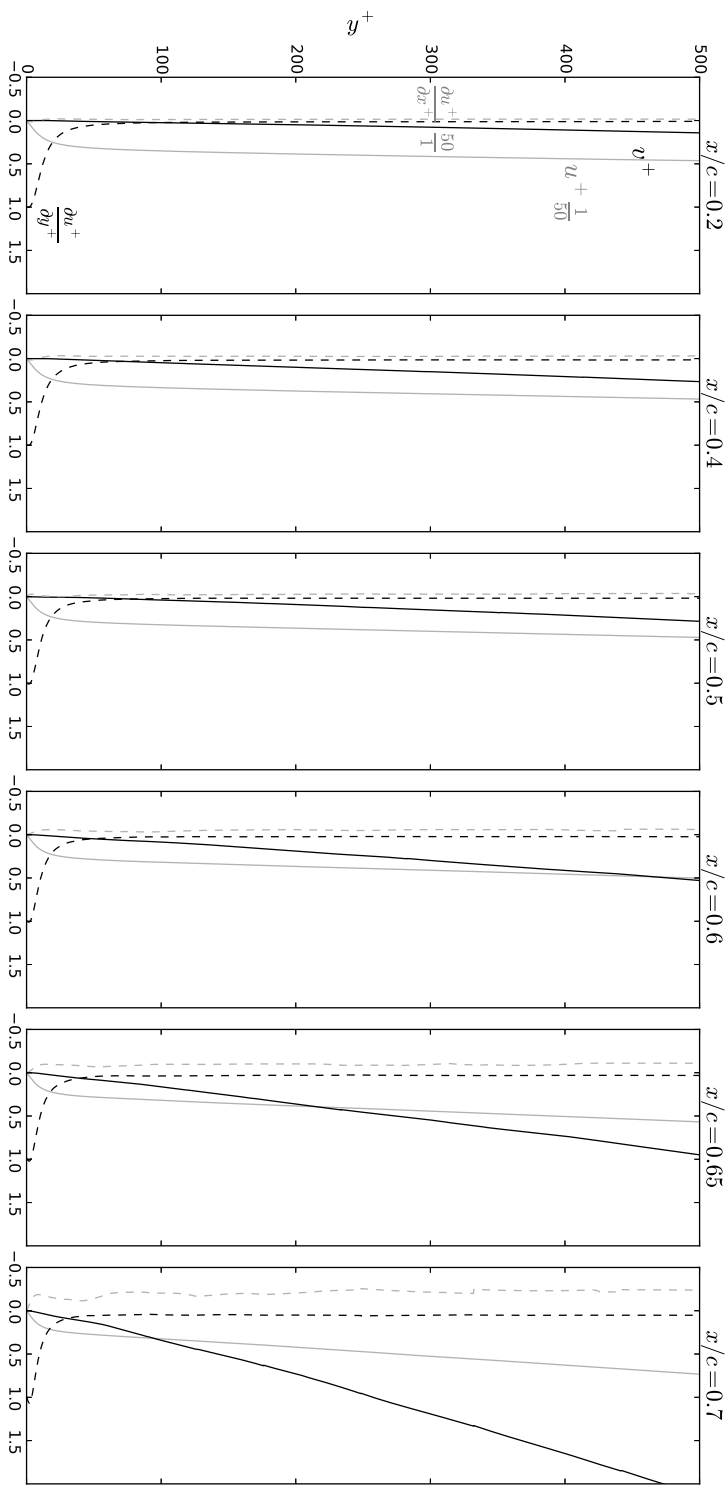


Figure 5.23: Balance along the chord and along the wall distance of the convective terms: u^+ (gray solid), v^+ (black solid), $\frac{\partial u^+}{\partial x^+}$ (gray dashed), and $\frac{\partial u^+}{\partial y^+}$ (black dashed). Note that to appear on the same scale, u^+ has been divided by 50, and $\frac{\partial u^+}{\partial x^+}$ multiplied by 50.

5.4 Comparison between wmLES and wrLES

In this section, the findings of the previous section are used to push further the analysis about the wmLES presented in Section 5.2. In that section, the wmLES velocity profiles had been studied at $x/c = 0.529, 0.815, 0.952$, in order to match the locations measured by Wadcock [101]. A good agreement had been observed for the most upstream location but the two other locations exhibited strong deviations. Using the wrLES data, the comparison can be performed all along the chord extent. Figure 5.24 compares the mean tangential velocity profiles for $0.05 \leq x/c \leq 0.95$ with steps of $x/c = 0.1$. In the buffer element, *i.e.* below the dashed line, the wmLES is not plotted. Above the buffer element, the match is quite good for the chordwise positions $x/c \leq 0.65$. The wmLES thus appears to capture the boundary layer flow on more than half of the chord and the differences are mostly attributable to the inability to capture the separation point. The performance of the wmLES thus appears more promising under this new light.

Figure 5.25 compares the velocity profiles in wall units before the separation, *i.e.* $0.05 \leq x/c \leq 0.80$ with steps of $x/c = 0.05$. The wrLES results are the same as the ones presented previously but circles are added to represent the position where the wmLES takes its input. As almost all circles fall within the log region, the position chosen for the wall model input is acceptable. However, most circles are close to the upper limit of the region. Therefore, a smaller y_{wm} would have been better. Some oscillations are also observed in the second element. All these observations hint at a further refinement of the mesh.

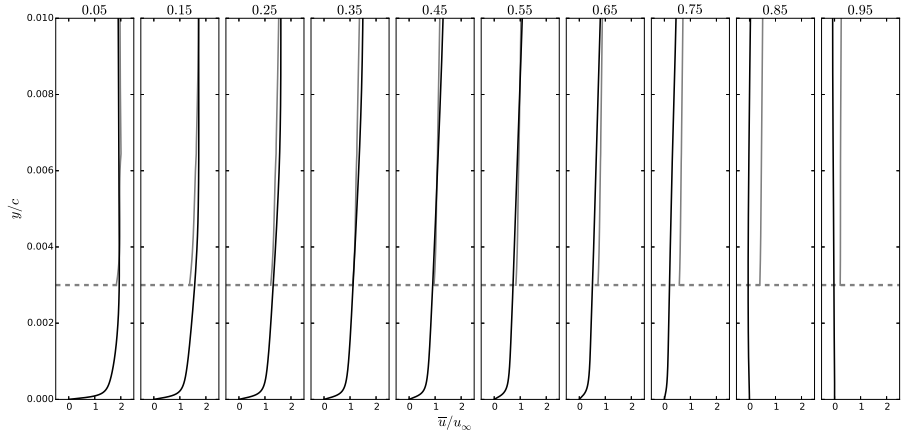


Figure 5.24: Comparison of the tangential velocity profiles along the chord for $0.05 \leq x/c \leq 0.95$ by steps of $x/c = 0.1$. wrLES is represented by black line. wmLES is represented by gray lines. The horizontal dashed line indicates the wall model input location. The wrLES results are not provided below that line as this corresponds to the unresolved solution in the buffer element.

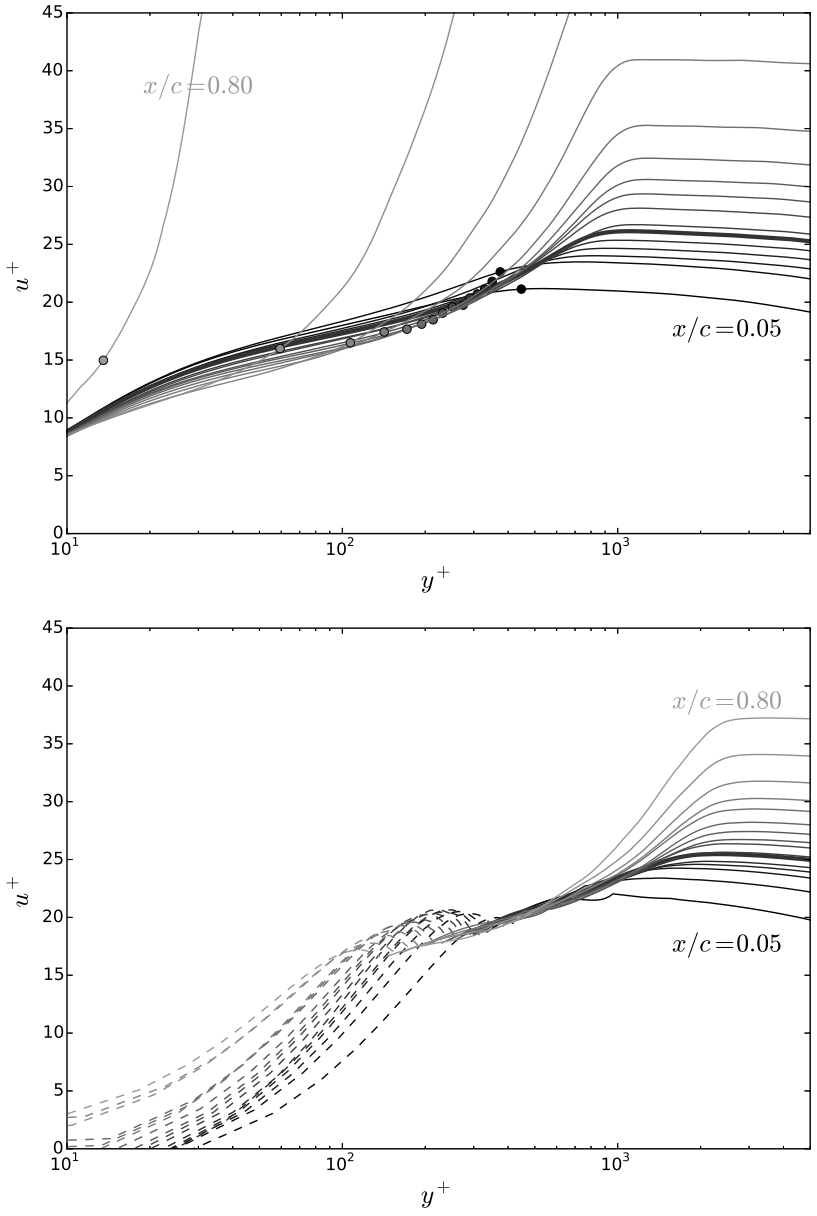


Figure 5.25: Tangential velocity profile evolutions along the chord in wall units and logarithmic scale. The profiles are given at positions x/c ranging from 0.05 to 0.80 with steps of 0.05 and are colored from black to light gray. A thicker line is used to indicate the profile for $x/c = 0.30$. The wrLES results are at the top, and the circles indicate the positions of the wall model input. The wmLES results are at the bottom, with dashed lines to indicate the unresolved solution in the buffer element.

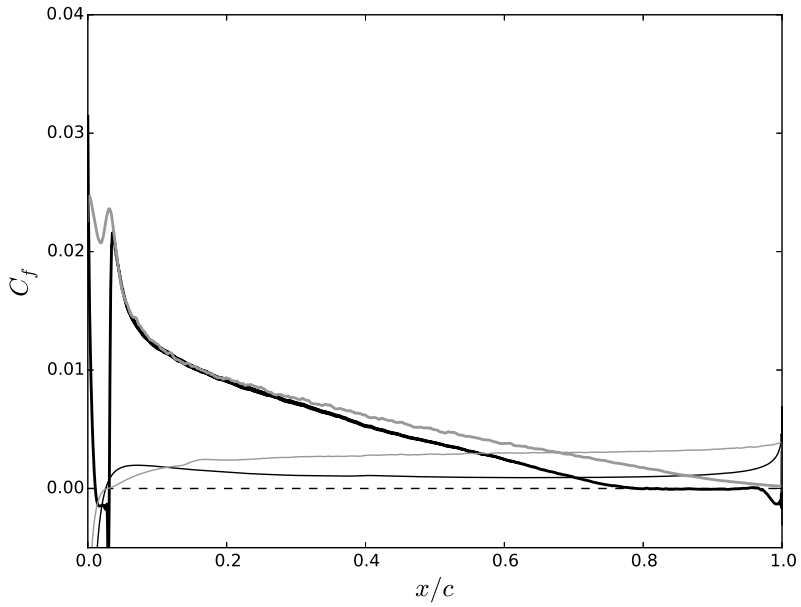


Figure 5.26: Chordwise friction coefficient evolution. Comparison of the wrLES (black lines) to the wmLES (gray lines). The suction side data are highlighted by using a thicker line.

For the wmLES, the velocity in the buffer element (dashed line) shows, as expected, a large oscillation ($p = 2$). The rest of the profiles have the right trend. The velocity profiles are quantitatively similar to the wrLES ones up to $x/c = 0.3$. After that point, the evolutions are only qualitatively similar. This can come from the fact that the input position is not placed correctly, but also from the usage of very different span extents (the wrLES uses $s/c = 1\%$ while the wmLES uses $s/c = 10\%$).

Figure 5.26 compares the chordwise friction coefficient evolutions predicted by the wrLES and the wmLES. As observed previously in the comparison to RANS and XFOIL, the curves are better matching on the suction side than on the pressure side. Considering that the wrLES shows a laminar boundary layer on the entire pressure side and that the wall model assumes a turbulent boundary layer, it is normal that the model over-estimates the shear. For the same reason, on the suction side, the laminar separation bubble is not captured by the wmLES and the friction does not match for $x/c \leq 0.03$. However, after that laminar region, the match is very good for $x/c \leq 0.2$. The wrLES wall shear reduces then faster than the wmLES and separates. As pointed before, the refinement or the use of a wall-normal mesh that grows as δ will certainly improve the wmLES results. Also, as the wmLES uses a span $s/c = 10\%$ that is ten times larger than the one used by the wrLES $s/c = 1\%$, the eventual span influence in the separation needs to be evaluated.

5.5 Preliminary results: wrLES with a span ten times larger

The wrLES studied in Section 5.3 is performed on a narrow span corresponding to 1% of the chord. This span is adequate for the development of the turbulent boundary layer, and is therefore sufficient to perform wall model comparison, at least up to the mid-chord. In order to be more physically correct, further studies are currently performed on a span that is ten times larger. These computations are made possible by a one year allocation at the Tier 0 Jülich Supercomputing Centre (PRACE R2Wall project). At the time of writing this thesis, the computations still need four months to run and the statistics are not converged. Therefore, only two interesting points regarding the setup are presented here.

5.5.1 Numerical setup

In addition to the span increase, from 1% to 10% of the chord, the rest of the domain and of the mesh are improved to obtain the best possible computation. The domain is enlarged in order to avoid any influence of the far-field boundary conditions. Figure 5.27 compares the domains of the two cases. All previous computations were made on a squared domain of 40 chords. For the new computation, a rounded domain is used with a radius that corresponds to 100 chords.

Based on the findings of Section 5.3, the resolution of the mesh is sufficient at the wall. However, to improve the capture of the boundary layer, the growth rate of the grid is reduced. As for the case with a span of 1%, the boundary layer is made of quadrangles that form a C-type mesh and the rest of the domain is unstructured. However, the triangles are here recombined in quad-

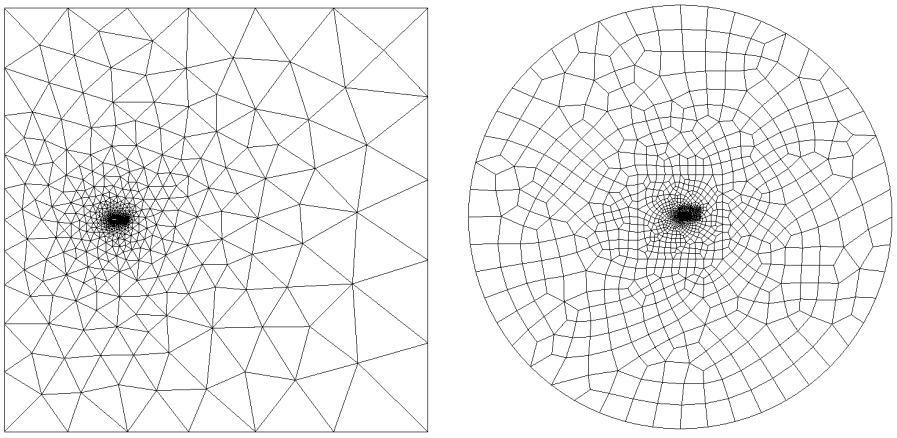


Figure 5.27: 2D views of the global domains considered for the wrLES computations. The domain used for the wrLES with a span of 1% is given on the left. The domain used for the wrLES with a span of 10% is given on the right.

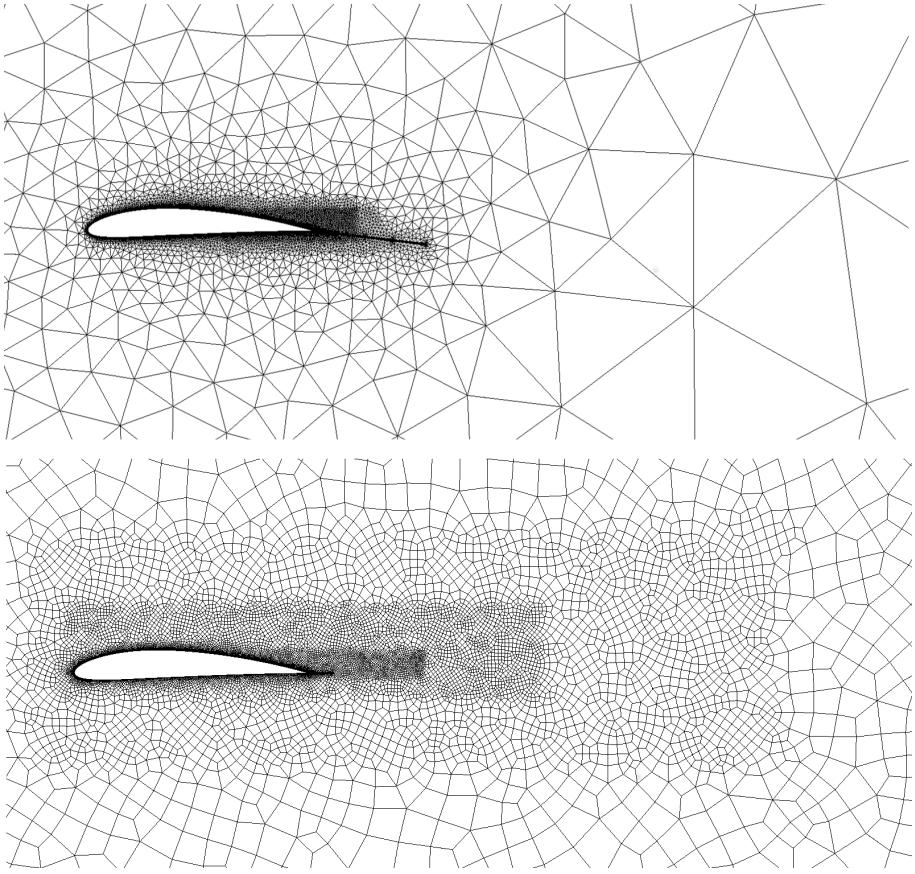


Figure 5.28: 2D views of the meshes considered for the wrLES computations: mesh for the span of 1% (top) and for the span of 10% (bottom).

rangles to improve the computational performance. Figure 5.28 shows a closer view of the two meshes. The total 3D mesh has about $6M$ elements that corresponds to approximately $400M\ dof$. Due to the mesh refinement, this is a bit more than ten times the mesh with a span of 1% that had approximately $35M$ dof.

5.5.2 Initialization: use of the wrLES with a small span

The computation needs to be initialized with the best solution in order to limit the time required to evacuate the transient. Therefore, the results from the computation on the small span are used and the solution is copied about ten times in the span direction. The risk with this approach is that the periodicity of the small span remains present for several flow-through times and some noise thus needs to be added to force the mixing.

At the time of starting the computation, the addition of noise in Argo was global and had not been tested on airfoil flows. There was thus a risk to keep some disturbance for a time corresponding to the distance between the inlet and the airfoil, *i.e.* $100\ ftt$. A solution was to code and test a local noise, applied only on the airfoil. Another solution, chosen here, was to obtain a mixing by the use of the periodic conditions.

The mixing arises from the fact that the span of 10% is not exactly ten times bigger than the 1% case, which was actually 1.0312% wide. As the initial field is obtained by copying ten times the solution of the small span, without any overlap, the initial solution is composed of nine perfect copies of the small span and a truncated one. Figure 5.29 shows the instantaneous pressure fields on the suction side of the airfoil at two moments after the restart from the smaller span. Nine vertical white lines indicate also the positions of the repeated initial field.

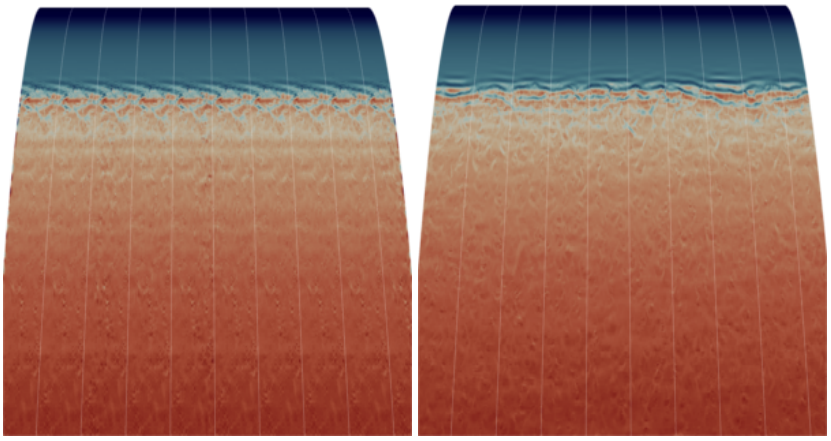


Figure 5.29: Instantaneous pressure field on the first $\simeq 60\%$ of the suction side at two different time steps after the restart from the smaller span. On the left, only one time step has been made after the restart, on the right $0.3\ ftt$ have been made. The vertical white lines represent the positions where the initial solution has been copied.

After one time step, the nine repetitions of the structures and the truncation are clearly visible. After $0.3\ ftt$, the periodicity is no longer strong.

To analyze this further, Figure 5.30 compares the spanwise variations of the pressure at different chordwise locations for both time steps. For all chordwise positions, the flow after the restart presents more fluctuations than after $0.3\ ftt$. These fluctuations are representative of the small structures coming from the quasi 2D flow. For the locations $x/c \geq 0.55$, a periodicity is observed just after the restart and it disappears after $0.3\ ftt$.

Figure 5.31 presents the spanwise correlations of the pressure at four locations. The correlations just after the restart clearly show peaks at distances that correspond to the length of the small span. At $x/c = 0.15$, for instance, we can clearly identify two signatures of the periodicity that was injected in the initial condition. A first one is the series of peaks at $N \times 0.010312$, as expected from the periodic duplicates of the small domain. A second set of weaker peaks is due to the shorter periodicity enforced between the last duplicate and the first one; those are then expected at a distance equal to the original period minus the overlap $d_o = 10 \times 0.010312 - 0.1$, and with the following peaks appearing at the original periodicity: $0.010312 - d_o + N \times 0.010312$.

These peaks have vanished at $t = 0.3\ ftt$ at all the chordwise locations, thus confirming that our initialization has efficiently broken the small domain periodicity in the vicinity of the airfoil.

To conclude, Figure 5.32 shows a global view on the airfoil after about $1.5\ ftt$. The impact of the short span computation is still visible in the far wake. Near the airfoil, the flow has already adapted to the larger span.

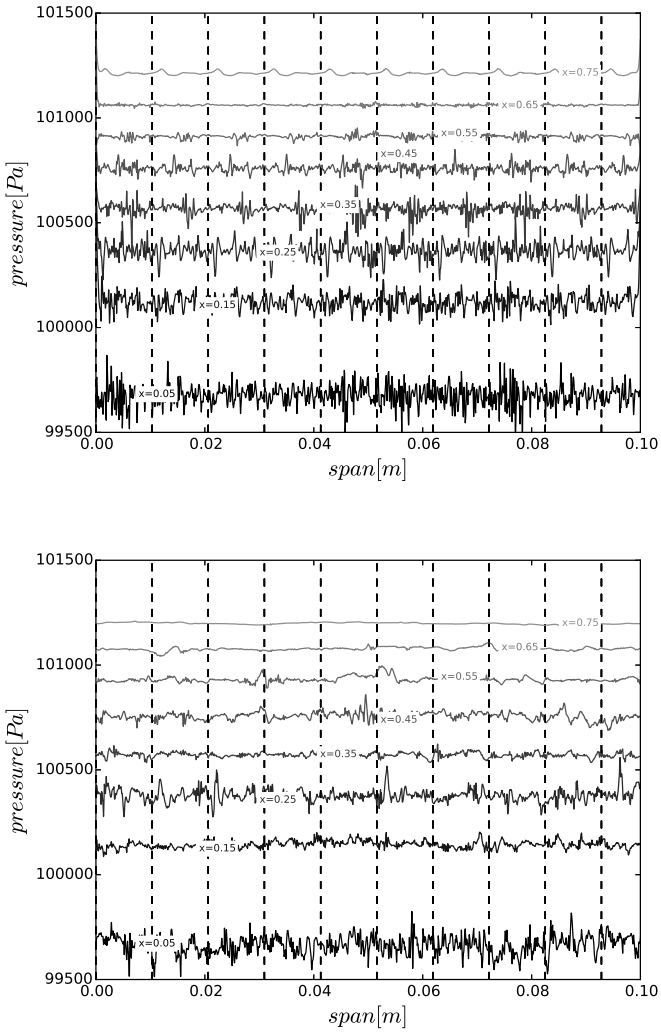
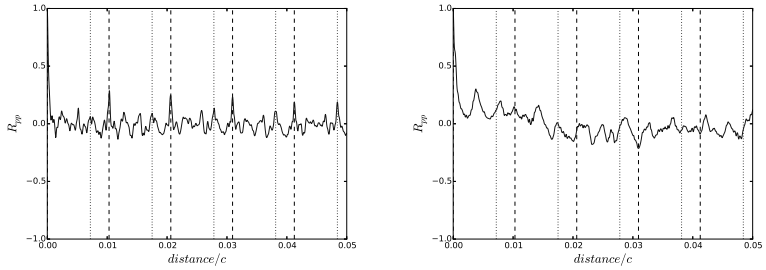
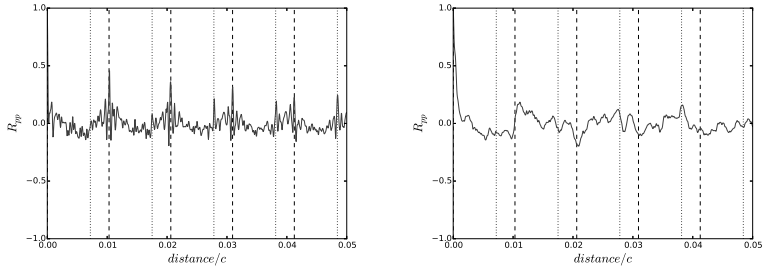


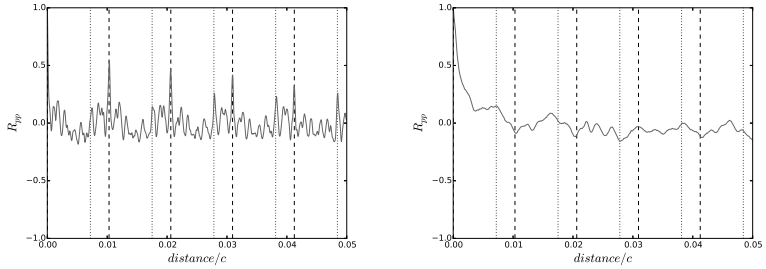
Figure 5.30: Instantaneous spanwise pressure at different chordwise positions on the suction side at two different time steps after the restart from the smaller span. At the top, only one time step has been made after the restart, at the bottom $0.3\ ftt$ have been made. The vertical dashed lines represent the positions of the boundaries where the result of the smaller span has been copied.



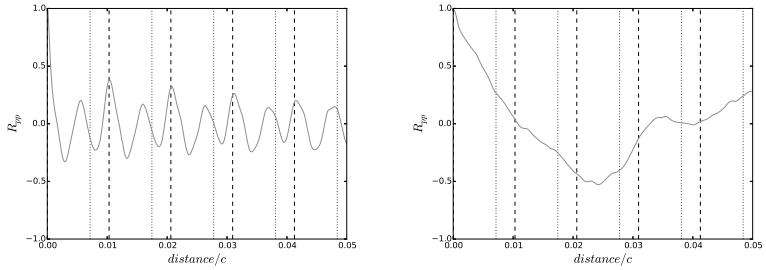
$x/c = 0.15$



$x/c = 0.35$



$x/c = 0.55$



$x/c = 0.75$

Figure 5.31: Pressure correlation on the suction side at two different time steps after the restart from the smaller span. On the left, only one time step has been made after the restart, on the right $0.3\ ftt$ have been made. The vertical dashed lines represent the distance between the periodic boundaries from the smaller span, *i.e.* $N \times 0.010312$. The vertical dotted lines represent the effect of the truncation, *i.e.* $0.010312 - d_o + N \times 0.010312$.

Figure 5.32: Initial results of the computation with a $span/c = 10\%$. Instantaneous Q criterion colored by Mach number with a close-up on the leading edge and on the wake. The zoom the leading edge shows the laminar separation and the transition. The zoom on the wake shows the 10 repetitions of the structures in the span direction that come from the initialization with $span/c = 1\%$.

5.6 Achievements

In this chapter, the NACA4412 airfoil is studied at $Re = 1.64 \times 10^6$ and $\alpha = 12.0°$ with both wall-modeled and wall-resolved LES.

For the wmLES, the guidelines developed in Chapter 4 are applied. As this corresponds to the first evaluation of the wmLES approach on a complex test case, the cost of the computation is kept as low as possible. Therefore, Reichardt wall model is chosen, although it is not supposed to capture properly the small laminar region nor the strong APG. Furthermore, as Chapter 4 advises to use polynomials of even degree in the wall-adjacent/buffer elements, $p = 2$ is used rather than $p = 4$, considered as too expensive here. Finally, as the boundary layer grows largely on the airfoil suction side and as the grid height is constant, the rule of $y_{wm} \simeq 0.2\delta$ is only fixed at the mid-chord position. Therefore, this position is likely too far from the wall in the first half of the chord. When compared to the grid uses for the wrLES of the E387, the grid obtained that way provides the relation $Re^{0.35}$. Therefore, the grid cost evolution with the Reynolds number is close to the prediction from Chapman [21].

As for the E387 airfoil presented in Chapter 3, the wmLES results are compared to experimental data as well as to XFOIL and RANS results. The test case is considered complex as there is a laminar region, a transition, a boundary layer subjected to an APG and a separation. Therefore, considering the simplicity of the wmLES approach, the completion of the calculation is already an achievement. Furthermore, the comparison of the wmLES to the other approaches in terms of lift, drag, pressure and friction coefficients shows that the wmLES captures correctly the global flow behavior. A close look at the pressure coefficient evolution shows that the wmLES is even closer to the experiment than the other approaches in the first half of the suction side. Close to the trailing edge, the three numerical approaches fail in predicting the pressure plateau observed experimentally. By examining the RANS and wmLES velocity profiles in that region, it appears that the numerical approaches do not capture the same flow separation as in the experiment. However, the RANS approach is closer to the experiment than the wmLES.

In that situation, the common approach is to perform a new wmLES with a more advanced wall model to get closer to the experimental results. However, considering the difficulty to reproduce perfectly the experimental setup and the cost of testing *a posteriori* different wall models, another approach is chosen in this work. A wall-resolved LES is performed in order to increase the understanding about the APG effect on the boundary layer and to aid the development of wall-modeled LES.

The wrLES results, obtained using a relatively small span, are successfully compared to seven previous studies, both numerical and experimental, in terms of pressure coefficient distribution, velocity and Reynolds stresses pro-

files. It appears that the obtained results are well within the range of the previous studies and also satisfactorily match the experimental results.

An *a priori* analysis of the wall models on the basis of the wrLES results shows that basic wall model as Reichardt's law-of-the-wall or Werner and Wengle's model can be sufficient, as long as the input location is located well below the end of the log layer. More elaborate analytical models that take the pressure gradient into account, such as that proposed by Shih, do not seem appropriate for high Reynolds number flows. Finally, an analysis of the TLM terms as they appear in the wrLES confirms previous observations that the convective terms are almost balanced by the pressure gradient term within the log region. This indicates that, also for the TLM, an equilibrium approach outperforms a more elaborate approach that is solely enriched by the pressure gradient.

Based on these findings, the wmLES results are re-analyzed. This permits to detect that the wall model input is placed slightly too far from the wall and that the wmLES mesh needs to be refined. Furthermore, as the pressure side is fully laminar and as an LSB is observed on the suction side, the wmLES overestimates largely the wall shear. Therefore, contrarily to what was first thought, the effort in terms of wall modeling should primarily be put in switching correctly from laminar to turbulent flow.

To better capture the separated flow as well as the near wake, and to evaluate an eventual span effect, a new wrLES is currently performed on a span that is ten times larger. It costs usually a lot to bring a large computation of this type to the converged state. Here, in order to reduce the cost, the short span computation is used as initial solution for the large span. The preliminary results indicate that the application of the periodic conditions on a initial flow that is not periodic is sufficient to mix the flow in the spanwise direction. Besides verifying the impact of the span on the results, this new computation will also push the study further by comparing the other models and by performing spanwise correlations.

CHAPTER 6

CONCLUSIONS AND PERSPECTIVES

The aim of this PhD thesis is twofold. The first objective consists in evaluating the discontinuous Galerkin method in problems that are relevant for the wind turbine industry. The second objective resides in the reduction of the large computational cost that affects LES at high Reynolds numbers by the implementation and the validation of a wall-modeled LES approach. In order to achieve these two objectives, this work presents several wall-resolved and wall-modeled LES of wind turbine airfoils at low and high Reynolds numbers. The DG solver developed at Cenaero, which is called Argo, is used to perform the wall-resolved LES and it is enhanced to perform the wall-modeled LES.

This work is only the second to perform wrLES of low Reynolds number airfoils with the present implementation of the DG method. Two low Reynolds number airfoils had already been studied in a previous PhD [15]. A DNS of the E387 airfoil did not agree with the experiment and was then assessed through a comparison with a DNS performed by the finite volume variant of the code. A LES of the SD7003 airfoil was also performed and compared to a DNS performed with the same code. These efforts can then be seen as a verification of the LES approach for airfoil flows but validation still had to be performed.

6.1 Conclusions

The first ambition of this work was to validate the wall-resolved LES approach on low Reynolds number airfoils. To that end, two low Reynolds number airfoils were analyzed in Chapter 3, namely the S826 and the E387. For these two airfoils, various wrLES were performed and compared to both experimental and numerical references.

The study of the S826 airfoil enabled the verification of the wrLES approach against a well-established code in the wind sector (EllipSys3D). Furthermore, it highlighted the extreme sensitivity of the measurements to the tunnel environment, and especially to the inflow turbulence. The latter indeed largely impacts the transition, and thus the extent of the long laminar separation bubbles observed at low Reynolds number. As the resolution of the inflow turbulence requires considerable computational resources, it is rarely considered in wrLES of airfoil flows, thereby leading to large differences between the numerical and the experimental results. The correct characterization of the inflow turbulence seen by a wind turbine airfoil remains a challenge, both numerically and experimentally. This comes not only from the turbulence intensity, but also from the large turbulence length scales observed in the atmospheric boundary layer. The extended analysis conducted in this work, both numerically and experimentally, permitted to provide a strong confidence in the validity of the computations and to detect large stall cells in the experiment. Based on this cross-validation, a guidance was suggested to reconcile CFD and experiment and to help the validation of low Reynolds number airfoils.

The study of the E387 airfoil provided a good match with the experiment and therefore the desired validation of the approach. Furthermore, the comparison with the methods that are widely used in the wind industry (RANS and XFOIL), confirmed that the wrLES better captures the flow separation. Therefore, this work demonstrated the interest and the validity of the wrLES approach to solve wind turbine airfoil flows.

A wmLES approach was also implemented to tackle high Reynolds number flows. The main challenge usually stated regarding the wmLES approach concerns the wall model capability to predict the wall shear. This work also identified another, and arguably more fundamental, challenge for wmLES: the approach needs to master the interplay between the model and the behavior of the numerical method in the first coarse mesh elements above the wall. Therefore, the two challenges were studied equally and addressed separately in Chapter 4 and Chapter 5.

In Chapter 4, the simplicity of the turbulent channel flow configuration allowed to evaluate the influence of various parameters, *e.g.* the polynomial degree. This enabled to develop a robust methodology and to obtain an accuracy close to the one observed on previous wall-resolved LES of the same test case.

Table 6.1 gathers the grid requirements used previously to perform DNS and wrLES of the channel and compares them to the ones allowed by the wmLES. The cost reduction obtained with wmLES is considerable and very promising.

This study constituted also the first rigorous sensitivity analysis for wmLES in a DG method. Therefore, the findings made in this work enabled the establishment of valuable guidelines for the use of wmLES in discontinuous finite-element-like methods. The most important guideline was that, even for high-order method, the input data needs to be taken in the second element and polynomials of even degrees need to be used in the first element.

In Chapter 5, these guidelines were used to characterize the flow over the widely used NACA4412 airfoil at a high Reynolds number. Despite the large coarseness of the grid, the wmLES successfully captured the global flow behavior. Therefore, this simulation constitutes a strong step and it provides a promising perspective for the wmLES approach, especially as various improvements are still possible.

One working point is the use of a more advanced wall model, which better captures the flow physics. With this aim in view, this work performed a wall-resolved LES of the same airfoil. In addition to enable the evaluation of different existing wall models, this wrLES provided a reproducible test case to support the development of wmLES.

The *a priori* analysis of different wall models permitted to compare the accuracy, robustness and applicability of different largely used models. Based on this study, this work could then recommend some wall models that are well-adapted to the simulation of airfoil flows. Furthermore, this work highlighted the fact that basic wall models can be more accurate than supposedly more advanced models.

By comparing the wmLES to the wrLES results on both pressure and suction sides, this work also highlighted the importance of improving the models to capture transitional flows. This constitutes a second, and potentially much more important, way to improve the wmLES approach.

	Re_τ	$\Delta x^+ \times \Delta y^+ \times \Delta z^+$	*Mdof*
DNS	180	$20 \times 0.2 \times 10$	5.0
wrLES	950	$30 \times 1.5 \times 15$	8.0
wmLES	5200	$400 \times 250 \times 400$	0.3
	50000	$3800 \times 2400 \times 3800$	0.3

Table 6.1: Grid required to perform DNS, wrLES and wmLES of the turbulent channel flow at different Reynolds numbers. The DNS and wrLES data come from a previous work performed with the DG approach [15]. The wmLES data are the ones obtained in this work.

Airfoil	$10^6\ Re$	AoA	$\frac{span}{c}$	$10^6\ dof$	n	LES type
S826	0.04	$0-12$	10.5%	3	-	wr
	0.10			15	2.0	wr
E387	0.60	$4-6-8$	10.5%	3	0.2	wr
NACA4412	1.64	12	10.5%	9	0.3	wm
			1.0%	35	1.3	wr
			10.0%	400	1.4	wr

Table 6.2: Summary of the main airfoils simulations performed in this work.

Finally, the grid costs that correspond to the different wrLES and wmLES performed in this work are compared in Table 6.2. We recall that the number of dof is used here to compare the computation costs instead of the total CPU time. This choice is deliberate as the computational time depends highly on the efficiency of the processors and as three types of processors have been used in this PhD work, *i.e.* ivybridge, westmere and bluegene cores. For example, the computation of one flow-through time over the NACA4412 required 0.3 MioCPUh for the span extent $s/c = 1\%$, run on westmere cores and 5.9 MioCPUh for the span extent $s/c = 10\%$ run on bluegene/Q cores. Based on the dof and the Reynolds number Re of the S826 airfoil, the cost evolution is estimated by the exponent n calculated using the following relation

$$\frac{dof/span}{(dof/span)_{S826}} = \left(\frac{Re}{Re_{S826}}\right)^n. \tag{6.1}$$

These values have to be used with caution as the three airfoils present very different geometries; the thicknesses, for example, are of 14% for the S826, 9% for the E387 and 12% for the NACA4412. Furthermore, the grid methodology has also changed from an O- to a C-type mesh. Still, the comparison does provide orders of magnitude between wm- and wrLES, especially for cases performed on the same airfoil. By comparing the cost increase between the two wrLES of the S826 airfoil, $n = 2$ is obtained. And by comparing it with wm- and wrLES of the NACA4412, the cost increases with $n = 0.3$ for the wmLES and $n = 1.4$ for the wrLES. The interest of the wmLES approach to drastically reduce the computational cost is again highlighted.

Almost all computations presented in this work have been performed on a Tier 1 machine that has about ten thousand cores. For the large wrLES of the NACA4412, forty thousand cores were needed and an access to a Tier 0 machine was requested. The experience gained in this work on the different wrLES and especially the case of the narrow span certainly helped in being granted this allocation.

6.2 Perspectives

This work validates the wrLES approach for the simulation of airfoil flows and demonstrates its added value with respect to the approaches currently used in the wind industry, *i.e.* the panel and the RANS methods. This work also enables the simulation of high Reynolds number airfoils at an affordable cost with the implementation of a wmLES approach.

As the large cost reduction goes inevitably with a loss of accuracy, it is hard to strike the right balance. In this work, the wmLES results are compared to the panel and the RANS methods. Table 6.3 compares the approximate CPU costs required to simulate a high Reynolds number airfoil. These costs are only estimates as they will depend on the solver and the processors that are used. For LES, they will also depend on the span extent that is considered (*e.g.* 5%, 10%) and of the performed flow-through times. This cost varies widely between the studies: one can find ratios between 5 and 20. This comes from the use of different methods to bring the flow to the converged state and also from the different tolerances considered for assessing the convergence of the statistics.

Panel method	RANS	wmLES	wrLES
seconds	minutes	days	weeks
1 core	10 cores	1000 cores	100.000 cores

Table 6.3: CPU times required to simulate an airfoil at $Re \simeq 2Mio$. These times are based on the NACA4412 computations performed in this work. The values are largely approximated and should therefore only be taken as orders of magnitude.

As the panel and the RANS methods are computationally inexpensive and as the wmLES results presented here do not provide any gain in predictive accuracy, this work cannot demonstrate the added-value of performing a full wmLES. However, the present work identifies a few tasks to further develop the wmLES approach and establish its advantages. Moreover, the method is already usable in a hybrid approach, by combining wmLES on the less critical parts of the geometry and wrLES on specific parts of interest, such as vortex generators.

In the short term, the research on improving wmLES will be continued using the wrLES of the NACA4412 airfoil with a span $s/c = 10\%$ as a calibration benchmark, see Figure 6.1. Computations are still ongoing, and will soon have passed the transient phase. The statistical data will permit to confirm the findings of this work, to evaluate a potential span effect and to extend the study to the separated flow region. This new work will provide a significant extension to this thesis, as more advanced analyses are planned. Firstly, as described in Appendix B, even for a given wall model, the use of different turbulent viscosity equations strongly impacts the result. Therefore, different

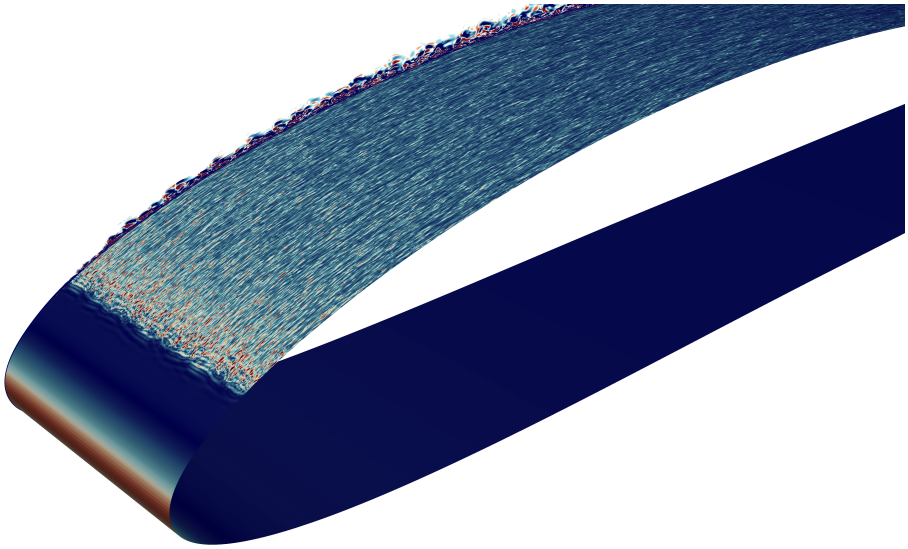


Figure 6.1: NACA4412 at $Re = 1.6 \times 10^6$ and $\alpha = 12°$: wrLES with a span $s/c = 10\%$. View of the instantaneous shear on the airfoil surface and of the instantaneous spanwise vorticity.

turbulent viscosity models will be compared. Secondly, new spanwise correlations will allow to quantify the sizes of the 3D structures. Figure 6.2 shows an example of this type of correlations for the 1% span case. On that figure, it appears that the correlations go to zero at $x/c = 0.30$ and $x/c = 0.53$ but not at $x/c = 0.95$. This confirms that the span of 1% is too small to correctly capture the flow after $x/c \simeq 0.6$. Thirdly, in addition to the analysis of the averaged data, the instantaneous correlations between shear and velocity will be studied. This will allow the definition of models that can be applied locally and instantaneously, thus providing more flexibility and efficiency.

In the long term, wall models also need to be developed to capture the laminar region and the transition. The first step should consist in having two models, one laminar, one turbulent, and to adequately switch from one to another. This improved model should then be applied on the NACA4412 airfoil to confirm that the observed disagreement with wrLES disappears. The wall roughness should also be taken into account, to enlarge the range of applications of the present wmLES and to enable the simulations of wind farm flows over complex terrains.

Parallel to this fundamental work, the industrialization of the approach is continuously pursued in close industrial and academic collaborations. The wmLES approach has been tested on the complex turbomachinery geometry presented in Figure 6.3. On that geometry, stability problems have been observed on the inlet guide vanes, as described in Appendix C. Although it is difficult

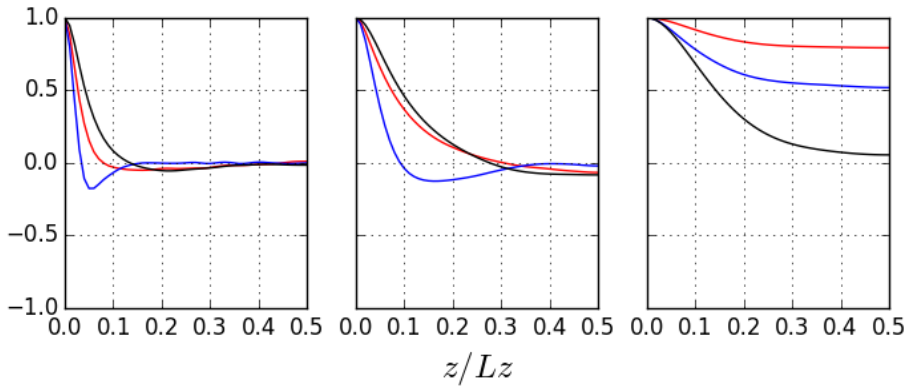


Figure 6.2: Spanwise correlations of the streamwise (red), normal (blue) and spanwise (black) fluctuating velocities at about 0.05δ from the wall on the NACA4412 with the span of 1%. Three positions along the chord are considered with $x/c = 0.30$ on the left, $x/c = 0.53$ in the center and $x/c = 0.95$ on the right. These results are given as example for the additional studies foreseen for the span of 10%.

to pinpoint the reason for this instability, the suspicion is that the use of the turbulent wall model on the laminar region induces a non-physical separation due to the overestimation of the friction.

Figure 6.4 shows the velocity around the inlet guide vane just before the stability problem. On the close view, the separation is clearly observed, as well

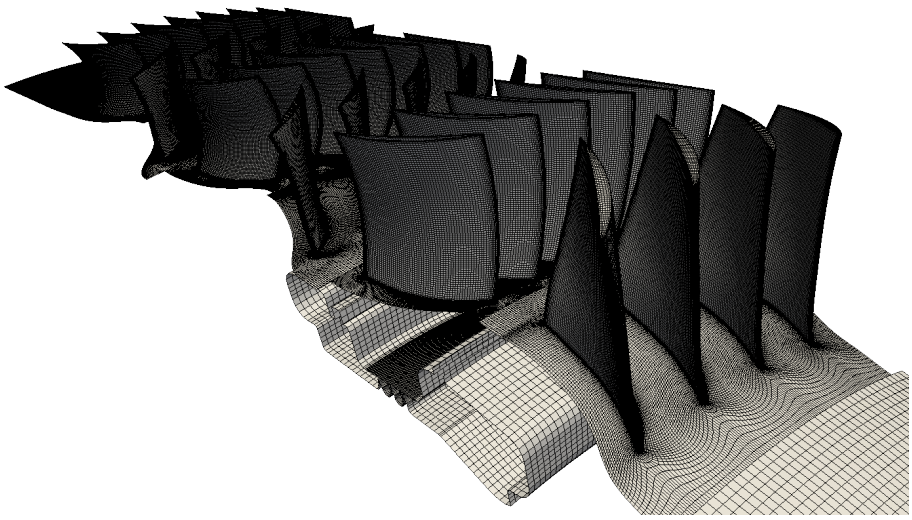


Figure 6.3: View of the surface mesh used for the CREATE test case.

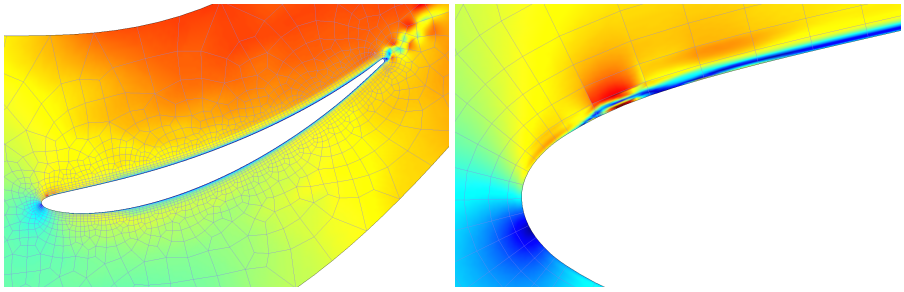


Figure 6.4: Comparison of the instantaneous velocity field [0-160 m/s] obtained just before the stability problem for the baseline case. A closer view on the leading edge is given on the right.

as some very large velocities at the wall. The addition of a laminar model and a transition switch will certainly alleviate this issue, and therefore help to increase the robustness of the approach. To apply the wmLES to the turbomachinery sector, a few modifications are also required. The boundary conditions need to master non-stationary walls and thermal wall models are necessary. These modifications have been verified on simple cases but they still need a thorough validation.

Finally, it is worth mentioning that, at the beginning of this work, a colleague made the following not so encouraging comment: "Don't be too enthusiastic about the simulations of airfoils, the first is fun, the next are boring", essentially sending the message that one does not learn much from successive airfoil simulations. At the end of this work, I strongly disagree with that statement: in a humbling process, every simulation of this work brought its share of lessons.

The only way to demonstrate the interest of LES as a "virtual wind tunnel" is to perform multiple validation cases, with different types of flow conditions and different types of grid. Furthermore, for the development of wmLES, sensitivity investigations such as the one performed for the channel flow are required to capture the interplay between the numerical approach and the coarse near-wall grid. As all LES, DNS and experimental tests are sensitive to their respective setup, none of them should be considered as the "truth". The different approaches should be used jointly, in order to complement each other and to push further the global understanding of airfoil aerodynamics.

BIBLIOGRAPHY

[1] Aerospace engineering website, picture of the development of the boundary layer over a flat plate. [Online; accessed December 10, 2017] *http://aerospaceengineeringblog.com/boundary-layers/*.

[2] ANSYS Fluent Theory Guide: 4.14.9 LES Near-Wall Treatment, 2015.

[3] D. Althaus. Profilpolaren für den Modellflug: Windkanalmessungen an Profilen im Kritischen Reynoldszahlbereich. Neckar-Verlag Villingen-Schwenningen, Germany, 1980.

[4] D. Arnold, F. Brezzi, B. Cockburn, and L. Marini. Unified Analysis of Discontinuous Galerkin Methods for Elliptic Problems. *SIAM Journal of Numerical Analysis*, 39:1749–1779, 2002.

[5] C. Bak, H. A. Madsen, P. Fuglsang, and F. Rasmussen. Double stall. Technical Report No. R-1043 (EN), RISOE, Risoe National Library, Roskilde, Denmark, 1998.

[6] E. Balaras, C. Benocci, and U. Piomelli. Two-layer approximate boundary conditions for large-eddy simulations. *AIAA journal*, 34(6):1111–1119, 1996.

[7] J. Barlow, W. Rae, and A. Pope. Low-speed wind tunnel testing. *John Wiley & Sons, New York*, 1999.

[8] M. J. Berger and M. J. Aftosmis. An ode-based wall model for turbulent flow simulations. *AIAA Journal*, pages 1–15, 2017.

[9] A. Bernard, J. Foucaut, P. Dupont, and M. Stanislas. Decelerating Boundary Layer: A New Scaling and Mixing Length Model. *AIAA Journal*, 41(2):248–255, 2003.

[10] S. Bocquet, P. Sagaut, and J. Jouhaud. A compressible wall model for large-eddy simulation with application to prediction of aerothermal quantities. *Physics of Fluids*, 24(6), 2012.

[11] S. T. Bose and P. Moin. A dynamic slip boundary condition for wall-modeled large-eddy simulation. *Physics of Fluids*, 26(1):015104, 2014.

[12] R. Brionnaud, D. M. Holmann, and M. C. Modena. Aerodynamic analysis of the 2nd AIAA High Lift Prediction Workshop by a Lattice-Boltzmann Method solver. 2014.

[13] A. P. Broeren and M. B. Bragg. Spanwise variation in the unsteady stalling flowfields of two-dimensional airfoil models. *AIAA Journal*, 39(9):1641–1651, 2001.

[14] W. Cabot and P. Moin. Approximate wall boundary conditions in the Large-Eddy Simulation of high Reynolds number flow. *Flow, Turbulence and Combustion*, 63:269–291, 2000.

[15] C. Carton de Wiart. *Towards a discontinuous Galerkin solver for scale-resolving simulations of moderate Reynolds number flows, and application to industrial cases*. PhD thesis, Ecole polytechnique de Louvain/iMMC, May 2014.

[16] C. Carton de Wiart and K. Hillewaert. DNS and ILES of transitional flows around a SD7003 airfoil using a high order discontinuous Galerkin method (paper ICCFD7-2012-3604). In *Seventh International Conference on Computational Fluid Dynamics*, Hawai, USA, 2012.

[17] C. Carton de Wiart, K. Hillewaert, L. Bricteux, and G. Winckelmans. LES using a Discontinuous Galerkin Method: isotropic turbulence, channel flow and periodic flow. In *Proceedings of the ERCOFTAC Workshop "Direct and Large-Eddy Simulation 9"*, Dresden, Germany, April 3-5 2013. ERCOFTAC.

[18] C. Carton de Wiart, K. Hillewaert, L. Bricteux, and G. Winckelmans. Implicit LES of free and wall bounded turbulent flows based on the discontinuous Galerkin/symmetric interior penalty method. *International Journal of Numerical Methods in Fluids*, 78(6):335–354, 11 March 2014. doi 10.1002/fld.4021.

[19] C. Carton de Wiart, K. Hillewaert, M. Duponcheel, and G. Winckelmans. Assessment of a discontinuous Galerkin method for the simulation of vortical flows at high Reynolds number. *Int. J. Numer. Meth. Fluids*, 74:469–493, 2013. doi: 10.1002/fld.3859.

[20] C. Carton de Wiart and S. M. Murman. Assessment of wall-modeled les strategies within a discontinuous-galerkin spectral-element framework. In *55th AIAA Aerospace Sciences Meeting*, page 1223, 2017.

[21] D. Chapman. Computational aerodynamics development and outlook. *AIAA Journal*, 17(12):1293–1313, 1979.

[22] Z. L. Chen, S. Hickel, A. Devesa, J. Berland, and N. A. Adams. Wall modeling for implicit large-eddy simulation and immersed-interface methods. *Theoretical and Computational Fluid Dynamics*, 28(1):1, 2013.

[23] H. Choi and P. Moin. Grid-point requirements for large eddy simulation: Chapman's estimates revisited. *Physics of Fluids*, 24(011702), 2012.

[24] A. Choudhry, M. Arjomandi, and R. Kelso. A study of long separation bubble on thick airfoils and its consequent effects. *International Journal of Heat and Fluid Flow*, 52:84–96, 2015.

[25] F. H. Clauser. Turbulent boundary layers in adverse pressure gradients. *Journal of the Aeronautical Sciences*, 21(2):91–108, 1954.

[26] D. Coles. The law of the wake in the turbulent boundary layer. *Journal of Fluid Mechanics*, 1956.

[27] D. Coles and A. J. Wadcock. Flying-hot-wire study of flow past an NACA 4412 airfoil at maximum lift. *AIAA Journal*, 17(4):321–329, 1979.

[28] M. Comsa. Picture of wind turbine blade sections. [Online; accessed Novembre 28, 2017] *cleanenergybrands.com*.

[29] J. W. Deardorff. A numerical study of three-dimensional turbulent channel flow at large Reynolds numbers. *Journal of Fluid Mechanics*, 41(02):453–480, 1970.

[30] C. Duprat, G. Balarac, O. Métais, P. M. Congedo, and O. Brugière. A wall-layer model for large-eddy simulations of turbulent flows with/out pressure gradient. *Physics of Fluids*, 23:015101, 2011.

[31] A. Frère, C. Carton de Wiart, K. Hillewaert, P. Chatelain, and G. Winckelmans. Application of wall-models to discontinuous Galerkin LES. *Physics of Fluids*, 29(8):085111, 2017.

[32] A. Frère, K. Hillewaert, P. Chatelain, and G. Winckelmans. High Reynolds number airfoil: from wall-resolved to wall-modeled LES. In *Proceedings of the DLES 11 conference*, 2017.

[33] A. Frère, K. Hillewaert, H. Sarlak, R. F. Mikkelsen, and P. Chatelain. Cross-Validation of Numerical and Experimental Studies of Transitional Airfoil Performance. In *Proceedings-33rd Wind Energy Symposium*, Kissimmee, 2015. AIAA.

[34] A. Frère, N. N. Sørensen, K. Hillewaert, P. Chatelain, and G. Winckelmans. Discontinuous Galerkin methodology for Large-Eddy Simulations of wind turbine airfoils. *Journal of Physics: Conference Series*, 753(2), 2016.

[35] G. Gassner and D. A. Kopriva. A comparison of the dispersion and dissipation errors of gauss and gauss-lobatto discontinuous galerkin spectral element methods. *SIAM J. Scientific Computing*, 33(5):2560–2579, 2011.

[36] M. Ge, D. Tian, and Y. Deng. Reynolds number effect on the optimization of a wind turbine blade for maximum aerodynamic efficiency. *Journal of Energy Engineering*, 142(1):04014056, 2016.

[37] N. Gregory and C. L. O'reilly. Low-speed aerodynamic characteristics of NACA 0012 aerofoil section, including the effects of upper-surface roughness simulating hoar frost. Technical Report 3726, Aeronautical Research Council reports and memoranda, London, 1973.

[38] M. M. Hand, D. A. Simms, L. J. Fingersh, D. W. Jager, J. R. Cotrell, S. Schreck, and S. M. Larwood. Unsteady aerodynamics experiment phase VI: wind tunnel test configurations and available data campaigns. Technical report, National Renewable Energy Lab., Golden, CO.(US), 2001.

[39] R. C. Hastings and B. R. Williams. Studies of the flow field near a NACA 4412 aerofoil at nearly maximum lift. *The Aeronautical Journal*, 91(901):29–44, 1987.

[40] K. Hillewaert. *Development of the Discontinuous Galerkin Method for high-resolution, large scale CFD and acoustics in industrial geometries*. PhD thesis, Ecole polytechnique de Louvain/iMMC, February 2013.

[41] K. Hillewaert, C. Carton de Wiart, G. Verheylewegen, and T. Arts. Assessment of a high-order discontinuous Galerkin method for the direct numerical simulation of transition at low Reynolds number in the T106C high-lift low pressure turbine cascade. In *Proceedings of the ASME Turbine Technical Conference and Exhibition*, number GT2014-26739. ASME Turbo Expo 2014, 2014.

[42] H. P. Horton. *Laminar separation bubbles in two and three dimensional incompressible flow.* PhD thesis, 1968.

[43] K. Jansen. Preliminary large-eddy simulations of flow around a NACA 4412 airfoil using unstructured grids. *Annual Research Briefs, Center for Turbulence Research, Stanford University/NASA Ames Research Center*, 1995.

[44] K. Jansen. Large-eddy simulation of flow around a NACA 4412 airfoil using unstructured grids. *Annual Research Briefs, Center for Turbulence Research, Stanford University/NASA Ames Research Center*, pages 225–232, 1996.

[45] H.-J. Kaltenbach and H. Choi. Large-eddy simulation of flow around an airfoil on a structured mesh. *Center for Turbulence Research, Annual Research Briefs*, 1995.

[46] S. Kawai and K. Asada. Wall-modeled large-eddy simulation of high Reynolds number flow around an airfoil near stall condition. *Computers & Fluids*, 85(0):105 – 113, 2013.

[47] S. Kawai and J. Larsson. Wall-modeling in large eddy simulation: Length scales, grid resolution, and accuracy. *Physics of Fluids*, 24(1):015105, 2012.

[48] J. Larsson, S. Kawai, J. Bodart, and I. Bermejo-Moreno. Large eddy simulation with modeled wall-stress: recent progress and future directions. *Mechanical Engineering Reviews*, 3(1):15–00418, 2016.

[49] J.-P. Laval. Direct Numerical Simulations of channel flow over a smooth geometry - Dataset: *dns channel flow with APG*. TurbBase Cineca IRODS repository, data creator: Laval, J.-P.

[50] J. Lee, M. Cho, and H. Choi. Large eddy simulations of turbulent channel and boundary layer flows at high Reynolds number with mean wall shear stress boundary condition. *Physics of Fluids*, 25(11):110808, 2013.

[51] M. Lee and R. D. Moser. Direct numerical simulation of turbulent channel flow up to $Re_\tau = 5200$. *Journal of Fluid Mechanics*, 774:395–415, 2015.

[52] T. Leonard. Modelling of air flow close to a non-moving turbine blade with LES. *http://www.cerfacs.fr/~cfdbib/repository/WN_CFD_09_164.pdf*, 2010.

[53] G. Lodato, P. Castonguay, and A. Jameson. Structural wall-modelled LES using a high-order spectral difference scheme for unstructured mesh. *Flow, turbulence and combustion*, 92(593-606), 2014.

[54] H. Ludwig and W. Tillman. Untersuchungen veber dis Wandschub in turbulenten Reibungsschichten, translated as Investigations of the wall shearing stress in turbulent boundary layers, NACA TM no. 1285, 1949.

[55] N. Maheu, V. Moureau, P. Domingo, F. Duchaine, and G. Balarac. Large-eddy simulations of flow and heat transfer around a low-mach number turbine blade. In *CTR Summer Program*. Center for Turbulence Research, NASA Ames/Stanford Univ., 2012.

[56] M. Marquillies, J.-P. Laval, and R. Dolganov. Direct Numerical Simulation of a separated channel flow with a smooth profile. *Journal of Turbulence*, 9(1), 2008.

[57] I. Marusic, J. P. Monty, M. Hultmark, and A. J. Smits. On the logarithmic region in wall turbulence. *Journal of Fluid Mechanics*, 716:R3, 2013.

[58] J. McArthur. *Aerodynamics of wings at low Reynolds number*. PhD thesis, University of Southern California, 2008.

[59] R. J. McGhee, B. S. Walker, and B. F. Millard. Experimental results for the Eppler 387 airfoil at low Reynolds numbers in the Langley low-turbulence pressure tunnel. Technical Report TM-4062, NASA, Langley Research Center, Hampton, Virginia, 1988.

[60] G. Medic, G. Daeninck, J. A. Templeton, and G. Kalitzin. A framework for near-wall RANS/LES coupling. *CTR Annual Research Briefs*, pages 169–182, 2005.

[61] J. Michelsen. Basis3D - a Platform for Development of Multiblock PDE Solvers. Technical Report AFM 92-05, Technical University of Denmark, December 1992.

[62] J. Michelsen. Block structured Multigrid solution of 2D and 3D elliptic PDE's. Technical Report AFM 94-06, Technical University of Denmark, May 1994.

[63] R. Nave. Picture of pressure profile around airfoil. [Online; accessed December 10, 2017] *hyperphysics.phy-astr.gsu.edu/hbase/Fluids/airfoil.html*.

[64] F. Nicoud, J. S. Baggett, P. Moin, and W. Cabot. Large eddy simulation wall-modeling based on suboptimal control theory and linear stochastic estimation. *Physics of Fluids*, 13(10):2968–2984, 2001.

[65] J. M. Österlund, A. V. Johansson, H. M. Nagib, and M. H. Hites. A note on the overlap region in turbulent boundary layers. *Physics of Fluids*, 12(1):1–4, 2000.

[66] G. I. Park. Wall modeling in large-eddy simulation. CTR Summer Program, tutorial seminar, 07/01/2016.

[67] G. I. Park and P. Moin. An improved dynamic non-equilibrium wall-model for large eddy simulation. *Physics of Fluids*, 26(1):015108, 2014.

[68] F. Pierella, P. Krogstad, and L. Sætran. Blind test 2 calculations for two in-line model wind turbines where the downstream turbine operates at various rotational speeds. *Renewable Energy*, 70:62–77, 2014.

[69] U. Piomelli. *Wall-Modeled Large-Eddy Simulations: Present Status and Prospects*. Springer Netherlands, 2010.

[70] U. Piomelli and E. Balaras. Wall-layer models for large-eddy simulations. *Annual review of fluid mechanics*, 34(1):349–374, 2002.

[71] S. Pope. *Turbulent Flows*. Cambridge University Press, 2000.

[72] L. Prandtl. Verhandlungen des dritten internationalen Mathematiker-Kongresses in Heidelberg, trans. as Early Developments of Modern Aerodynamics, Butterworth-Heinemann, Oxford,1904.

[73] J. Regan. Picture of a candle. [Online; accessed December 10, 2017] *flickr.com/photos/43558134@N06/albums/72157628971455339*.

[74] D. Rodríguez and V. Theofilis. On the birth of stall cells on airfoils. *Theoretical and Computational Fluid Dynamics*, 25(1-4):105–117, 2011.

[75] H. Sarlak. *Large Eddy Simulation of turbulent flows in wind energy*. PhD thesis, DTU Wind Energy, Technical University of Denmark, Lyngby, 2014.

[76] H. Sarlak, A. Frère, R. Mikkelsen, and J. N. Sørensen. Investigation of laminar separation and stall cell generation on low-Reynolds-number airfoils. *Experimental Thermal and Fluid Science (to be submitted)*.

[77] H. Sarlak, R. Mikkelsen, S. Sarmast, and J. N. Sørensen. Aerodynamic behaviour of NREL S826 at Re=100,000. *Journal of Physics: Conference Series (Online)*, 524(1), 2014.

[78] P. Schlatter and D. Henningson. *Seventh IUTAM Symposium on Laminar-Turbulent Transition: Proceedings of the Seventh IUTAM Symposium on Laminar-Turbulent Transition, Stockholm, Sweden, 2009*. IUTAM Book-series. Springer Netherlands, 2010.

[79] H. Schlichting. *Boundary Layer Theory*. Series in Mechanical Engineering. McGraw-Hill, 7th edition, 1979.

[80] S. Schmidt, M. Franke, and F. Thiele. Assessment of SGS Models in LES Applied to a NACA 4412 Airfoil. In *39st AIAA Aerospace Sciences Meeting and Exhibit*, 2001.

[81] P. Schrooyen. *Numerical Simulation of aerothermal flows through ablative thermal protection systems*. PhD thesis, Ecole polytechnique de Louvain/iMMC, November 2015.

[82] G. B. Schubauer and H. K. Skramstad. Laminar boundary layer oscillations and stability of laminar flow. *Journal of Aeronautical Sciences*, 14(2):69–78, 1947.

[83] U. Schumann. Subgrid scale model for finite difference simulations of turbulent flows in plane channels and annuli. *Journal of computational physics*, 18(4):376–404, 1975.

[84] M. S. Selig, R. W. Deters, and G. A. Williamson. Wind tunnel testing airfoils at low Reynolds numbers. In *49th AIAA Aerospace Sciences Meeting*, pages 4–7, 2011.

[85] M. S. Selig, J. F. Donovan, and D. B. Fraser. Airfoils at Low Speeds. H.A. Stokely publisher, Virginia, USA, 1989.

[86] T.-H. Shih. A generalized wall function. Technical report, National Aeronautics and Space Administration, Glenn Research Center, 1999.

[87] J. Smagorinsky. General circulation experiments with the primitive equations: I. the basic experiment. *Monthly weather review*, 91(3):99–164, 1963.

[88] J. N. Sørensen. Aerodynamic aspects of wind energy conversion. *Annual Review of Fluid Mechanics*, 43:427–448, 2011.

[89] N. Sørensen. General Purpose Flow Solver Applied to Flow over Hills. Risø-R- 827-(EN), Risø National Laboratory,Denmark, 1995.

[90] P. Spalart, W. Jou, M. Strelets, S. Allmaras, et al. Comments on the feasibility of LES for wings, and on a hybrid RANS/LES approach. *Advances in DNS/LES*, 1:4–8, 1997.

[91] D. B. Spalding. A Single Formula for the Law of the Wall. *Journal of Applied Mechanics*, 28(3):455–458, 1961.

[92] J. Sumner, C. S. Watters, and C. Masson. CFD in Wind Energy: The Virtual, Multiscale Wind Tunnel. *Energies*, 3:989–1013, 2010.

[93] A. Tan and J. Auld. Study of Laminar Separation Bubbles at Low Reynolds Number Under Various Conditions. In *11th Australasian Fluids Mechanics Conference, Hobart, Australia*, 1992.

[94] J. L. Tangler. The nebulous art of using wind tunnel aerofoil data for predicting rotor performance. *Wind Energy*, 5(2-3):245–257, 2002.

[95] O. Thiry. *Investigation of wall shear stress models for large eddy simulation*. PhD thesis, Ecole polytechnique de Louvain/iMMC, November 2016.

[96] P. Venugopal, L. Cheung, G. Jothiprasad, and S. Lele. Large eddy simulation of a wind turbine airfoil at high angle of attack. In *Center for Turbulence Research Proceedings of the Summer Program 2012*, 2112.

[97] R. Vinuesa, A. Bobke, R. Örlü, and P. Schlatter. On determining characteristic length scales in pressure-gradient turbulent boundary layers. *Physics of fluids*, 28(5):055101, 2016.

[98] R. Vinuesa, S. M. Hosseini, A. Hanifi, D. S. Henningson, and P. Schlatter. Direct numerical simulation of the flow around a wing section using high-order parallel spectral methods. In *International symposium on turbulence and shear flow phenomena (TSFP-9)*, 2015.

[99] R. Vinuesa, S. M. Hosseini, A. Hanifi, D. S. Henningson, and P. Schlatter. Pressure-gradient turbulent boundary layers developing around a wing section. *Flow, Turbulence and Combustion*, pages 1–29, 2017.

[100] D. Volker. Preliminary results of wind tunnel measurements on some airfoil sections at Reynolds numbers between 0.6×10^5 and 5.0×10^5. Memo. M-276, Delft Univ. of Technology, June 1977.

[101] A. J. Wadcock. Investigation of low-speed turbulent separated flow around airfoils. Nasa - 177450, NASA Ames Research Center, 1987.

[102] M. Wang and P. Moin. Dynamic wall modeling for large-eddy simulation of complex turbulent flows. *Physics of Fluids*, 14(7):2043–2051, 2002.

[103] Z. Wang, K. Fidkowski, R. Abgrall, F. Bassi, D. Caraeni, A. Cary, H. Deconinck, R. Hartmann, K. Hillewaert, H. Huynh, N. Kroll, G. May, P.-O. Persson, B. van Leer, and M. Visbal. High-order CFD methods: current status and perspective. *International Journal for Numerical Methods in Fluids*, 72(8):811–845, 2013.

[104] H. Werner and H. Wengle. Large-eddy simulation of turbulent flow over and around a cube in a plate channel. In *Turbulent Shear Flows 8*, pages 155–168. Springer, 1993.

[105] F. M. White. *Viscous fluid flow*. McGraw-Hill, 1974.

[106] P. Wu and J. Meyers. A constraint for the subgrid-scale stresses in the logarithmic region of high reynolds number turbulent boundary layers: A solution to the log-layer mismatch problem. *Physics of Fluids*, 25(1):015104, 2013.

[107] H. Zhu, S. Fu, L. Shi, and Z. J. Wang. A hybrid rans-implicit les approach for the high-order fr/cpr method. In *54th AIAA Aerospace Sciences Meeting*, page 1599, 2015.

APPENDIX A

TURBULENT CHANNEL FLOW: ADDITIONAL TEST CASES

A.1 Grid refinement and aspect ratio study for variable order cases

Section 4.2.4 showed that the polynomial degree of the buffer element should be $p_B = 4$ but that the rest of the domain could stay at $p = 3$. For the sake of clarity, the study on the mesh impact was made with $p = 4$ in the entire domain but it is interesting to verify the conclusion for the configuration with $p_B = 4$ in the buffer element and $p = 3$ in the rest of the domain. Table A.1 presents the three new cases. The case C15 is refined in the three directions while keeping the aspect ratio $\frac{\Delta x}{\Delta y} = \frac{\Delta z}{\Delta y} = AR = \pi/2$. The cases C16 and C17 are coarsened to obtain aspect ratios of $AR = 1$ and $AR = 2$, respectively.

Figure A.1 shows that the grid refinement and the change of aspect ratio performed here have no impact on the velocity profiles. These results are similar to those obtained with $p = 4$ in the entire domain. Therefore, the guidelines developed with a constant order seem acceptable for variable order cases.

	Grid size	Deg.	Effective wall resolution		Input
	$n_x \times n_y \times n_z$	p	$\Delta x\ \Delta y\ \Delta z$	$\Delta x^+\ \Delta y^+\ \Delta z^+$	y_{wm}
	$[-]$	$[-]$	$[\%\delta]$	$[-]$	$[\%\delta]$
C15	$40 \times 20 \times 20$	$B4/3$	$4 \times 3 \times 4$	$200 \times 150 \times 200$	$B10$
C16	$40 \times 13 \times 20$	$B4/3$	$4 \times 4 \times 4$	$200 \times 200 \times 200$	$B15$
C17	$26 \times 16 \times 13$	$B4/3$	$6 \times 3 \times 6$	$300 \times 150 \times 300$	$B13$

Table A.1: Additional turbulent channel test cases description ($Re_\tau = 5200$): number of elements in each direction, polynomial degree, effective resolution (in terms of δ and of wall units, rounded to 50) and distance from the wall where the input velocity data is taken. The letter B indicates that the 'buffer element" configuration is used and precedes the polynomial order used in this element.

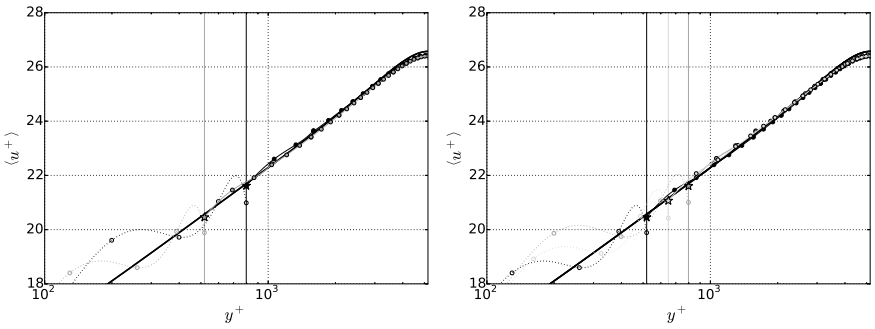


Figure A.1: Mean velocity profiles of the wmLES cases with different meshes. Refinements with constant cell aspect ratio are on the left with the baseline (C10-black line with markers) and the refined case (C15-dark gray line with markers). The different aspect ratios are on the right with the baseline aspect ratio $AR = \pi/2$ (C15-black line with markers) versus the smaller $AR = 1.0$ (C16-dark gray line with markers) and bigger $AR = 1.9$ (C17-light gray line with markers) aspect ratios. The DNS reference [51] is shown as a solid black line without markers. The vertical lines and the stars indicate respectively the position and the value of the wall model input data.

A.2 Mean velocity fluctuations

To limit the scope of the sensitivity analysis, only the velocity profiles were compared in the core of the work. However, it is important to verify whether the wmLES approach is able to capture higher order statistics. The velocity fluctuations are hence presented in Figure A.2 for the two best cases emerging from the sensitivity analysis of Section 4.2, namely C6 and C10. The two cases use $p_B = 4$ in the buffer element but C6 uses $p = 4$ in the rest of the domain, while C10 uses $p = 3$.

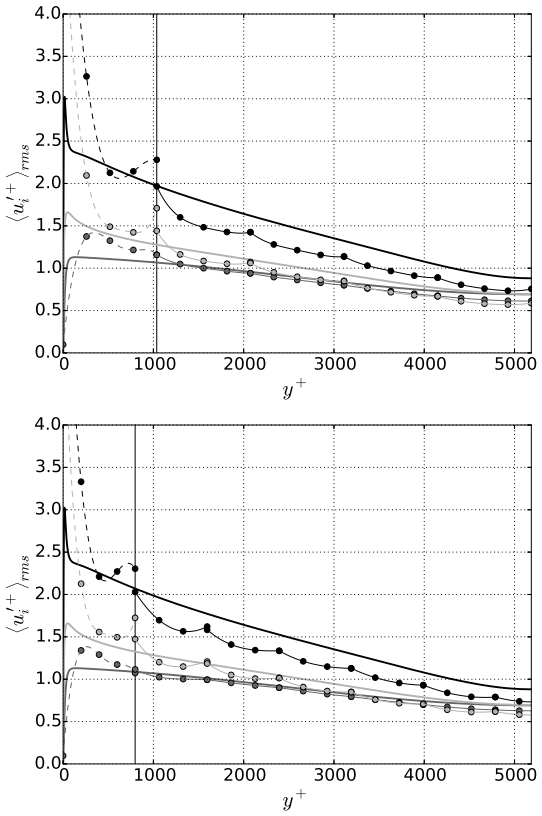


Figure A.2: Mean velocity fluctuations of the two wmLES best cases emerging from the sensitivity analysis. The results for the case C6 are on the top. The results for the case C10 are on the bottom. The fluctuations are presented using the root mean square of the streamwise (black), wall-normal (dark gray) and spanwise (light gray) fluctuations. The wmLES results are represented using solid and dashed lines with markers. In each element, $p+1$ equally spaced markers are used to represent the degree p of the Lagrange polynomial. To distinguish the under-resolved and resolved regions, the polynomials are drawn with respectively dashed and solid lines. The DNS references [51] are shown as solid lines without markers. The vertical lines indicate the sampling locations.

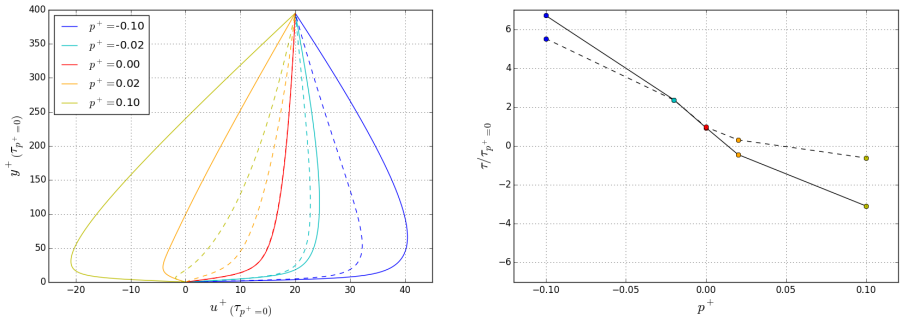
Figure A.2 shows that wmLES under-estimates the fluctuations but these results are however in line with wall-resolved LES results obtained with the same methodology at lower Reynolds numbers [18] and with wmLES approaches tested on the channel flow [67]. These results are hence considered satisfactory.

APPENDIX B

TWO-LAYER MODEL: IMPACT OF THE ν_t

As discussed in Section 2.1.5, different variants of the Two-Layer Model exist, with different equations for the turbulent viscosity, see Table 2.2. Three very different variants are compared here, namely those used by Bocquet *et al.* [10], Wang and Moin [102] and Duprat *et al.* [30].

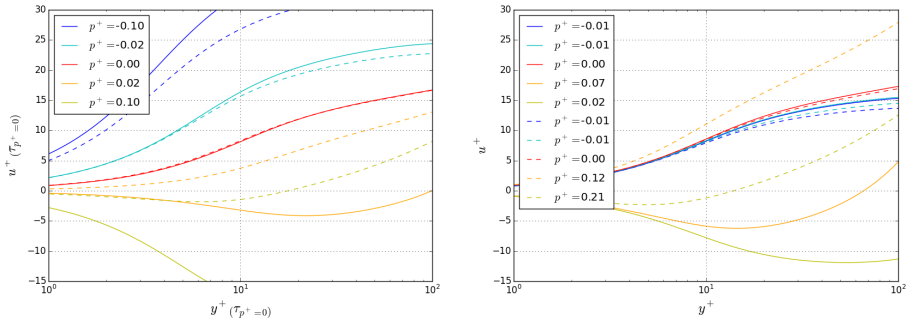
Before performing large computations, off-line unit tests of the models have been performed, comparing the velocity profile and wall shear stress found for a given velocity, a given distance and different pressure gradients. From this initial study, it appears that the method suggested in Bocquet *et al.* [10], based on Newton iterations, is difficult to converge for large pressure gradients. For this case a root-finding algorithm for which the convergence is guaranteed should be tested (*e.g.* Ridder's method as used by Lodato *et al.* [53]). Figure B.1(a) compares the velocity profiles up to the intercept for the ν_t expression used by Wang (solid line) and Duprat (dashed line), each time for the same pressure gradients, in a fully linear scale. As the computed shear stress not only varies in function of pressure gradient, but is also different for the two models, it was decided, for the sake of clarity, to use the shear stress obtained for a zero pressure gradient for the normalisation. It appears that the profiles are roughly similar for a zero or favorable pressure gradient but are very different otherwise. It seems that the pressure gradient has a much bigger impact on the flow in Wang's model. For example, at $p^+ = 0.02$, Wang's model predicts a backflow which is not seen with Duprat's model. Figure B.1(b) compares the obtained values for the different pressure gradients. This figure confirms that the models provide similar output for zero and favorable pressure gradients and that Wang's estimate is larger than Duprat's one for



(a) Calculated velocity profile (normalized using the wall shear stress at zero PG)

(b) Calculated wall shear stress (normalized by the stress at zero PG)

Figure B.1: Comparison of the results obtained using different ν_t equations: Wang and Moin [102] (solid line) and Duprat *et al.* [30] (dashed line).



(a) Calculated velocity profile (normalized using the wall shear stress at zero PG)

(b) Calculated velocity profile (normalized using the wall shear stress of each test case)

Figure B.2: Velocity profiles obtained using different ν_t equations: [102] (solid line) and [30] (dashed line).

adverse pressure gradients. For the largest adverse pressure gradients Wang's shear estimate is even three times bigger than Duprat's estimate.

For comparison to theory, the velocity profiles are also shown in log linear scale. On Figure B.2(a) the data are normalized as in B.1, using the wall shear stress obtained for a zero pressure gradient. To compare the effect of the pressure gradient to reference data, the data are presented on Figure B.2(b) with the more common normalization with the actual shear stress velocity obtained for each test case separately. This quick study permits to observe convergence difficulties with Bocquet's model and an amplification of the PG impact for Wang's model compared to Duprat's model.

APPENDIX C

ROBUSTNESS PROBLEMS ON IGV

The wall-modeled approach based on Reichardt's law has been validated on the turbulent plane channel flow and it has been tested on a free stream airfoil, the NACA4412. During the time of the PhD, other members of Cenaero's team used this wmLES approach on a part of an aircraft engine. On this very complex case, some instability was observed close to the leading edge of the inlet guide vane (IGV). Although it is difficult to pinpoint the reason for this instability, some ideas and few tests are given in the following paragraphs.

As Reichardt's law considers a turbulent boundary layer in equilibrium, it provides, in all cases, a positive shear stress. This shear is imposed in a direction that is opposed to the velocity direction taken at the input position. In case the flow is laminar, the shear stress predicted by the model is larger than what it should be. On the wmLES of the NACA4412 presented in Chapter 5, the laminar region is of about 1%. Some instabilities are observed close to the leading edge but they do not impede the global simulation. On the IGV, the instabilities propagate and lead to the apparition of large oscillations of velocity and a large separation.

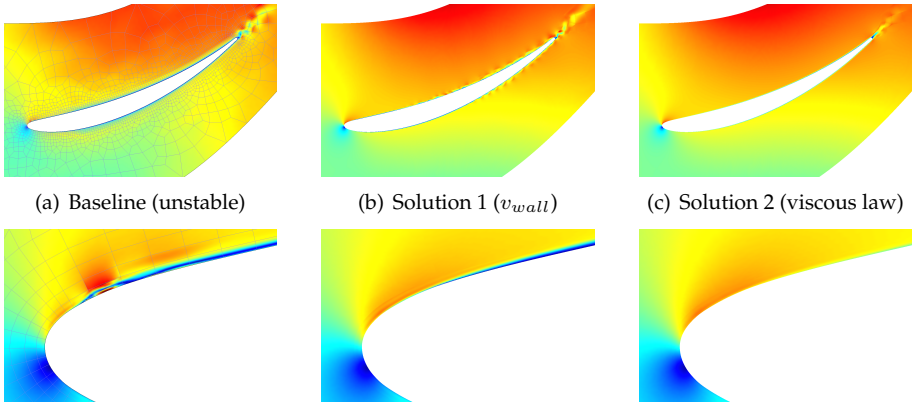
The main explanation is that this too high shear induces a slight separation of the flow. The separation induces an inflection point in the velocity profile. If the inflection point is between the wall and the input location, it will not be captured by the model. Therefore, the model will continue to apply a shear in opposition to the inlet velocity, *i.e.* in the direction of the velocity at the wall, and will reinforce the separation. This mechanism enhances the separation until it surpasses the interception location for the wall model, at which

point the stress is inverted. This seems to result in a very violent, but purely numerical, boundary layer transition.

For the IGV, this phenomenon is observed on the suction side behind the leading edge. Figure C.1 presents the instantaneous velocity field around an artificial periodic IGV blade section, cut from the profile of the IGV at midspan, as well as a closer view on the leading edge where the stability issue is observed. It appears on this figure that there is an extremely high velocity at the wall. This high velocity is pointing towards the leading edge, creating a reversed flow .

Two solutions have been tested.

- Solution 1 applies the same wall law (Reichardt) but imposes the wall shear stress in the direction of the wall velocity. In case of a flow reversal this solution will stabilize the flow.
- Solution 2 changes Reichardt turbulent wall law to a laminar/viscous sublayer law. This law will provide a lower shear stress and should hence avoid flow reversal.



(a) Baseline (unstable) (b) Solution 1 (v_{wall}) (c) Solution 2 (viscous law)

Figure C.1: Comparison of the instantaneous velocity field [0-160 m/s] obtained just before the stability problem for the baseline case (left), to the converged fields obtained with the solution 1 (center) and 2 (right). A closer view on the leading edge is given on the bottom.

The instantaneous fields of the two proposed solutions are compared to the baseline on Figure C.1 to C.3. On all these figures the results are presented just before the stability problem for the baseline case and after convergence for the two solution cases.

As presented on Figure C.1, the two proposed solutions permit to avoid the large flow reversal on the leading edge. However, they provide different velocity fields (see Figure C.1) with a turbulent behavior for Solution 1 and a laminar behavior for Solution 2. As planned, Solution 2 leads to much lower

wall shear stresses (see Figure C.3) and to much higher wall velocities (see Figure C.2). Solution 2 acts hence as an intermediate solution between a slip wall boundary condition and the use of a turbulent wall model. It will not permit to accurately predict the viscous loss but is a robust option and will be useful for flow initialization.



(a) Baseline (unstable) (b) Solution 1 (v_{wall}) (c) Solution 2 (viscous law)

Figure C.2: Instantaneous wall velocity [0-100 m/s]

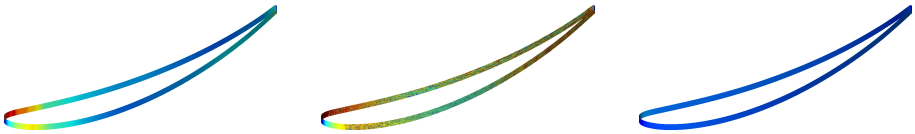


Figure C.3: Instantaneous wall shear stress [0-55 Pa]

Figure C.4: Comparison of the instantaneous velocity (up [0-100 m/s]) and shear stress (down [0-55 Pa]) on the airfoil surface with zoom on the leading edge for the three different approaches. Views are at different times. The case with Reichardt law and shear in the input velocity's direction is taken just before stability problem. The two other cases are converged.

Solution 1 permits to stabilize the computation and to obtain a very satisfying flow behavior. This approach has hence be chosen for the first computations on the machine. However, none of the two solutions provide acceptable results on the turbulent channel flow. They are hence good "tricks" to make the computation to work but are not validated approaches.